

X-shooter observations of strong H₂-bearing DLAs at high redshift[★]

S. A. Balashev¹†, V. V. Klimenko¹, P. Noterdaeme², J.-K. Krogager²,
D. A. Varshalovich¹, A. V. Ivanchik¹, P. Petitjean², R. Srianand³, C. Ledoux⁴

¹ *Ioffe Institute, Polytechnicheskaya ul. 26, Saint Petersburg, 194021, Russia*

² *Institut d'Astrophysique de Paris, UMR 7095, CNRS-SU, 98bis bd Arago, 75014 Paris, France*

³ *Inter-University Centre for Astronomy and Astrophysics, Post Bag 4, Ganeshkhind, 411 007, Pune, India*

⁴ *European Southern Observatory, Alonso de Córdova 3107, Casilla 19001, Vitacura, Santiago, Chile*

Accepted 2019 September 22. Received 2019 July 09

ABSTRACT

We present results from spectroscopic observations with X-shooter at the Very Large Telescope of seven H₂-bearing DLAs at high redshifts ($z_{\text{abs}} \sim 2.5 - 3$). These DLAs were originally selected from the presence of strong H₂ lines directly seen at the DLA redshift in low-resolution, low S/N SDSS spectra. We confirm the detection of molecular hydrogen in all of them. We measure the column densities of H I, H₂ in various rotational levels, and metal species, and associated dust extinction. The metallicities, obtained from undepleted species, are in the range $\log Z = -0.8$ to -0.2 . We discuss the chemical enrichment in these clouds and compare their properties with that of other molecular-rich systems selected by other means. In particular, we show that three different methods of pre-selection of H₂-bearing DLAs in the SDSS have their own biases but complement each other mostly in terms of chemical enrichment. We use the rotational excitation of H₂ molecules together with the fine-structure energy levels of neutral carbon to constrain the physical conditions in the gas with the help of numerical modelling as well as analytical expressions for the surface density at which atomic to molecular conversion happens. We find that the H₂-bearing medium revealed by the studied DLAs has typical values for the kinetic temperature, hydrogen density, and UV radiation field of, respectively, $T \sim 100$ K, $n_{\text{H}} \sim 100 \text{ cm}^{-3}$, and I_{UV} about twice the intensity of the Draine field. Detailed studies combining different selections should therefore bring important clues to understand the H I-H₂ transition at high redshift.

Key words: cosmology: observations – quasar: absorption lines – ISM: clouds, molecules

1 INTRODUCTION

Molecular hydrogen (H₂) is by far the most abundant molecule in the Universe and predominantly resides in the cold neutral gas of galaxies. This cold phase may be subject to Jeans instability and is hence thought to be tightly linked to the onset of star formation. While the association between star formation and molecular gas is well established on kpc-scales for normal galaxies in the local Universe (e.g. Bigiel et al. 2008; Schruba et al. 2011), observations in emission in the distant Universe have much coarser spatial resolution and are mostly limited to the bright-end (and much probably

high-metallicity end) of the galaxy population. In addition, the mass of molecular gas is estimated indirectly via tracers, like CO or dust emission, which are metallicity-dependent (e.g. Genzel et al. 2012). While the link between star formation and molecular gas has been observed in a variety of environments, there are some observational indications that star formation could proceed directly from the atomic gas when the metallicity is low (e.g. Michałowski et al. 2015). Indeed, in the diffuse ISM H₂ forms on the surface of dust grains, whose abundance scales with metallicity. Therefore, it is expected that at low metallicities, the H₂ formation timescale can be larger than the gravitational collapse time (see e.g. Krumholz 2012).

The star formation process can be studied not only in emission (where the relation between star formation and atomic gas is usually derived over the whole extent of the galaxy), but also through absorption-line studies. This is

[★] Based on observations carried out at the European Southern Observatory (ESO) Very Large Telescope Unit-2, Kueyen, under program ID 094.A-0362 (PI Balashev).

† E-mail: s.balashev@gmail.com

particularly useful for high-redshift galaxies, since the detection in absorption is independent of the luminosity of the associated object. Blind absorption-line studies indeed select systems owing to their cross-section only. The neutral gas in and around high-redshift galaxies in absorption studies is mostly detected via the H I-Ly α absorption line, producing the so-called damped Lyman- α systems (DLA, Wolfe et al. 2005), when the H I column densities reaches $\log N(\text{H I}) \gtrsim 20$, ensuring the gas is predominantly neutral. Statistical studies have shown that DLAs contain the bulk of the neutral atomic gas in the Universe (e.g. Noterdaeme et al. 2012b) and present a significant metallicity evolution with redshift (e.g. De Cia et al. 2018), i.e., the smoking gun of star formation. However, despite recent progress, it remains technically challenging to detect galaxy counterparts of DLAs in emission (see Krogager et al. 2017, and references therein), and therefore to understand the origin of DLAs and constrain the associated star-formation rates. However, absorption studies of cold and molecular gas already provide very useful information to understand the star-formation processes in high-redshift galaxies. Indeed molecular hydrogen is found in a fraction of high- z DLAs ($\sim 4\%$ for $\log N(\text{H}_2) \gtrsim 18$, Balashev & Noterdaeme 2018) meaning that cold gas is intercepted by the line-of-sight. Such H₂-bearing DLAs potentially provide information on the transition from atomic to molecular gas and subsequently on the onset of star formation.

Locally, observations towards nearby stars have revealed that the H₂ column density significantly increases when the H I column density reaches some threshold value. This threshold directly traces the H I-to-H₂ transition and is well-described by analytic and numerical modelling (see Sternberg et al. 2014, and references therein). The H I-to-H₂ transition is also found to occur at higher H I column density in the Magellanic clouds, owing to lower metallicities and stronger UV fields, in agreement with expectations from the models. In turn, a global understanding of the H I-to-H₂ transition at higher redshifts is still missing (see Noterdaeme et al. 2015), mostly because of small statistical samples, which actually probe a wide range of physical conditions. To date, there are ~ 40 confirmed intervening H₂-bearing DLAs detected at redshifts $z > 2$.

Before the advent of the Sloan Digital Sky Survey (SDSS; York et al. 2000), H₂ at high redshifts has been blindly searched, mostly in high-resolution DLA spectra from archival data. The detection rate is found to be quite low: Ledoux et al. 2003; Noterdaeme et al. 2008 found H₂ in about 10% of the DLAs surveyed using high-resolution spectra, while Jorgenson et al. 2014 found only one H₂ in 86 blindly-selected DLAs, using mid-resolution data. Petitjean et al. (2006) proposed that above a metallicity $Z > 0.2Z_{\odot}$, the probability to detect H₂ increases to about 50%. However, this is of little practical use since the metallicity is known accurately only once a high-resolution spectrum is obtained. With a huge increase in the number of quasar spectra available, the SDSS spectroscopic database has presented a unique opportunity to search for H₂ systems. Different techniques have been proposed to pre-select these from low-resolution, low-S/N spectra.

A first efficient pre-selection was based on the presence of neutral carbon lines (e.g., Srianand et al. 2008; Noterdaeme et al. 2010). Indeed, C I is a fragile species that survives more easily in the same conditions as H₂ requires (see

e.g. Liszt 1981; Ge et al. 2001). Since the strongest C I absorption lines are usually redshifted outside of the Lyman- α forest, it was possible to systematically search for C I in SDSS spectra without any prior on H I content (Ledoux et al. 2015). While the sample of C I-selected molecular systems is continuously increasing thanks to the SDSS (e.g. Ma et al. 2015; Noterdaeme et al. 2017), the majority of the systems have $z \lesssim 2$, so that H₂ (and sometimes H I) lines are inaccessible from the ground, due to the atmospheric cutoff at ~ 3000 Å. For those systems where H₂ is covered, Noterdaeme et al. (2018) find a 100% detection rate of H₂ molecules. However, it has been found that a selection based on C I only identifies metal-rich systems (with $Z \sim Z_{\odot}$, see Zou et al. 2018 and Ledoux et al., in prep.).

Another method to pre-select possible H₂-bearing systems is to consider extremely-strong DLAs (ESDLAs, with $\log N(\text{H I}) > 21.7$, Noterdaeme et al. 2014), since a large critical column density for atomic-to-molecular conversion is expected for clouds at the typical metallicity of DLAs. Such a conversion could furthermore explain the steeping slope of the observed $N(\text{H I})$ -distribution function at high $N(\text{H I})$ (Zwaan & Prochaska 2006; Altay et al. 2013). From a galactic-scale point-of-view, we also expect the corresponding lines-of-sight to probe gas at small galacto-centric distances, as confirmed by the detection of Lyman- α emission in composite ESDLA spectra (Noterdaeme et al. 2014) and in individual systems (Noterdaeme et al. 2012a; Ranjan et al. 2018). This picture is corroborated by the possible increase of thermal pressure with increasing H I column density (Balashev et al. 2017), indicating that such lines-of-sight probe more central regions of galaxies. An enhanced H₂ detection rate in ESDLAs has indeed been confirmed through follow-up of ESDLAs (Noterdaeme et al. 2015; Ranjan et al. 2019) as well as in stacked SDSS spectra (Balashev & Noterdaeme 2018).

Finally, Balashev et al. (2014) proposed to directly identify H₂ Lyman-Werner bands in SDSS spectra. However, this is a complex task because of the low spectral resolution, the typically low signal-to-noise ratio, and the presence of Ly α forest absorption lines. Due to these limitations, only a few percent of SDSS spectra are suitable for the detection of H₂, and only systems with high H₂ column densities ($N(\text{H}_2) \gtrsim 10^{19} \text{ cm}^{-2}$) can be detected. In our original search of SDSS DR9, we have found about 25 good H₂ candidates (with low false detection probability (FDP), see Balashev et al. 2014); A number that has since then been increased to about 100 using SDSS DR14.

In order to study the H₂ absorbers selected directly from SDSS in greater detail, we have initiated a follow-up program using the Very Large Telescope (VLT). The higher spectral resolution and signal-to-noise ratio allow us to confirm the presence of H₂ in the candidate systems and to measure the gas properties. One of the H₂-bearing DLAs at $z = 2.786$ towards J0843+0221 has already been published owing to its unique and extremely high H₂ column density of $\log N(\text{H}_2) \sim 21.2$ (Balashev et al. 2017). In the present paper, we describe the full analysis of the remaining 7 systems from this follow-up sample.

The paper is structured as follows. First, we describe the observations and the methodology that we have used to analyze the H₂-bearing DLAs in Sect. 2 and 3, respectively. In Sect. 4, we discuss the properties of the sample, which

Table 1. Journal of X-shooter observations.

Quasar	Date	Seeing (")	Airmass	Exp. times† (ks)
J 013644.02+044039.00	27.11.2014	1.15	1.16	3.6, 3.6, 3×1.2
J 013644.02+044039.00	28.11.2014	1.15	1.26	3.6, 3.6, 3×1.2
J 085859.67+174925.32	24.12.2014	0.73	1.36	3.6, 3.6, 3×1.2
J 085859.67+174925.32	15.02.2015	1.38	1.37	3.6, 3.6, 3×1.2
J 090609.46+054818.72	23.12.2014	0.79	1.26	3.6, 3.6, 3×1.2
J 090609.46+054818.72	25.12.2014	0.67	1.22	3.6, 3.6, 3×1.2
J 094649.47+121628.56	18.02.2015	0.83	1.27	3.5, 3.5, 3×0.9
J 094649.47+121628.56	18.02.2015	0.99	1.29	3.5, 3.5, 3×0.9
J 114638.95+074311.28	18.02.2015	0.79	1.19	3.6, 3.6, 3×1.2
J 114638.95+074311.28	24.02.2015	0.77	1.25	3.6, 3.6, 3×1.2
J 123602.11+001024.60	14.02.2015	0.87	1.13	3.6, 3.6, 3×1.2
J 123602.11+001024.60	18.02.2015	1.15	1.12	3.6, 3.6, 3×1.2
J 234730.76–005131.68	20.12.2014	0.52	1.39	3.6, 3.6, 3×1.2

† Exposure times given for the UVB, VIS, and NIR arms, in this order.

we compare to other H₂ samples arising from different selection methods. Lastly, in Sect. 5, we offer a summary of the findings presented in this paper.

2 OBSERVATIONS AND DATA REDUCTION

Since the main goal of our pilot observations was to confirm the reality of the H₂ absorption systems detected by Balashev et al. (2014), we first selected the targets with lowest false H₂-detection probability from our list of DLA systems (extended to DR10) and that were accessible from the Paranal observatory during the semester of observations. The sample was observed with the X-shooter spectrograph (Vernet et al. 2011) mounted at the Unit Telescope 2 of the VLT (VLT-UT2, Kueyen). The observations were performed in service mode under program ID 094.A-0362 (PI: Balashev) between the end of 2014 and beginning of 2015. The log of observations is given in Table 1. For all observations, we used a slit width of 1 arcsec in the UVB arm, and 0.9 arcsec in the VIS and NIR arms, leading to a resolving power of $R \sim 5400$, ~ 8900 , and ~ 5600 ¹ in the UVB, VIS, and NIR arms, respectively. For each target, we obtained two 1-hour exposures except for SDSS J234730.76–005131.68, which was observed only once before the end of the observations.

We first reduced the spectra using the ESO Reflex pipeline (Freudling et al. 2013). However, the unavailability of atmospheric dispersion correction at the time of observations led to a significant wavelength-dependent trace offset in the UVB, which was not properly taken into account by the pipeline. Therefore, we used our own code to extract the 1-dimensional (1D) spectra along the trace starting from the 2D pipeline product (which incorporates dark/bias correction, flat-field correction, 2D geometry and arc-line solutions). In addition, we improved the removal of cosmic-ray hits by flagging the corrupted pixels on the 2D exposures

¹ The actual value of the spectral resolution depends on the atmospheric seeing value, which in some cases was smaller than the slit width, see Table 1.

interactively. The 2D sky model was constructed using polynomial fitting along the spatial axis for each dispersion column and taking into account the rejection of outliers and correction of 2D geometrical issues at the edge of bright sky lines. We used the optimal-extraction method with a Moffat profile to extract the 1D spectrum (Horne 1986). Finally, we corrected the flux error in each pixel of each spectra by a wavelength-dependent factor so that it matches the observed dispersion relative to the quasar continuum. To do this, we identified unabsorbed regions in the continuum and estimated a smooth average of the dispersion of pixels using 5-10 Å-wide sliding windows. This extraction resulted in an overall $\sim 25\%$ improvement in the S/N ratio and a better handling of lower quality regions, which were otherwise hard to manage through the pipeline.

3 ANALYSIS

Before presenting the analysis of the different systems, we note that two out of seven DLAs studied in this paper have redshifts close to that of the quasar ($\Delta v \lesssim 3000$ km/s) and could hence be considered as proximate. This is quite surprising at the first glance since the parent sample used by Balashev et al. (2014), i.e., the DLA catalogue from Noterdaeme et al. (2012b), was based on a search optimised for intervening DLAs and hence likely biased against proximate DLAs. Recently, Noterdaeme et al. (2019) found that the incidence rate of proximate H₂-bearing DLAs (within ~ 2000 km s⁻¹ from the quasar) per redshift path unit can be a factor of 5 higher than that of intervening systems. However, the observed number of systems depends on the total redshift path probed by each sample and therefore intervening H₂ systems should still dominate in numbers over proximate ones, due to the much longer total pathlength. The relatively high number of proximate DLAs here is more likely to originate from selection method used for this follow-up sample. Indeed, the objects were selected upon their probability of false H₂-detection. This probability is strongly correlated with the number of the band used and therefore, the closer DLA to the quasar, the more H₂ bands are available in the spectrum before blue cutoff, and the smaller can be the false detection probability. In this work, as we concentrate on the chemical and physical properties of the systems and found no striking difference between those within a few thousands km s⁻¹ from the quasar and those located further in velocity space, therefore we consider them indistinctly.

3.1 Absorption lines

We analysed all DLA systems in our sample in the same manner. We used a custom routine² for Voigt-profile fitting to derive the redshifts, column densities and Doppler parameters of the velocity components for H I, H₂, C I, and various low-ionization metal absorption lines (e.g. Si II, Fe II,

² We used this routine in recent analyses of absorption-line systems (e.g., Balashev et al. 2016, 2017) and also, partly, in Noterdaeme et al. (2018); Krogager et al. (2018a), where we found that it usually is in good agreement with other codes used for Voigt-profile fitting, like vpfit (Carswell & Webb 2014) and VoigtFit (Krogager 2018).

Si II, Zn II). For each absorption line (except H I Ly α , described below) we derived the local continuum using a B-spline interpolation matched on the adjacent unabsorbed spectral regions. The spectral pixels used to constrain the fit were selected visually and iteratively. For each quasar we fit available exposures jointly without combining them. The number of velocity components was also defined visually and increased in case of remaining structure in the residuals. We used Monte-Carlo Markov Chain calculations with an affine invariant sampler (Goodman & Weare 2010) to obtain the posterior probability density function (PDF) of fitting parameters (assuming flat uninformative priors). While we directly obtained the PDF, in the following we use the standard way of reporting the best fitting parameters and uncertainties. The best fitting value corresponds to the maximum posterior probability and the estimated uncertainties correspond to the 68.3% confidence interval around this value (corresponding to formal 1σ uncertainty for Gaussian PDF).

We measured the H I column density from the Ly α line. However, since this line is strongly damped and frequently located close to the Ly α emission line, we simultaneously fitted the absorption profile and the unabsorbed continuum modelled usually by 4-8 order Chebyshev polynomials, depending on the wavelength range. The values all agree within 0.2 dex from those measured at lower S/N and resolution power from the SDSS data.

We confirm the presence of H₂ in all systems through the detection of Lyman- and Werner-band absorption lines. We only detect lines from several low rotational levels of the $v = 0$ vibrational ground state. Therefore, in the following, we use an abbreviated notation for those levels, as follows: H₂J_i, where index i is the rotational quantum number. While an increase of the Doppler parameter with increasing rotational level has been observed for several H₂ systems (Lacour et al. 2005; Noterdaeme et al. 2007; Balashev et al. 2009; Ivanchik et al. 2010), the spectral resolution of X-shooter is not high enough to study this effect. Therefore, we tied the Doppler parameters of different rotational levels when fitting H₂ lines. This implies that the reported column densities for high ($J > 2$) rotational levels should be considered with caution, in particular because the corresponding lines are generally in the intermediate regime. Notwithstanding, this has a little effect on the measurement of the total $N(\text{H}_2)$ which is dominated by the first rotational levels whose lines are damped and hence not sensitive to the exact Doppler parameter. Additionally, for each exposure we included two additional independent parameters when fitting H₂ lines, to linearly correct for the wavelength distortions caused by the unavailability of the ADC (see e.g. Noterdaeme et al. 2017). We then used the obtained values of the zero point and the slope of distortion to correct the spectrum before fitting the C I and low-ionization metal lines. Finally, since the seeing was narrower than the slit width for some exposures, we also varied spectral resolution for each exposure as independent fitting parameter. We found lower H₂ column densities than initially estimated from the SDSS in all cases, see Fig. 1. The reasons for this is that H₂ profiles are unresolved in SDSS, the blends with Ly α forest lines are hard to take into account and the signal to noise ratio are low. For these reasons, the SDSS-based H₂ column densities were considered as indicative only by Balashev et al. (2014). Notwithstanding, the column densities agree within 0.3 dex for 4 out of

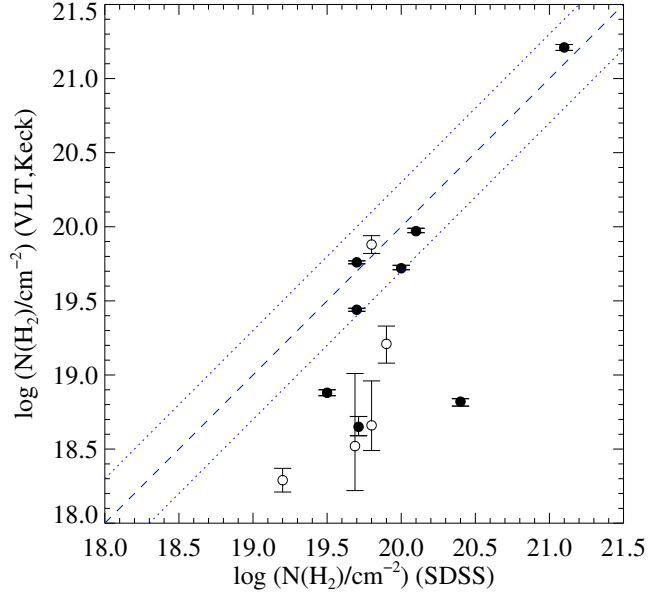


Figure 1. Comparison of H₂ column densities automatically determined from the low-resolution low S/N SDSS data with those obtained from medium/high-resolution observations. The sample studied in this paper is shown as filled symbols (all using X-shooter but J0843+0221 observed with UVES), while open symbols represent other known H₂ systems (all observed with UVES but towards J81240.69+320808.52, observed with HIRES on Keck, see Jorgenson et al. 2009).

7 DLAs (5/8 including J0843+0221). From the X-shooter data, we could see that these are indeed the cases where the H₂ profiles dominated by one main component, while for the other three DLAs with larger differences, there are at least two H₂ components with comparable column densities.

To fit the low-ionization metal lines, we tied the redshifts and Doppler parameters of various species since the broadening is dominated by turbulence which is independent of the atomic mass. We also varied spectral resolution for each exposure as independent fitting parameter. For all DLAs we detected associated C I absorption lines at the position of H₂ components. Therefore, we fitted the C I lines (and the associated fine-structure levels) independently from other metals.

The detailed fitting results, the corresponding figures and specific comments for each DLA in our sample are presented in Supplementary materials. The total column densities of H I, H₂, C I, the average molecular fraction, metallicity, and Fe depletion are summarised in Table 2. We also add the H₂-bearing DLAs towards J0843+0221 to our sample, since it was selected from SDSS using the same technique. However it was obtained with separate high resolution UVES observations, which confirmed the exceptionally high H₂ column density (Balashev et al. 2017).

3.2 Dust-extinction measurements

We obtained the estimates of $E(B - V)$ by fitting a quasar spectral template to the data assuming a fixed extinction curve. Since we observe no indications of the prominent 2175 Å dust feature, we used the extinction curve observed

towards the Small Magellanic Cloud (SMC) as parametrized by Gordon et al. (2003), however, we modified the far UV curvature part using $c_4 = 0$ since this provided a better description of the data. The dust reddening is assumed to be caused solely by the H₂-bearing DLA. We used the quasar template derived by Selsing et al. (2016) and fitted only the data in bona fide continuum regions, i.e., regions which are not strongly affected by absorption or broad emission lines. In the near-infrared, we performed a 5- σ clipping in order to discard outlying pixels introduced by the removal of skylines in the data reduction. Moreover, we masked out pixels that are affected by telluric absorption.

Before fitting, the template by Selsing et al. was smoothed with a Gaussian kernel ($\sigma = 7$ pixels) to prevent the noise in the template to falsely fit noise peaks in the real data. In order to take into account the uncertainty on the template, we subsequently convolved the errors on the observed data with the uncertainty estimate for the template.

We then fitted the template to the data using 3 free parameters: the amount of dust in the absorber, A_V , and the change in the intrinsic power-law index, $\Delta\beta$, as well as a flux scaling, f_0 , since we do not know the intrinsic brightness prior to reddening. The best-fit A_V are given in Table 2. We found that power law indices, $\Delta\beta$, to be between -0.8 and 0.2 for this sample. The typical statistical uncertainties on A_V of such measurements are ~ 0.01 mag. However, there is a strong degeneracy between A_V and the intrinsic power-law shape of the quasar spectrum. We estimated the systematic uncertainty related to the unknown spectral shape by assuming the inferred Gaussian dispersion for β of $\sigma_\beta = 0.19$ (Krawczyk et al. 2015). We drew a random $\Delta\beta$ from a Gaussian centred at $\Delta\beta = 0$ with dispersion σ_β and change the quasar template accordingly. We then refitted the spectra with the newly altered, random template to obtain a distribution of A_V . Based on this distribution, we inferred an estimate of the systematic uncertainty of $\sigma_{\text{sys}} \sim 0.1$ mag. We therefore consider this systematic uncertainty as a conservative estimate of the error on individual measurements.

3.3 Physical conditions

In this section, we derive the temperature and number density of the H₂-bearing gas in our sample as well as the intensity of the UV irradiation onto the clouds. In cases where more than one component is detected in H₂, we use only the strongest component since C I is not always detected for the weaker component. We note however that for one absorber (toward J1146+0743) we are able to properly constrain C I and H₂ in both components, and for both components, we infer consistent results for temperature, density and UV intensity. Also for J0843+0221 we used the total column densities of H₂ and C I, since absorption lines from $J = 0, 1$ H₂ rotational levels damped and two main components are not resolved.

We used the $J = 0$ to $J = 1$ rotational excitation temperature of H₂, T_{01} , as a proxy for the kinetic temperature T_k in the cold diffuse medium (see Roy et al. 2006). The inferred temperatures for the individual systems are given in Table 2. We note that these estimates of the temperature only corresponds to the temperature of the H₂-bearing gas and not the overall DLA gas, for which there most likely is

a contribution from a warm neutral phase with $T \gtrsim 10^3$ K (e.g., Srianand et al. 2012; Neeleman et al. 2015).

In order to constrain the number density and the UV flux in the H₂-bearing medium, we used the relative population of C I fine structure levels (see Silva & Viegas 2002), H₂ rotational levels and the analytical theory of H I-H₂ transition from Sternberg et al. (2014). For C I, we used the same calculations and code as in (Balashev et al. 2017; Ranjan et al. 2018). Here we briefly outline the assumptions used in the analysis. For C I excitation, we assumed a homogeneous medium, where C I fine-structure levels are populated by the Cosmic Microwave Background (CMB) radiation, UV pumping and collisions. The CMB temperature at the absorbers redshift is fixed to be $T_{\text{CMB}}(z) = T_{\text{CMB}}(z = 0)(1 + z)$ (see, e.g., Srianand et al. 2008; Noterdaeme et al. 2011). Since the observed H₂ column densities are high, we assume that the gas phase containing the bulk of C I is fully molecularized (e.g., Balashev et al. 2015), i.e. the main collisional partners are H₂ and He. Due to the relatively low measured C I column densities we neglect self-shielding in C I lines in which UV pumping occurs. Since the collisional coefficients for C I depend on temperature, we fixed the temperature to the measured T_{01} value, reducing the free parameters to be the hydrogen number density (n_{H}) and the intensity of the UV field (I_{UV} , that we express relative to the Draine field). The exact shape of the spectrum cannot be constrained, since it depends on the unknown galaxy's stellar population and ambient conditions. Therefore, we assumed Draine shape for the UV background spectrum. We also added the UV metagalactic background in the calculation. However, at redshifts $z \sim 2 - 3$, it is $\sim 10\div 30$ times lower than the Draine field in the considered wavelength range (see e.g. Khaire & Srianand 2019).

The population of the H₂ rotational levels also provides constraints on the (I_{UV} , n_{H})-plane, and were previously used to estimate the physical conditions in a few high- z H₂-bearing DLAs (e.g., Klimenko et al. 2016; Shaw et al. 2016; Noterdaeme et al. 2017; Rawlins et al. 2018). While UV pumping plays a direct role in the excitation of high rotational level, we are not confident that $J \geq 3$ rotational levels are well constrained (see note in Sect. 3.1). We hence here focus on the excitation of the $J = 0, 1, 2$ levels only. These levels are predominantly thermalised and their excitation typically close to the kinetic temperature (see Le Petit et al. 2006), which is set by the thermal balance, itself being a function of density and UV field. Notwithstanding, UV pumping could also contribute to the excitation of these low- J levels, so that the assumption of a homogeneous cloud is not correct anymore (the resonant H₂ lines –at which pumping occur – quickly saturate inside the cloud). We therefore used the PDR Meudon code (Le Petit et al. 2006) which performs full radiative transfer calculations in H₂ lines. We used grids of pseudo-spherical constant-density models with the only parameters being the metallicity (assuming dust scales to metallicity), density and intensity of UV field. The temperature profile in the cloud was calculated from the solution of thermal balance for each model. We then ran grids of models with ten logarithmically-spaced points for both the number density and UV field intensity in the respective ranges of $0 \leq \log n_{\text{H}}/\text{cm}^{-3} \leq 4$ and $-1.5 \leq \log I_{\text{UV}} \leq 2.5$ (where I_{UV} is measured in Draine field units). For each system, we chose the appropriate grid corresponding to the observed metal-

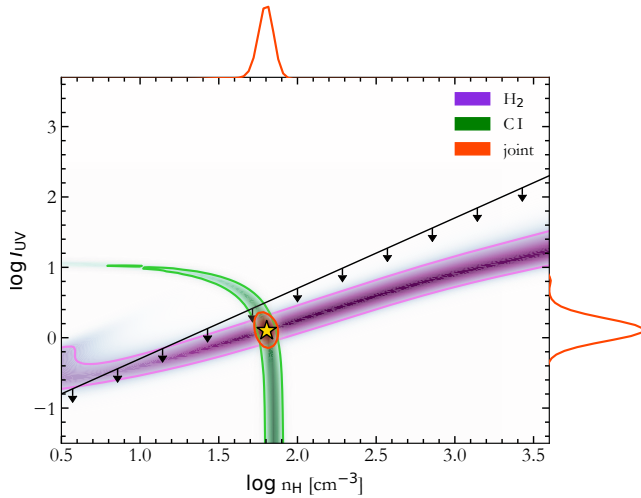


Figure 2. Constraints on the hydrogen number density n_{H} and UV field strength (I_{UV} , in Draine field units) in the H_2 -bearing medium toward SDSS J085859.67+174925.32. The green and violet color gradients represent the obtained probability density function (with the contour lines encompassing 68.3% of it) using excitation of C I fine-structure levels and H_2 rotational levels, respectively. The red contour shows the joint constraint with the star located at the most probable value. The red lines on the top and right axis indicate the marginalized distributions of respectively, n_{H} and I_{UV} from the joint fit. The black line with downward arrows show the constraint obtained from the theoretical H I-H_2 transition in the medium.

licity. We used models assuming a slab of gas with thickness corresponding to $A_{\text{V}} = 0.5$ irradiated from both sides. To compare the modeled and observed column densities of different H_2 rotational levels, we cut the model at a depth in the cloud where half of the total H_2 column density equals half the observed one. This approach mimics a cloud illuminated on both sides with a total column density of H_2 equal to the measured one.

We then compared the modelled excitation of H_2 rotational levels to the observed ones, including a factor of 2 (0.3 dex) uncertainty for the observed H_2 column densities to take account for unknown geometry (the H_2 cloud is likely not exactly spherical). In order to obtain a smooth representation of the results, we interpolated the calculated H_2 excitation on a denser grid in the $n_{\text{H}}-I_{\text{UV}}$ parameter space.

In Fig. 2, we show an example of the constrained regions from C I and H_2 for the DLA towards J0858+1749 using green and purple colors, respectively. The figures for the remaining targets in our sample are shown in the Appendix. Although independently C I and H_2 provide degenerate constraints in the $n_{\text{H}}-I_{\text{UV}}$ parameter space, their constraints are nearly orthogonal allowing us to break the degeneracy. Therefore, a joint fit (shown by the red contour in Fig. 2) provides significantly tighter constraints as evidenced by the marginalized joint probability densities shown on the right and top axes of Fig. 2. The black line in Fig. 2 indicates the constraint on the parameters using the analytical theoretical expression from Bialy et al. (2017), based on the H I-H_2 theory from Sternberg et al. (2014), which relates the H I column density in the envelope of H_2 cloud to the ratio of the UV intensity to density (I_{UV}/n) for a given dust abun-

dance. The latter is assumed here to scale with metallicity. Since neutral gas not directly related to the H_2 -bearing cloud also contributes to the observed $N(\text{H I})$, the constraint following Bialy et al. (2017) results in an upper limit on I_{UV} for a given n_{H} . For all DLAs in our sample, the H I-H_2 transition theory provides constraints in agreement with the joint measurements from C I and H_2 .

The estimates of n_{H} and I_{UV} for our sample are given in Table 2.

4 DISCUSSION

4.1 Comparison between different H_2 -absorber samples

In this section, we compare the chemical properties of various samples of H_2 -bearing DLAs (and sub-DLAs) in the distant Universe: this includes (1) high-redshift systems from this paper based on direct H_2 identification in SDSS spectra of DLAs (Balashev et al. 2014); (2) systems pre-selected using C I without any prior on H I content (Ledoux et al. 2015; Noterdaeme et al. 2018); (3) systems pre-selected based on very high H I column densities (see Noterdaeme et al. 2015; Ranjan et al. 2019); and (4) regular DLAs systems without any further or particular selection (mostly from the VLT/UVES database, see Noterdaeme et al. 2008, Balashev et al. 2017 and references therein, but also from Muzahid et al. 2015, 2016 for low- z systems). For convenience, in the following we will refer to these samples as, respectively, *direct- H_2* , *C i*, *strong-H i* and *blind*.

We note that the H_2 -bearing DLAs towards J0843+0221³ and J1146+0743 belong to both the high- $N(\text{H I})$ and the direct- H_2 selections (Noterdaeme et al. 2014; Balashev et al. 2014).

We also compare the properties of these samples with those observed at $z = 0$ in the local group (Savage et al. 1977; Rachford et al. 2009; Gillmon et al. 2006; Welty et al. 2012). By construction (due to various selection effects) the different samples probe different regions in terms of the redshift, metallicity, H I , and H_2 abundance, which we discuss in the following.

4.1.1 Hydrogen content of molecular absorbers

In Fig. 3, we plot the dependence of H_2 on H I column densities measured in different samples. It can be seen that, for a given H_2 column density, C I-selected systems tend to probe lower H I column densities than the other samples. This can be explained by the absence of any prior on H I for the detection of these systems (Ledoux et al. 2015), and the corresponding sightlines may statistically intercept less unrelated H I gas compared to DLAs. Notwithstanding, when compared to the cosmological H I frequency distribution, the $N(\text{H I})$ -distribution of the C I-selected sample remains skewed towards high values. In other words, the probability to find C I remains higher at higher H I column densities, but the

³ This system has the second highest H_2 column density to date ($\log N(\text{H}_2) = 21.2$, Balashev et al. 2017), only slightly below that towards J1513+0352, selected for its high $N(\text{H I})$ ($\log N(\text{H}_2) = 21.3$, Ranjan et al. 2018).

Table 2. Summary of column densities, chemical enrichment, and physical conditions in the sample.

Quasar	z_{abs}	$\log N(\text{H}_2)$ [cm ⁻²]	$\log N(\text{H I})$ [cm ⁻²]	$\log f$	$\log N(\text{C I})$ [cm ⁻²]	[X/H] ^a	[Fe/X]	A_V ^b	T_{01} [K]	$\log n_{\text{H}}$ [cm ⁻³]	$\log I_{\text{UV}}^c$
J 0136+0440	2.779	18.65 ^{+0.06} _{-0.07}	20.73 ± 0.01	-1.79 ^{+0.06} _{-0.07}	14.67 ^{+0.17} _{-0.15}	-0.58 ^{+0.03} _{-0.03}	-0.70 ^{+0.03} _{-0.04}	0.16	77 ⁺⁷ ₋₆	2.2 ^{+0.1} _{-0.2}	-0.2 ^{+0.2} _{-0.1}
J 0858+1749	2.625	19.72 ^{+0.01} _{-0.02}	20.40 ± 0.01	-0.53 ^{+0.01} _{-0.02}	14.34 ^{+0.04} _{-0.04}	-0.63 ^{+0.02} _{-0.02}	-1.70 ^{+0.03} _{-0.03}	0.29	102 ⁺² ₋₂	1.8 ^{+0.1} _{-0.1}	0.1 ^{+0.2} _{-0.2}
J 0906+0548	2.567	18.88 ^{+0.02} _{-0.02}	20.13 ± 0.01	-1.00 ^{+0.02} _{-0.02}	13.86 ^{+0.06} _{-0.05}	-0.18 ^{+0.05} _{-0.08}	-1.28 ^{+0.08} _{-0.06}	0.21	116 ⁺²⁶ ₋₄	2.6 ^{+0.1} _{-0.1}	0.7 ^{+0.1} _{-0.2}
J 0946+1216	2.607	19.97 ^{+0.01} _{-0.02}	21.15 ± 0.02	-0.93 ^{+0.02} _{-0.03}	14.43 ^{+0.05} _{-0.05}	-0.48 ^{+0.01} _{-0.01}	-0.77 ^{+0.01} _{-0.01}	0.25	118 ⁺⁹ ₋₈	2.3 ^{+0.1} _{-0.1}	0.5 ^{+0.2} _{-0.2}
J 1146+0743	2.840	18.82 ^{+0.03} _{-0.02}	21.54 ± 0.01	-2.42 ^{+0.03} _{-0.02}	13.91 ^{+0.09} _{-0.07}	-0.57 ^{+0.02} _{-0.02}	-0.67 ^{+0.02} _{-0.02}	0.17	101 ⁺¹² ₋₉	2.6 ^{+0.2^c} _{-0.2}	0.6 ^{+0.2^d} _{-0.2}
J 1236+0010	3.033	19.76 ^{+0.01} _{-0.01}	20.78 ± 0.01	-0.80 ^{+0.01} _{-0.01}	14.11 ^{+0.08} _{-0.07}	-0.58 ^{+0.04} _{-0.03}	-1.09 ^{+0.04} _{-0.04}	0.07	118 ⁺⁷ ₋₆	1.5 ^{+0.6} _{-0.6}	0.4 ^{+0.4} _{-0.4}
J 2347-0051	2.588	19.44 ^{+0.01} _{-0.01}	20.47 ± 0.01	-0.80 ^{+0.01} _{-0.01}	14.05 ^{+0.37} _{-0.25}	-0.82 ^{+0.05} _{-0.03}	-0.71 ^{+0.03} _{-0.05}	0.04	76 ⁺² ₋₂	2.0 ^{+0.4} _{-0.5}	-0.4 ^{+0.4} _{-0.3}
J 0843+0221	2.786	21.21 ^{+0.02} _{-0.02}	21.82 ± 0.11	-0.48 ^{+0.08} _{-0.08}	13.98 ^{+0.04} _{-0.04}	-1.52 ^{+0.08} _{-0.10}	-1.01 ^{+0.07} _{-0.05}	< 0.1	123 ⁺⁹ ₋₈	2.82 ^{+0.05} _{-0.06}	1.18 ^{+0.24} _{-0.17}

(a) For all systems the metallicity given here is based on the abundance of sulphur, except for that towards J 1146+0743 for which we used zinc because S II lines are blended.

(b) The typical statistical uncertainty on A_V is 0.01 mag, but the systematic uncertainty due to intrinsic spectral slope variations is 0.1 mag (see text).

(c) In units of the Draine field.

(d) For the system towards J 1146+0743, the estimated number density in the two components is similar. Here we give the value corresponding to the strongest H₂ component.

overwhelming incidence of neutral absorption systems with low $N(\text{H I})$ (e.g., [Noterdaeme et al. 2012b](#)) makes them over-represented in the C I sample.

The *blind* sample should in principle be more representative of the overall DLA population. However, while the corresponding H₂-bearing systems indeed cover a wide range of H I column densities, there is an excess of high-H I systems. This reflects not only the increasing H₂-detection probability with increasing $N(\text{H I})$ but also a bias towards high- $N(\text{H I})$ in the UVES DLA/sub-DLA database ([Noterdaeme et al. 2008](#)). Since these systems were mostly observed in high spectral resolution, high-S/N data, the corresponding detection limits can indeed be as low as $N(\text{H}_2) \sim 10^{14}$ cm⁻², so that systems with low molecular content (e.g., [Noterdaeme et al. 2007](#)) are also present in the figure.

The strong-H I sample, by construction, probes the high end of H I column densities. Although the incidence rate of H₂ in that sample is quite high, ~ 50 per cent, the actual H₂ column densities correspond to a very wide range⁴, including the two highest H₂ column densities found in ESDLAs, towards J 0843+0221 and J 1513+0352 ([Balashev et al. 2017](#); [Ranjan et al. 2018](#)).

Finally, the direct H₂-selection in SDSS is, by construction, mostly limited to high H₂ column densities, typically $\log N(\text{H}_2) > 19$, that produce detectable lines at low spectral resolution. In addition, the search was limited to DLAs and strong sub-DLAs ($\log N(\text{H I}) \geq 20$) from the SDSS catalogue ([Noterdaeme et al. 2012b](#)). We note that six out of eight H₂-selected systems have high average molecular fractions, as seen for C I-selected systems. In the case of the latter, the presence of C I depends on the abundance of carbon (hence the metallicity) and the shielding from UV photons, both

favouring high molecular fractions, as discussed in next section. In the case of the former, by selection we restrict to high H₂-column density systems when the H I frequency distribution decreases with increasing H I column density, also favouring high-molecular fraction systems.

4.1.2 Dependence on metallicity

Aside from the obvious differences in H₂ and H I column densities, the different pre-selection techniques also exhibit prominent differences in the probed metallicities and redshifts. In Fig. 4 we show metallicity as a function of redshift and H I column density. We here use metallicities based on volatile species, i.e. either sulphur or zinc (e.g., [Vladilo et al. 2011](#)) depending on the line coverage and possible blends.

From the left panel of Fig. 4, it can be seen that different samples probe slightly different redshifts. The obvious reason for this is that each selection utilizes a different redshift cutoff depending on the instrument used, the atmospheric cutoff in the blue, and the rest-frame wavelength of the transitions used for detection. Indeed, C I lines are detectable down to lower redshifts than H I, while the observation of H₂ lines in SDSS spectra requires even higher-redshifts than for H I. Note that the sensitivity functions, $g(z)$, of the samples increases with decreasing redshift, and therefore the density of points is enhanced close to their respective redshift cutoff.

H₂-bearing DLAs mainly occupy the upper half of the overall observed DLA metallicity distribution, consistent with previous works (e.g., [Petitjean et al. 2006](#)). While the C I-selected systems probe mostly the high-end of the H₂-bearing DLA metallicity distribution (and consequently of the overall DLA distribution, [Ledoux et al. in prep.](#)), the strong-H I-selected sample corresponds to low metallicity H₂-bearing systems. The direct H₂ selection tends to probe metallicities in between those of C I and ESDLAs and this

⁴ Note that most ESDLAs were followed up at intermediate resolution using the X-shooter spectrograph, thus formally reported non-detections of H₂ actually correspond to upper limits of $\log N(\text{H}_2) \gtrsim 16 - 17$.

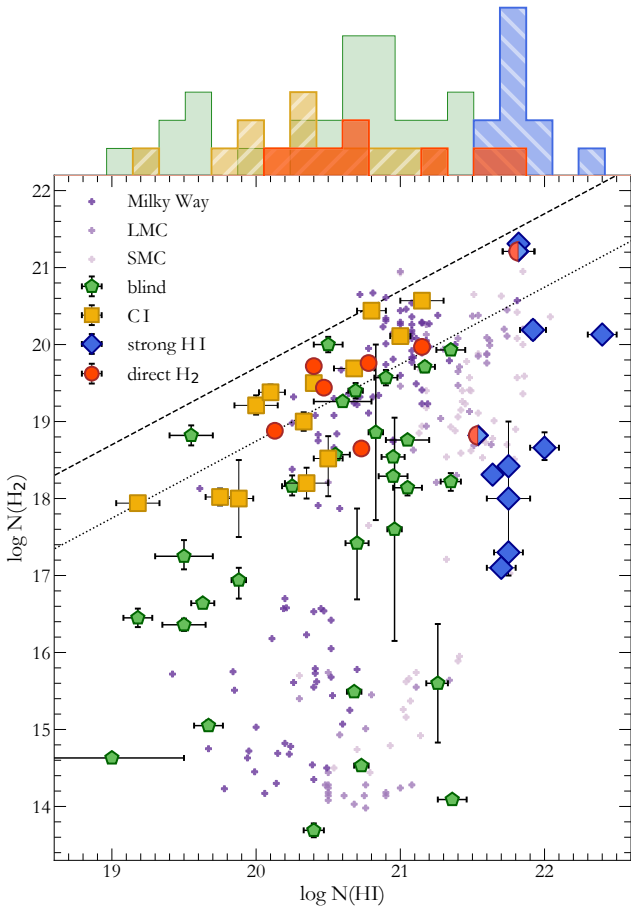


Figure 3. The dependence of $\log N(\text{H}_2)$ on $\log N(\text{H I})$ measured in absorption at high redshift and locally. The green pentagons, blue diamonds and yellow squares represent H_2 -bearing DLAs from the ‘blind’, C I and strong-H I selections, respectively. The sample presented in this paper and concerned with direct- H_2 detection is shown by red circles. Note that two systems, towards J 0843+0221 and J 1146+0743, belong to both the H_2 and the H I-selections and the symbols are then half red circle, half blue diamond. The measurements in the local galaxies (Milky Way, LMC and SMC) are shown by purple crosses with slightly different hue. The dashed and dotted lines depict constant average molecular fractions of 0.5 and 0.1, respectively. The histograms on top show the $N(\text{H I})$ -distributions for the different samples using the same colour coding.

remains evident even after taking into account the small redshift evolution of metallicity.

The metallicity actually plays a dominant role in the detectability of C I lines for a given H I column density. Not only does a high metallicity imply a high carbon abundance, but it also promotes the survival of C I through shielding by dust and H_2 , both of which scale with metallicity. Therefore the C I-selection predominantly picks out high metallicity systems, in particular at low $N(\text{H I})$ (Noterdaeme et al. 2018; Zou et al. 2018, Ledoux et al. (in prep)). Interestingly, for a given metallicity, the H_2 column densities in C I-selected systems increases with increasing $N(\text{H I})$. Since theoretical models of H I- H_2 conversion indicate that the H I envelope of a single cloud has almost constant column density whatever

the $N(\text{H}_2)$ (i.e. more gas added to a cloud is converted to H_2), this could indicate the interception of multiple H I- H_2 layers. This is consistent with a higher probability to find cold gas close to a given cold gas cloud, either along the same line of sight (appearing as multiple components, see Ledoux et al. in prep), or transversely (Krogager et al. 2018b).

The chemical conditions for the presence of H_2 at detectable levels are less restrictive than those for C I, allowing the direct H_2 and strong H I-selections to probe lower metallicities. Furthermore, in the high H I column density regime, the presence of H_2 in a given system appears to be little dependent on the metallicity. Indeed, the DLA towards J 0843+0221 has a very high H I and H_2 content despite its low metallicity, and the metallicity distribution of H_2 -bearing ESDLAs is not significantly different from that of non H_2 -bearing ESDLAs (see Fig. 4). The local physical conditions (density and UV field) seem to play a more important role for these systems. Indeed, these systems are expected to probe small galacto-centric distances (Noterdaeme et al. 2014; Ranjan et al. 2019), where the pressure could be increased (in theoretical models of warm and cold gas distribution in galaxies Wolfire et al. 2003). We also note that high- $N(\text{H I})$ DLAs with high metallicities could be under-represented among them due to the associated dust reddening. This could exclude the background quasars from optically-selected samples (see, e.g., Geier et al. 2019; Krogager et al. 2019) and lead to infeasible amounts of observing time required for spectroscopic follow-up.

The intermediate metallicities seen for the H_2 -selected sample suggest that the intrinsic metallicity distribution of H_2 -bearing systems is shifted compared to that of the overall DLA population. However, the paucity of low-metallicity systems in the direct H_2 sample in comparison to H_2 -bearing ESDLAs, if real, can be due also to differences in physical conditions. The presence of H_2 depends not only on the metallicity and column density but also on the number density (n) and intensity of the UV field (I_{UV}). To understand this further, we compare the observed $N(\text{H I})$ and metallicities with the theoretical expectation from the work by Bialy & Sternberg (2016). We caution that the theoretical predictions are only valid for a single cloud whereas the actual situation is more likely a concatenation of H_2 clouds along the line of sight embedded in a diffuse and warm H I phase that also contributes to the measured H I column density. In that sense, all measured values of $N(\text{H I})$ are upper limits to the H I column density associated with the envelope of the H_2 cloud. The different theoretical lines should therefore be regarded as the minimal conditions for H I/ H_2 transition at a given metallicity and H I column density. That is, the calculated H I column densities are only applicable for systems where a transition from H I to H_2 has occurred. For the typical ranges of the physical conditions in the cold ISM (mainly, the metallicity, number density and UV flux) this corresponds to a H_2 column density larger than $\log N(\text{H}_2) \sim 18 - 20$. Therefore we highlight the points correspond to different ranges of H_2 column densities in Fig. 3 using color saturation. The blank points represent the lowest H_2 column densities ($\log N(\text{H}_2) < 18$) for which the model lines are most likely not applicable. Almost all saturated H_2 -bearing DLAs, regardless of their selection, are located in between the $I_{\text{UV}}/n_{\text{H}} \sim 10^{-3}$ and $I_{\text{UV}}/n_{\text{H}} \sim 1$ lines. Systems with low metallicity and H I column density

would require very low I_{UV}/n_H ratios (below $\lesssim 10^{-3}$) in order to efficiently form H₂. High density systems with low total column density must have very small physical dimensions leading to a low absorption cross-section. This is consistent with the absence of H₂ among such absorption-selected samples. For example, for a given UV field typical of our Galaxy (i.e. $I_{UV} = 1$) this correspond to $n \gtrsim 10^3 \text{ cm}^{-3}$. Therefore at column density at the DLA threshold, and metallicity typical of DLAs ($[X/H] \sim -1.3$), a cloud should be compressed less than $< 0.1 \text{ pc}$ in order to H₂ to form. For a temperature of $T \sim 100 \text{ K}$, this also means a thermal pressure $P \sim 10^5 \text{ K cm}^{-3}$, which is not very common, especially at low $N(\text{H I})$.

To summarize, the three preselection methods presented above complement each other and enable us to study the physical conditions and the H₂/H I transition in a wide range of environments.

4.1.3 Fe depletion and dust

In previous discussions, we did not differentiate between the metallicity and dust content, assuming that the dust content directly scales with the metallicity. However, the presence of H₂ is directly linked to the dust content, since the formation of molecules occurs on the surface of dust grains that also participate to the shielding of UV photons. Unfortunately, the large systematic uncertainties of the A_V measurements, compared to the actual (low) values, prevent us from quantifying the dust content directly from the measured extinction. Instead, we can use the depletion of refractory elements (like iron) compared to volatile ones (zinc or sulphur). All samples follow a similar trend of increasing Fe depletion with increasing metallicity, as illustrated in Fig. 5, reflecting the scaling of dust with metallicity (see Ledoux et al. 2003). Since the H₂ formation rate is roughly proportional to the dust abundance, we might statistically expect an enhanced depletion for H₂-bearing DLAs at a given metallicity. However, we do not clearly observe such a behaviour: only two out of eight DLAs in our sample have a significant stronger depletion (i.e. lower $[\text{Fe}/X]$) than seen from the overall DLA population at their given metallicity. This can be due to a fact that the quantities used for comparison are averaged throughout the absorption complexes⁵. More importantly, the dependence on average depletion shown in Fig. 5 doesn't take into account the column densities. Observationally, it is already known that the total column of the dust probably plays a major role in the presence of H₂ at detectable levels (see Noterdaeme et al. 2008). The physical reason is that larger dust column imply larger shielding from UV photons, either directly from the dust grains, or indirectly provided by H₂ self-shielding (since the more dust, the higher H₂ formation rate and the larger H₂ column density). In Fig. 6 we show the dependence of the H₂ column density on the column density of iron locked into dust, which provides a way to quantify the column density of dust (Vladilo et al. 2006). Overall, the different samples are not distinguishable

⁵ See, e.g., the H₂-bearing DLA towards J 0000+0048, where the detailed analysis of high-resolution data indicates that the H₂-bearing component is significantly more depleted than the average over all DLA components.

in this Figure and confirm the neat increase in the H₂ column densities at $\log N(\text{Fe}_{\text{dust}}) \gtrsim 15$. This suggests that the physical conditions (ratio of UV to number density) should not be drastically different for different H₂ samples, since the critical $N(\text{Fe}_{\text{dust}})$ is mostly defined by this ratio (see, e.g., Bialy et al. 2017). For given physical conditions, an increasing $N(\text{H}_2)$ with increasing $N(\text{Fe}_{\text{dust}})$ could then be expected at higher dust column, regardless of whether this is due to a concatenation of several transition layers seen along a line of sight, or single clouds with larger column densities. Such a correlation may possibly be seen in the C I-selected sample which possibly share more homogeneous conditions.

4.2 Physical conditions

We find values of the temperature in the range 75-120 K, with a median of $T \sim 100 \text{ K}$ ⁶. These values are slightly higher than what is measured towards nearby stars ($T \sim 80 \text{ K}$, see, e.g., Savage et al. 1977), but lower than previously seen in the overall population of high- z DLAs ($T \sim 150 \text{ K}$; Srianand et al. 2005). However, T_{01} temperatures in H₂-bearing DLAs are known to decrease with increasing H₂ column density (Muzahid et al. 2015; Balashev et al. 2017), a trend also seen in the local ISM. The systems in our sample have typically higher H₂ column densities than those from Srianand et al. (2005), but lower than towards nearby stars, that can explain the difference. However, from our sample alone, we do not see any trend in T_{01} vs. $\log N(\text{H}_2)$, though our measurements are still within the measured dispersion of T_{01} . Metallicity could also play a role to explain the differences in the temperatures since it plays an important role in the thermal balance (e.g., Wolfire et al. 2003). Indeed, the cooling is dominated by line emission (in particular [C II] at $158 \mu\text{m}$) while the heating is dominated by photoelectric effect on dust grains. Both these processes are directly linked to the gas metallicity. Observationally, a low H₂ temperature of $T \sim 50 \text{ K}$ was measured in the super-Solar metallicity DLA towards J 0000+0048 (Noterdaeme et al. 2017) while higher temperatures were measured at low metallicities, $[X/H] \lesssim -1$ towards J 0843+0221 and J 1513+0352 (Balashev et al. 2017; Ranjan et al. 2018). However, since the photo-electric heating involves UV photons, the intensity of the UV field directly plays an important role. Indeed, one can see in Fig. 7, where the estimated UV flux is coded by the color saturation, that our sample (for which most systems span a narrow range of the metallicity) supports such a dependence. We can further speculate that, knowing the gas metallicity, the relative $J = 1/J = 0$ population of H₂ could give a useful diagnostic of the UV to density ratio, without the need of detailed modelling.

We found a typical hydrogen number density of $n \gtrsim 100 \text{ cm}^{-3}$ and typical UV field on average twice higher than the Draine field. The obtained number densities and kinetic temperatures agree well with the canonical values for the cold ISM in the two-phase model from Wolfire et al. (2003). This shows that H₂ is a good tracer of the CNM in DLAs. This is particularly useful since 21-cm absorption studies

⁶ We note that this value corresponds to the temperature of the H₂-bearing gas and not the overall DLA system, which is more likely characterized by a warm neutral phase with $T \gtrsim 10^3 \text{ K}$.

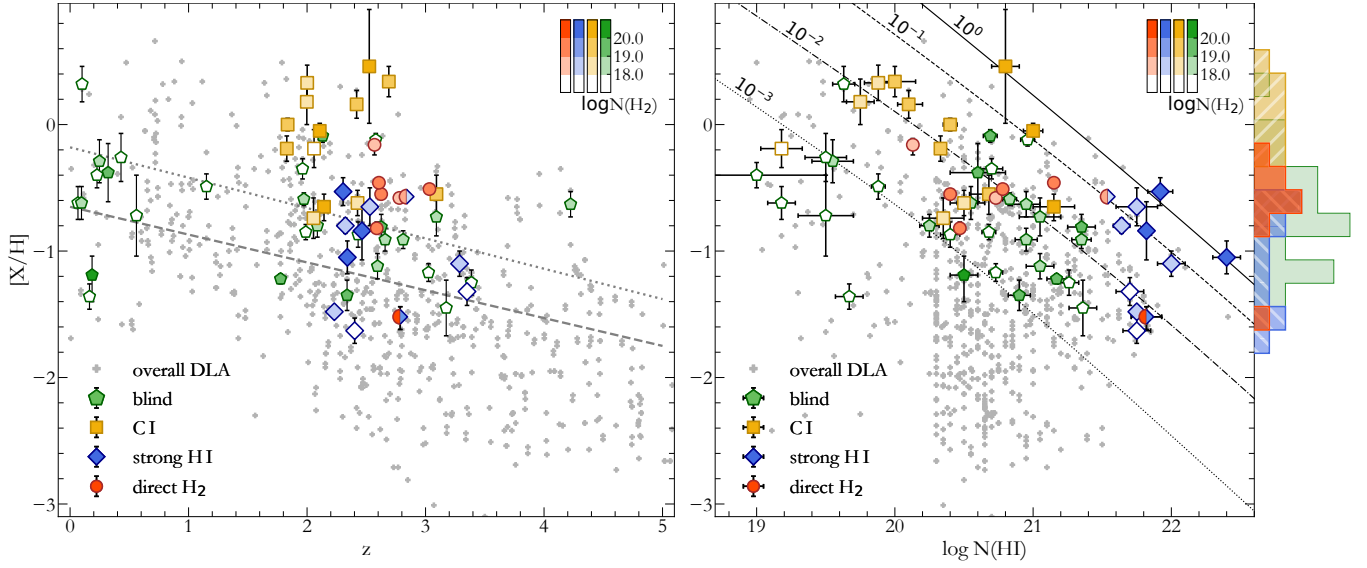


Figure 4. The metallicity as a function of the redshift (left panel) and $\log N(\text{H I})$ (right panel) measured in DLAs. The symbols are the same as in Fig. 3 with colour saturation representing the H_2 column density. The mean metallicity in DLAs as a function of redshift is shown on the left panel by dash (Rafelski et al. 2012) and dotted ($N(\text{H I})$ weighted and depletion corrected, see De Cia et al. 2018) lines. The different lines in the right panel correspond to the $N(\text{H I})$ in the envelope of a single H_2 cloud (Bialy et al. 2017) for the different ratios of the UV field to the number density, I_{UV}/n , where I_{UV} is expressed in units of the Draine field and the n in units of cm^{-3} .

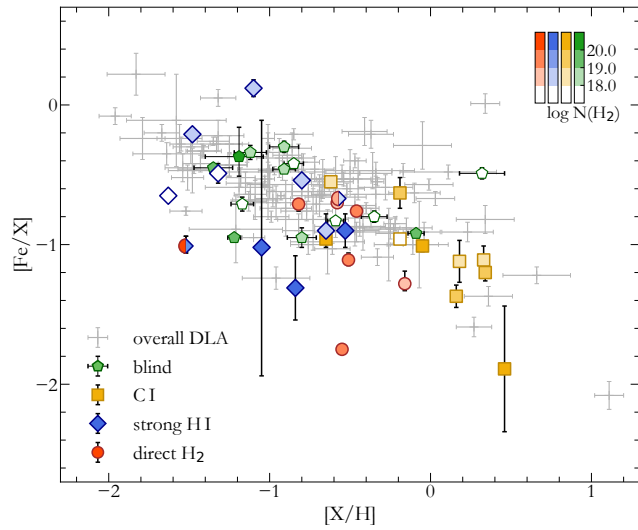


Figure 5. The depletion versus metallicity in DLA at high redshifts. Symbols and color encoding are the same as in Fig. 4.

remain limited at high redshift (Srianand et al. 2012), due to the paucity of strong compact radio sources observable with current facilities (but see Gupta et al. 2016, for future prospects).

Using our estimates of the number density and temperature, we compare the thermal pressures ($P/k = nT$) to those seen in other H_2 -bearing DLAs as well as in the local group in Fig. 8. Our sample probes a wide range of hydrogen column densities, from values similar to that of the Magellanic clouds (Welty et al. 2016) down to about an order of magnitude lower than in the Milky Way (Jenkins & Tripp 2011). The pressure in our sample is about $\sim 10^4 \text{ K cm}^{-3}$

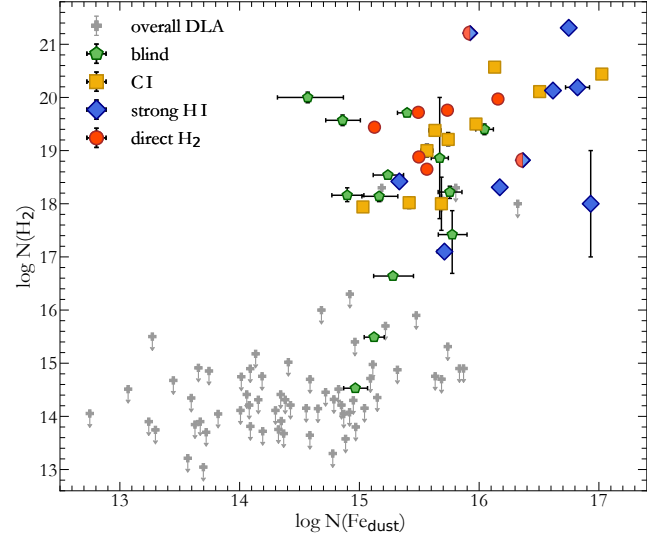


Figure 6. H_2 column density versus column density of Iron in the dust. Symbols and color encoding are the same as in Fig. 4. The grey crosses show the upper limits for DLAs taken from Norderdaeme et al. 2008; Ranjan et al. 2019.

with 0.5 dex dispersion around this value, similar to what is seen locally. Our data further strengthen the suggestion from Balashev et al. (2017) that the thermal pressure increases with the hydrogen column density. This is likely the consequence of both the pressure and the column density to increase with decreasing galacto-centric radius.

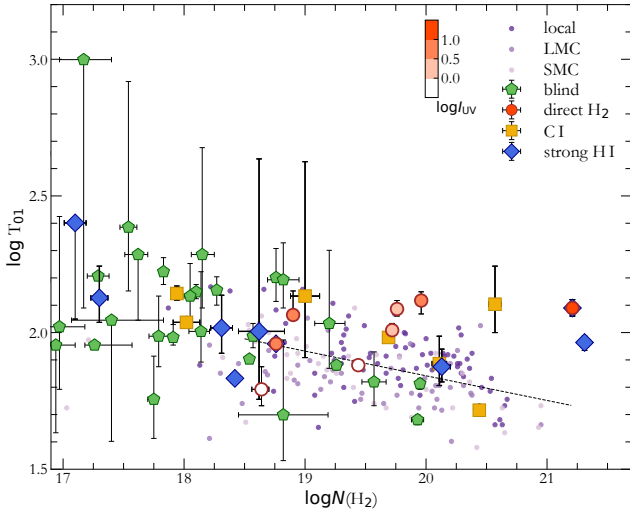


Figure 7. The excitation temperature T_{01} versus column density of molecular hydrogen. Symbols are as per Fig. 3, with colour-filling for the sample presented here (red-circles) representing the inferred intensity of the UV field (see enclosed colour bar).

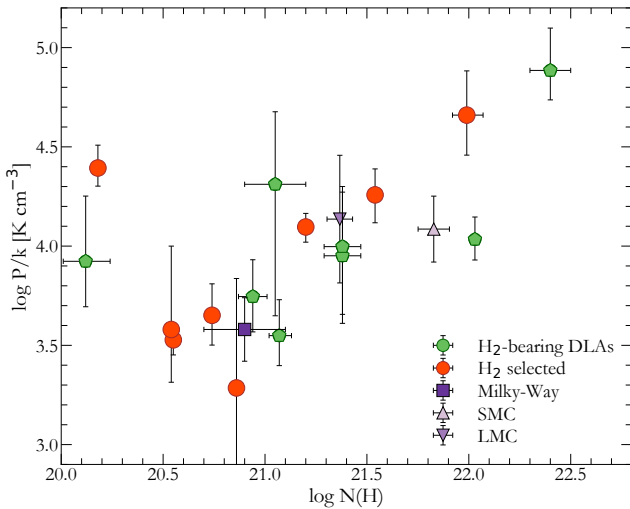


Figure 8. The dependence of the thermal pressure $P/k = nT$ on $\log N(H_{\text{tot}})$ measured in DLAs (circles) and local galaxies (square and triangles). Green and red circles correspond to the known $H_2/C\text{I}$ bearing DLAs at high redshift and our sample, respectively.

5 CONCLUSION

We presented follow-up observations with the X-shooter spectrograph on the Very Large Telescope of seven strong H_2 -bearing DLAs at high redshifts. These DLAs were selected from the SDSS DLA catalogue (see [Noterdaeme et al. 2012b](#)) directly upon the presence of H_2 Lyman bands seen in the SDSS spectra of their background quasars, see [Balashev et al. \(2014\)](#). Our X-shooter observations confirm the detection of H_2 in all systems and hence the high efficiency of the direct H_2 detection method even at low spectral resolution. We measured the neutral, molecular, and metal column

densities of the systems and found typical H_2 column densities in the range $\log N(H_2) = 18.5 - 20$, when the H I column density span a range $\log N(H\text{I}) \sim 20.1 - 21.5$. The metallicities, obtained from undepleted species, are in the range $\log Z = -0.8$ to -0.2 . Finally, in all systems, we detected absorption lines from C I in various fine-structure energy levels associated to the H_2 components. We used the rotational excitation of H_2 , the fine-structure excitation of C I, and theoretical relations for the H I- H_2 transition to estimate the physical conditions in the H_2 -bearing gas. We found a typical kinetic temperature of ~ 100 K and hydrogen densities $n_{\text{H}} \sim 100 \text{ cm}^{-3}$, within clouds embedded in a UV field about twice higher than the Draine field. This confirms that H_2 is a good tracer of the cold neutral medium⁷.

Comparing our sample with other samples of H_2 -bearing DLAs and sub-DLAs selected differently, we discuss how the selection methods probe different regimes of column density and chemical enrichment and how the presence of H_2 depends on the physical conditions. We show that all these methods complement each other and by the SDSS limitation tend to select high H_2 column-density systems that can be efficiently used to study the H I- H_2 transition.

ACKNOWLEDGEMENTS

We thank the referee for useful comments and suggestions. This paper was supported by RSF grant 18-12-00301. PN and JKK acknowledge support from the *French Agence Nationale de la Recherche*, under grant ANR-17-CE31-0011-01 (Projet "HIH2", PI Noterdaeme) and from the CNRS-RFBR Russian-French grant PRC No 1845 (PI Noterdaeme). We are also grateful to the Institut d'Astrophysique de Paris (SB and VK) and to the Ioffe Institute in Saint Petersburg (PN and JKK) for hospitality when part of this work was achieved.

REFERENCES

- Altay G., Theuns T., Schaye J., Booth C. M., Dalla Vecchia C., 2013, *MNRAS*, **436**, 2689
- Balashev S. A., Noterdaeme P., 2018, *MNRAS*, **478**, L7
- Balashev S. A., Varshalovich D. A., Ivanchik A. V., 2009, *Astronomy Letters*, **35**, 150
- Balashev S. A., Klimenko V. V., Ivanchik A. V., Varshalovich D. A., Petitjean P., Noterdaeme P., 2014, *MNRAS*, **440**, 225
- Balashev S. A., Noterdaeme P., Klimenko V. V., Petitjean P., Srianand R., Ledoux C., Ivanchik A. V., Varshalovich D. A., 2015, *A&A*, **575**, L8
- Balashev S. A., Zavarygin E. O., Ivanchik A. V., Telikova K. N., Varshalovich D. A., 2016, *Monthly Notices of the Royal Astronomical Society*, **458**, 2188
- Balashev S. A., et al., 2017, *MNRAS*, **470**, 2890
- Bialy S., Sternberg A., 2016, *ApJ*, **822**, 83
- Bialy S., Bihl S., Beuther H., Henning T., Sternberg A., 2017, *ApJ*, **835**, 126
- Bigiel F., Leroy A., Walter F., Brinks E., de Blok W. J. G., Madore B., Thornley M. D., 2008, *AJ*, **136**, 2846

⁷ However, [Srianand et al. \(2012\)](#) noted there is no one-to-one correspondence between the population of cold gas traced by H_2 and that traced by H I 21-cm absorption.

- Carswell R. F., Webb J. K., 2014, VPFIT: Voigt profile fitting program (ascl:1408.015)
- De Cia A., Ledoux C., Petitjean P., Savaglio S., 2018, *A&A*, **611**, A76
- Freudling W., Romaniello M., Bramich D. M., Ballester P., Forchi V., García-Dab16 C. E., Moehler S., Neeser M. J., 2013, *A&A*, **559**, A96
- Ge J., Bechtold J., Kulkarni V. P., 2001, *ApJ*, **547**, L1
- Geier S. J., et al., 2019, *A&A*, **625**, L9
- Genzel R., et al., 2012, *ApJ*, **746**, 69
- Gillmon K., Shull J. M., Tumlinson J., Danforth C., 2006, *ApJ*, **636**, 891
- Goodman J., Weare J., 2010, *Communications in Applied Mathematics and Computational Science*, **5**, 65
- Gordon K. D., Clayton G. C., Misselt K. A., Landolt A. U., Wolff M. J., 2003, *ApJ*, **594**, 279
- Gupta N., et al., 2016, in Proceedings of MeerKAT Science: On the Pathway to the SKA. 25-27 May, 2016 Stellenbosch, South Africa (MeerKAT2016).. p. 14 ([arXiv:1708.07371](https://arxiv.org/abs/1708.07371))
- Horne K., 1986, *PASP*, **98**, 609
- Ivanchik A. V., Petitjean P., Balashev S. A., Srianand R., Varshalovich D. A., Ledoux C., Noterdaeme P., 2010, *MNRAS*, **404**, 1583
- Jenkins E. B., Tripp T. M., 2011, *ApJ*, **734**, 65
- Jorgenson R. A., Wolfe A. M., Prochaska J. X., Carswell R. F., 2009, *ApJ*, **704**, 247
- Jorgenson R. A., Murphy M. T., Thompson R., Carswell R. F., 2014, *MNRAS*, **443**, 2783
- Khaire V., Srianand R., 2019, *Monthly Notices of the Royal Astronomical Society*, **484**, 4174
- Klimenko V. V., Balashev S. A., Ivanchik A. V., Varshalovich D. A., 2016, *Astronomy Letters*, **42**, 137
- Krawczyk C. M., Richards G. T., Gallagher S. C., Leighly K. M., Hewett P. C., Ross N. P., Hall P. B., 2015, *AJ*, **149**, 203
- Krogager J.-K., 2018, VoigtFit: Absorption line fitting for Voigt profiles (ascl:1811.016)
- Krogager J. K., Møller P., Fynbo J. P. U., Noterdaeme P., 2017, *MNRAS*, **469**, 2959
- Krogager J. K., et al., 2018a, *A&A*, **619**, A142
- Krogager J. K., et al., 2018b, *A&A*, **619**, A142
- Krogager J.-K., Fynbo J. P. U., Møller P., Noterdaeme P., Heintz K. E., Pettini M., 2019, *MNRAS*, **486**, 4377
- Krumholz M. R., 2012, *ApJ*, **759**, 9
- Lacour S., Ziskin V., Hébrard G., Oliveira C., André M. K., Ferlet R., Vidal-Madjar A., 2005, *ApJ*, **627**, 251
- Le Petit F., Nehmé C., Le Bourlot J., Roueff E., 2006, *ApJS*, **164**, 506
- Ledoux C., Petitjean P., Srianand R., 2003, *MNRAS*, **346**, 209
- Ledoux C., Noterdaeme P., Petitjean P., Srianand R., 2015, *A&A*, **580**, A8
- Liszt H. S., 1981, *ApJ*, **246**, L147
- Ma J., et al., 2015, *MNRAS*, **454**, 1751
- Michałowski M. J., et al., 2015, *A&A*, **582**, A78
- Muzahid S., Srianand R., Charlton J., 2015, *MNRAS*, **448**, 2840
- Muzahid S., Kacprzak G. G., Charlton J. C., Churchill C. W., 2016, *ApJ*, **823**, 66
- Neeleman M., Prochaska J. X., Wolfe A. M., 2015, *ApJ*, **800**, 7
- Noterdaeme P., Ledoux C., Petitjean P., Le Petit F., Srianand R., Smette A., 2007, *A&A*, **474**, 393
- Noterdaeme P., Ledoux C., Petitjean P., Srianand R., 2008, *A&A*, **481**, 327
- Noterdaeme P., Petitjean P., Ledoux C., López S., Srianand R., Vergani S. D., 2010, *A&A*, **523**, A80
- Noterdaeme P., Petitjean P., Srianand R., Ledoux C., López S., 2011, *A&A*, **526**, L7
- Noterdaeme P., et al., 2012a, *A&A*, **540**, A63
- Noterdaeme P., et al., 2012b, *A&A*, **547**, L1
- Noterdaeme P., Petitjean P., Pâris I., Cai Z., Finley H., Ge J., Pieri M. M., York D. G., 2014, *A&A*, **566**, A24
- Noterdaeme P., Petitjean P., Srianand R., 2015, *A&A*, **578**, L5
- Noterdaeme P., et al., 2017, *A&A*, **597**, A82
- Noterdaeme P., Ledoux C., Zou S., Petitjean P., Srianand R., Balashev S., López S., 2018, *A&A*, **612**, A58
- Noterdaeme P., Balashev S., Krogager J. K., Srianand R., Fathivavsari H., Petitjean P., Ledoux C., 2019, *A&A*, **627**, A32
- Petitjean P., Ledoux C., Noterdaeme P., Srianand R., 2006, *A&A*, **456**, L9
- Rachford B. L., et al., 2009, *The Astrophysical Journal Supplement Series*, **180**, 125
- Rafelski M., Wolfe A. M., Prochaska J. X., Neeleman M., Mendez A. J., 2012, *ApJ*, **755**, 89
- Ranjan A., et al., 2018, *A&A*, **618**, A184
- Ranjan A., Noterdaeme P., Krogager J.-K., Petitjean P., Srianand R., Balashev S., Gupta N., Ledoux C., 2019, submitted to *A&A*
- Rawlins K., Srianand R., Shaw G., Rahmani H., Dutta R., Chacko S., 2018, *MNRAS*, **481**, 2083
- Roy N., Chengalur J. N., Srianand R., 2006, *MNRAS*, **365**, L1
- Savage B. D., Bohlin R. C., Drake J. F., Budich W., 1977, *ApJ*, **216**, 291
- Schruba A., et al., 2011, *AJ*, **142**, 37
- Selsing J., Fynbo J. P. U., Christensen L., Krogager J. K., 2016, *A&A*, **585**, A87
- Shaw G., Rawlins K., Srianand R., 2016, *MNRAS*, **459**, 3234
- Silva A. I., Viegas S. M., 2002, *MNRAS*, **329**, 135
- Srianand R., Petitjean P., Ledoux C., Ferland G., Shaw G., 2005, *MNRAS*, **362**, 549
- Srianand R., Noterdaeme P., Ledoux C., Petitjean P., 2008, *A&A*, **482**, L39
- Srianand R., Gupta N., Petitjean P., Noterdaeme P., Ledoux C., Salter C. J., Saikia D. J., 2012, *MNRAS*, **421**, 651
- Sternberg A., Le Petit F., Roueff E., Le Bourlot J., 2014, *ApJ*, **790**, 10
- Vernet J., et al., 2011, *A&A*, **536**, A105
- Vladilo G., Centurión M., Levshakov S. A., Péroux C., Khare P., Kulkarni V. P., York D. G., 2006, *A&A*, **454**, 151
- Vladilo G., Abate C., Yin J., Cescutti G., Matteucci F., 2011, *A&A*, **530**, A33
- Welty D. E., Xue R., Wong T., 2012, *ApJ*, **745**, 173
- Welty D. E., Lauroesch J. T., Wong T., York D. G., 2016, *ApJ*, **821**, 118
- Wolfe A. M., Gawiser E., Prochaska J. X., 2005, *Annual Review of Astronomy and Astrophysics*, **43**, 861
- Wolfire M. G., McKee C. F., Hollenbach D., Tielens A. G. G. M., 2003, *ApJ*, **587**, 278
- York D. G., et al., 2000, *AJ*, **120**, 1579
- Zou S., Petitjean P., Noterdaeme P., Ledoux C., Krogager J. K., Fathivavsari H., Srianand R., López S., 2018, *A&A*, **616**, A158
- Zwaan M. A., Prochaska J. X., 2006, *ApJ*, **643**, 675

APPENDIX A: SUPPLEMENTARY MATERIAL

In this section we present the detailed results of the analysis of each DLA individually.

A1 SDSS J013644.02+044039.00

We measured the H I column density of the DLA at $z = 2.779$ towards J0136+0440 by fitting the Ly α absorption line. We fitted together the continuum using sixth order Chebyshev polynomial in the region of Ly α line with a one-component

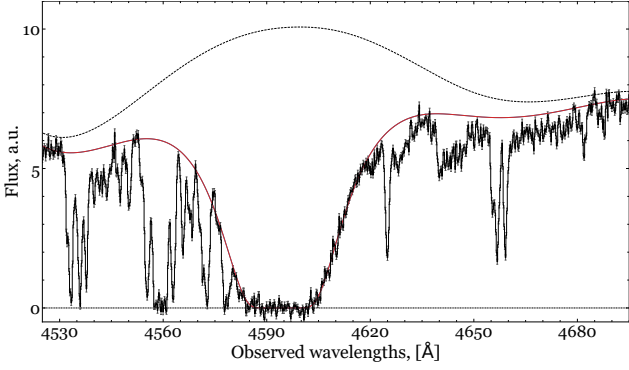


Figure A1. Fit to H I Ly α absorption line in DLA at $z = 2.779$ towards J0136+0440.

Table A1. Fitting results of H₂ towards J0136+0440.

comp.	1	2	$\log N_{\text{tot}}$
z	$2.77901^{(+7)}_{(-4)}$	$2.77943^{(+4)}_{(-7)}$	
Δv , km s ⁻¹	0.0	29.9	
b , km s ⁻¹	$13.2^{+1.7}_{-3.2}$	$7.7^{+2.4}_{-1.9}$	
$\log N(\text{H}_2 \text{ J0})$	$16.49^{+0.32}_{-0.17}$	$18.42^{+0.08}_{-0.08}$	$18.43^{+0.08}_{-0.07}$
$\log N(\text{H}_2 \text{ J1})$	$16.74^{+0.17}_{-0.16}$	$18.18^{+0.08}_{-0.09}$	$18.19^{+0.13}_{-0.08}$
$\log N(\text{H}_2 \text{ J2})$	$15.79^{+0.07}_{-0.17}$	$15.81^{+0.17}_{-0.17}$	$16.04^{+0.10}_{-0.05}$
$\log N(\text{H}_2 \text{ J3})$	$15.57^{+0.12}_{-0.10}$	$15.73^{+0.19}_{-0.14}$	$15.94^{+0.09}_{-0.07}$
$\log N(\text{H}_2 \text{ J4})$	$14.24^{+0.27}_{-0.50}$	$15.10^{+0.10}_{-0.06}$	$15.13^{+0.10}_{-0.06}$
$\log N_{\text{tot}}$	$16.97^{+0.21}_{-0.14}$	$18.64^{+0.06}_{-0.08}$	$18.65^{+0.06}_{-0.07}$

absorption model. We derived $\log N(\text{H I}) = 20.73 \pm 0.01$ at the best fit value $z = 2.77916$. The Ly α profile, together with the reconstructed quasar continuum are shown in Fig. A1. We note that the Ly α emission line almost coincides with the damped Ly α absorption and is partially reconstructed from continuum fitting but that its exact shape remains uncertain at the line center where the DLA completely absorb the corresponding photons.

The fit of H₂ absorption lines was done using a two components model. The result of the fit is given in Table A1 and H₂ line profiles are shown in Fig. A2. The excitation diagrams of H₂ rotation levels for both components are shown in Fig. A3, with derived T_{01} temperatures of 102^{+161}_{-43} K and 62^{+13}_{-8} K at $z = 2.77943$ and 2.77901 , respectively.

We detected C I absorption lines in a single component arising from three fine structure levels, coinciding with the main H₂ component at $z = 2.77943$. The result of the fit is given in Table A2 and the C I absorption profiles are shown in Fig. A4.

The constrained values of the hydrogen number density and UV field in the H₂/C I-bearing medium, based on the excitation of H₂ and C I levels are shown in Fig. A5. The comparison between observed and model column densities at the best fit value of the parameters (shown by yellow star in Fig. A5) is provided in Table A3.

Metal lines are fitted using a four components model. We estimated the metallicity in this system using S II. The results of the fit are given in Table A4 and fit profiles are shown in Fig. A6.

Table A2. Fit results of C I towards J0136+0440.

z	$2.779311^{(+7)}_{(-9)}$
b , km s ⁻¹	$4.4^{+0.2}_{-0.5}$
$\log N(\text{C I})$	$14.44^{+0.10}_{-0.12}$
$\log N(\text{C I}^*)$	$14.08^{+0.05}_{-0.05}$
$\log N(\text{C I}^{**})$	$13.31^{+0.06}_{-0.06}$
$\log N_{\text{tot}}$	$14.61^{+0.08}_{-0.09}$

Table A3. Comparison of observed column densities with the in the DLA towards J0136+0440 with the modelled values calculated at the best fit value of number density and UV field from Fig. A5.

species	$\log N$	
	observed	model
C I	$14.44^{+0.10}_{-0.12}$	14.35^a
C I*	$14.08^{+0.05}_{-0.05}$	14.20^a
C I**	$13.31^{+0.06}_{-0.06}$	13.52^a
H ₂ J=0	$18.42^{+0.08}_{-0.08}$	18.43
H ₂ J=1	$18.18^{+0.13}_{-0.09}$	18.15
H ₂ J=2	$15.81^{+0.17}_{-0.17}$	15.54
H ₂ J=3 ^b		14.38
H ₂ J=4 ^b		13.28

(a) These values were obtained under then the additional assumption that the total C I column density equates the observed one.

(b) We did not use these levels to compare with observed values, since the column densities measurements for these levels are subject to a large systematic uncertainty (see text).

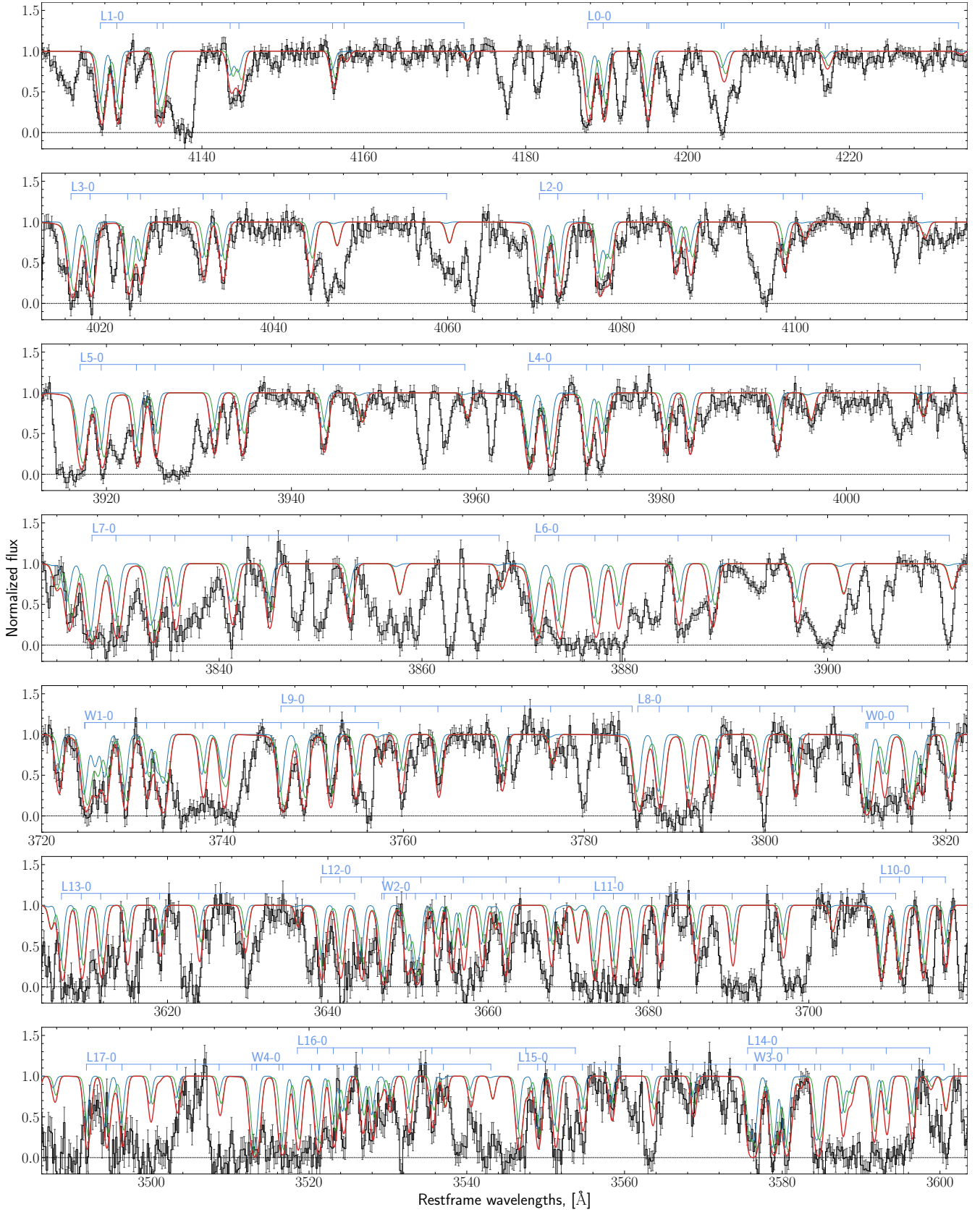


Figure A2. Fit of H_2 absorption lines in the DLA at $z = 2.77924$ towards J0136+0440.

Table A4. Fit results of metals towards J0136+0440.

comp	1	2	3	4	log N_{tot}	[X/H]	[X/SII]
z	2.778217 ⁽⁺³¹⁾ ₍₋₄₃₎	2.77922 ⁽⁺⁹⁾ ₍₋₁₄₎	2.779240 ⁽⁺¹⁵⁾ ₍₋₁₂₎	2.779960 ⁽⁺¹⁵⁾ ₍₋₂₃₎			
Δv , km s ⁻¹	-81.1	-1.7	0.0	57.1			
b , km s ⁻¹	51.0 ^{+1.8} _(-2.1)	53.4 ^{+5.2} _(-5.2)	19.1 ^{+1.6} _(-4.6)	7.4 ^{+2.3} _(-2.9)			
log N (SiII)	14.99 ^{+0.06} _(-0.09)	15.19 ^{+0.11} _(-0.16)	14.84 ^{+0.19} _(-0.36)	< 14.0	15.45 ^{+0.04} _(-0.03)	-0.80 ^{+0.04} _(-0.03)	-0.22 ^{+0.04} _(-0.05)
log N (SII)	14.76 ^{+0.05} _(-0.05)	< 14.8	15.11 ^{+0.05} _(-0.06)		15.28 ^{+0.03} _(-0.02)	-0.58 ^{+0.03} _(-0.03)	0.00 ^{+0.04} _(-0.04)
log N (FeII)	14.68 ^{+0.03} _(-0.03)	14.18 ^{+0.26} _(-0.53)	14.49 ^{+0.08} _(-0.11)	13.82 ^{+0.07} _(-0.09)	14.96 ^{+0.01} _(-0.01)	-1.28 ^{+0.02} _(-0.02)	-0.70 ^{+0.03} _(-0.04)

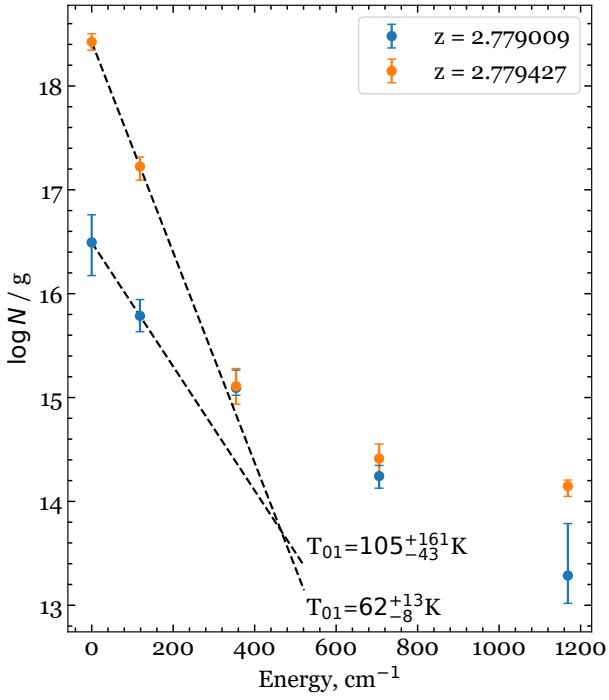


Figure A3. Excitation diagram for the two H₂ components at $z = 2.779$ towards J0136+0440.

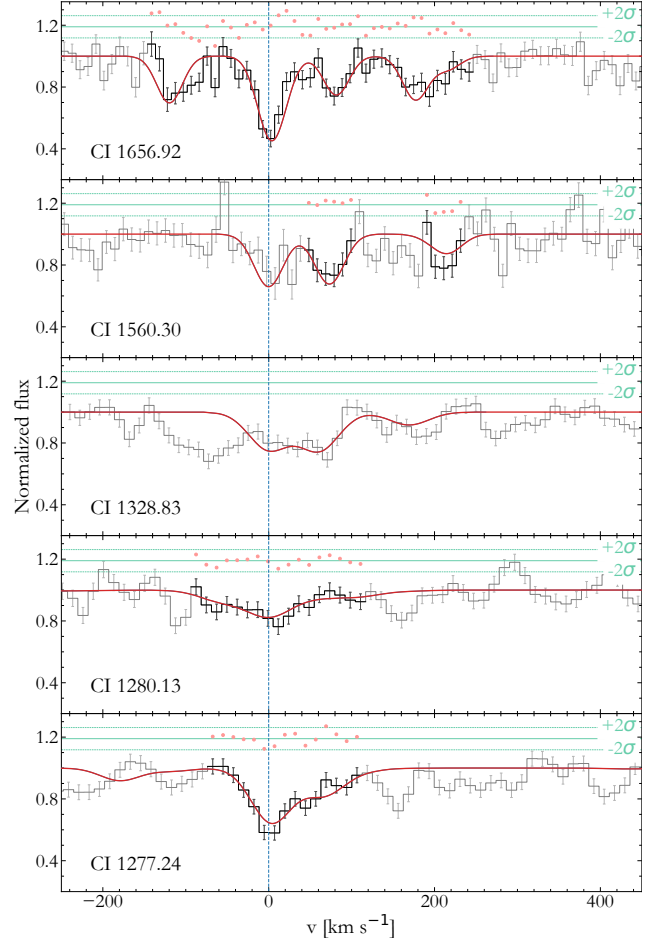


Figure A4. Fit to C I absorption lines at $z = 2.779$ towards J0136+0440.

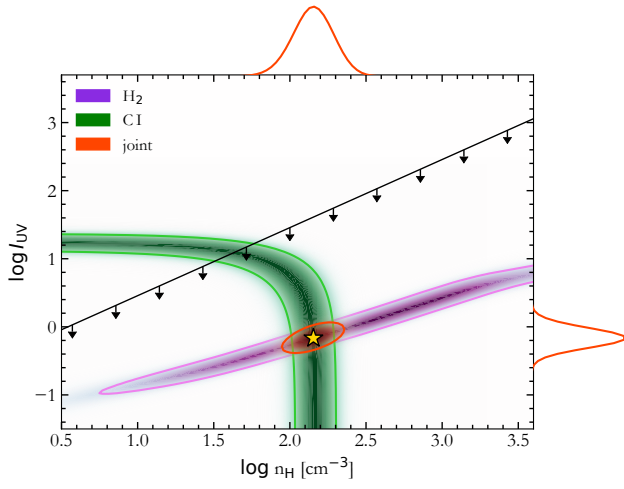


Figure A5. Constraints on the number density and UV field in the H_2 -bearing medium at $z = 2.77943$ towards J0136+0440 from the excitation of CI fine-structure and H_2 rotational levels. The colors and lines are the same as in Fig. 2

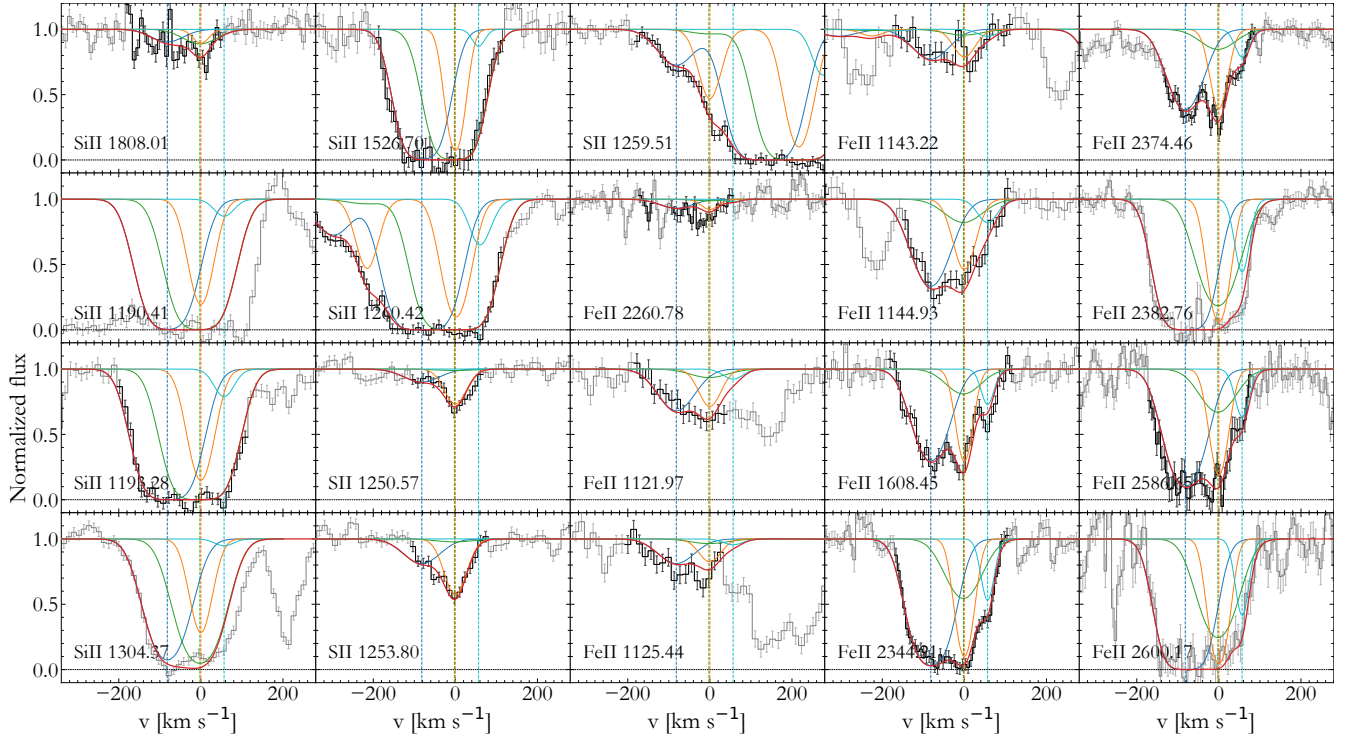


Figure A6. Fit to the metal absorption lines at $z = 2.779$ towards J0136+0440.

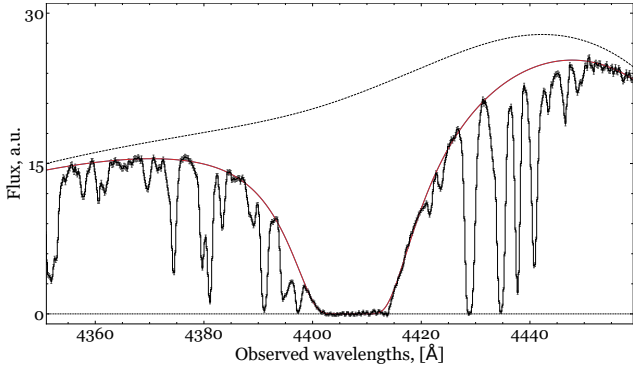


Figure A7. Fit to the damped H I Ly α absorption line at $z = 2.625$ towards J0858+1749.

A2 SDSS J085859.67+174925.32

We measured the H I column density of the DLA at $z = 2.625$ towards J0858+1749 by fitting the Ly α absorption line with a single component together with the continuum modelled using a sixth order Chebyshev polynomial. We derived $\log N(\text{H I}) = 20.40 \pm 0.01$ at the best fit value of $z = 2.62526$. The Ly α profile, together with the reconstructed quasar continuum are shown in Fig. A7.

We fitted the H₂ absorption lines towards SDSS J085859.67+174925.32 using a one component model. The result of the fit is given in Table A5 and H₂ line profiles are shown in Fig. A8. The excitation diagram of H₂ rotation levels is shown in Fig. A9 and we derived $T_{01} = 102^{+6}_{-7}$ K.

We detected C I absorption lines in three fine structure levels in a single component corresponding to H₂. The result from fitting these lines is given in Table A6 and the corresponding profiles are shown in Fig. A10.

The constrained values of the hydrogen number density and UV field in the H₂/C I-bearing medium are shown in Fig. 2 and the comparison between observed and model column densities at the best fit value (yellow star in Fig. 2) is provided in Table A7.

We fitted the metal lines with four components. At the spectral resolution achieved with X-Shooter, the low-ionisation metal profile appears to be very simple with the second component dominating the profiles and coinciding with the position of H₂ and C I. Since the S/N in this spectrum is high, we were able to fit weak Zn II, Mg I and Al III transitions. We also added Al II to the fit. However, we caution that only a single Al II line is available and in an intrinsically saturated regime. Hence, the derived column density should be considered with care. The result of the fit is given in Table A8 and fit profiles are shown in Fig. A11. We estimate the metallicity in this system using S II, which we found to be in agreement with the metallicity measured from Zn II. We noticed a relatively high depletion of iron for the measured metallicity of ~ -0.5 (see Fig. 5). This does not appear to be due to a fitting failure since the column density of Fe II is well constrained by fitting five transitions out of which three are weak.

Table A5. Fit results of H₂ towards J0858+1749.

z	$2.625248^{(+5)}_{(-4)}$
b (km s ⁻¹)	$7.9^{+0.4}_{-0.2}$
$\log N(\text{H}_2 \text{ J0})$	$19.28^{+0.02}_{-0.03}$
$\log N(\text{H}_2 \text{ J1})$	$19.51^{+0.01}_{-0.03}$
$\log N(\text{H}_2 \text{ J2})$	$17.78^{+0.22}_{-0.18}$
$\log N(\text{H}_2 \text{ J3})$	$16.99^{+0.22}_{-0.07}$
$\log N(\text{H}_2 \text{ J4})$	$15.14^{+0.07}_{-0.09}$
$\log N(\text{H}_2 \text{ J5})$	$14.53^{+0.10}_{-0.07}$
$\log N_{\text{tot}}$	$19.72^{+0.01}_{-0.02}$

Table A6. Fit results of C I towards J0858+1749.

z	$2.6252859^{(+24)}_{(-16)}$
b , km s ⁻¹	$3.8^{+0.1}_{-0.1}$
$\log N(\text{C I})$	$14.26^{+0.02}_{-0.04}$
$\log N(\text{C I}^*)$	$13.74^{+0.02}_{-0.01}$
$\log N(\text{C I}^{**})$	$12.96^{+0.02}_{-0.03}$
$\log N_{\text{tot}}$	$14.39^{+0.02}_{-0.03}$

Table A7. Comparison of observed column densities in the DLA towards J0858+1749 with the model ones, calculated at the best fit value of number density and UV field from Fig. 2.

species	$\log N$	
	observed	model
C I	$14.26^{+0.02}_{-0.04}$	14.23^a
C I*	$13.74^{+0.02}_{-0.02}$	13.83^a
C I**	$12.96^{+0.02}_{-0.03}$	12.88^a
H ₂ J0	$19.28^{+0.02}_{-0.03}$	19.26
H ₂ J1	$19.51^{+0.01}_{-0.03}$	19.44
H ₂ J2	$17.78^{+0.22}_{-0.18}$	17.41
H ₂ J3 ^b		16.11
H ₂ J4 ^b		14.23
H ₂ J5 ^b		13.76

(a) These values were obtained under then the additional assumption that the total C I column density equates the observed one.

(b) We did not use these levels to compare with observed values, since the column densities measurements for these levels are subject to a large systematic uncertainty (see text).

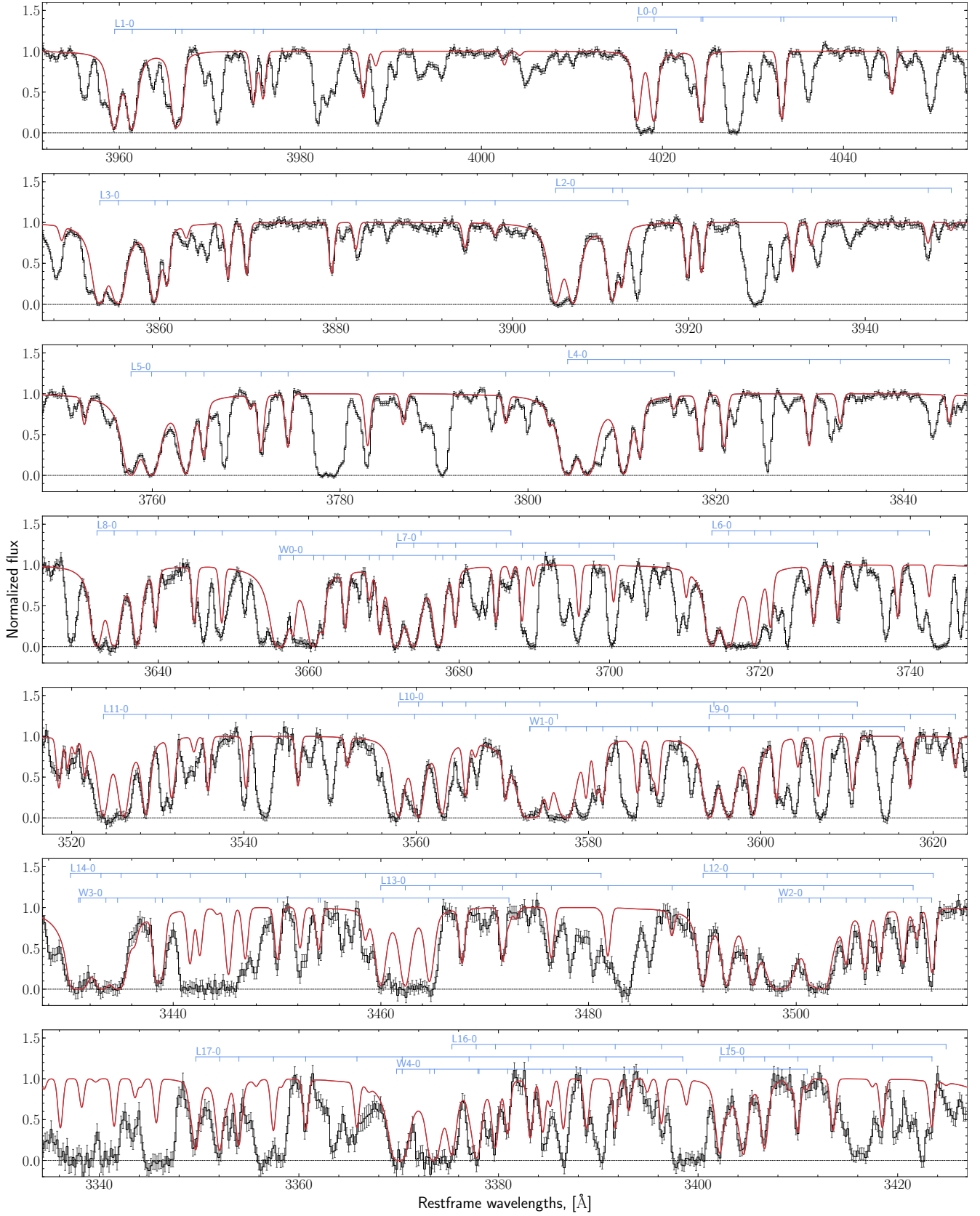
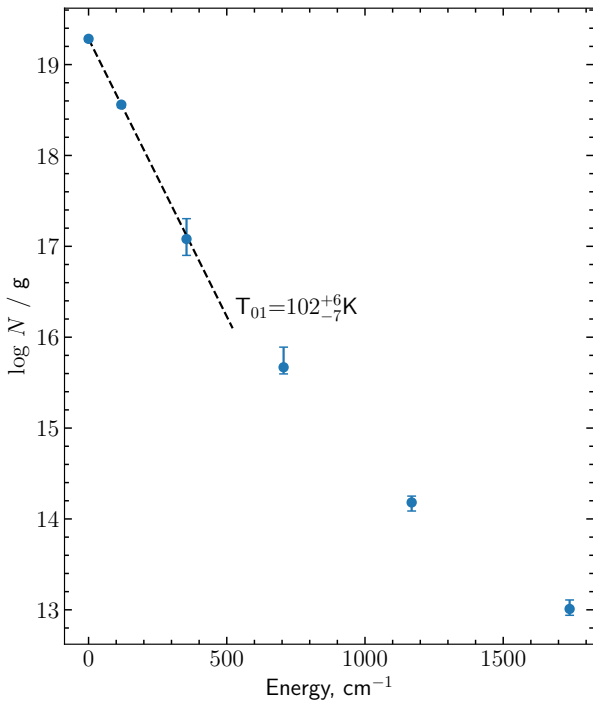
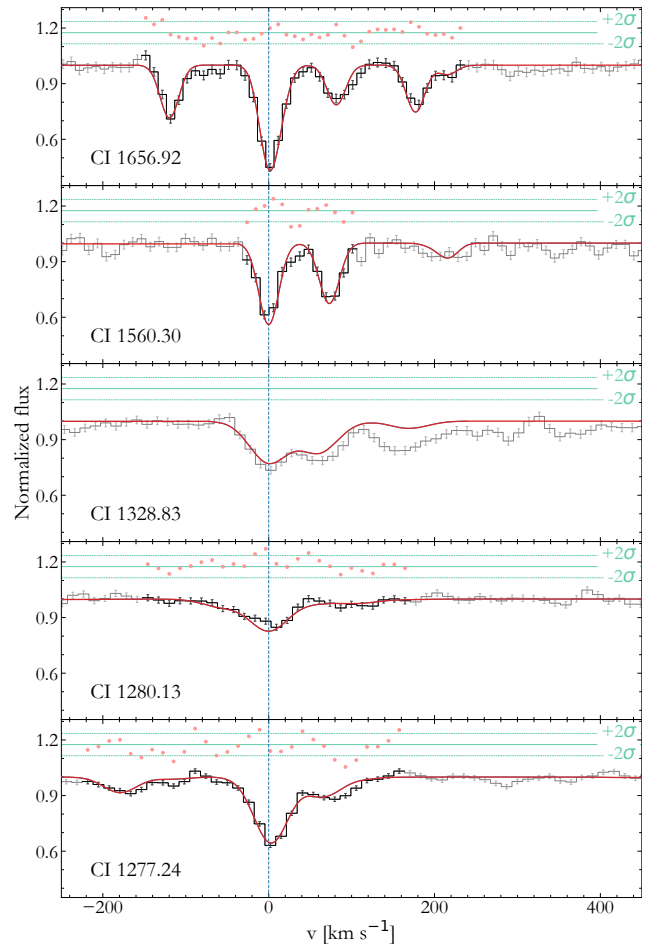


Figure A8. Fit to the H₂ absorption lines at $z = 2.625$ towards J0858+1749.

Table A8. Fit results of metals towards J0858+1749.

comp	1	2	3	4	$\log N_{\text{tot}}$	[X/H]	[X/SII]
z	$2.623389^{(+9)}_{(-15)}$	$2.6252594^{(+25)}_{(-30)}$	$2.625565^{(+28)}_{(-12)}$	$2.62596^{(+4)}_{(-13)}$			
Δv , km s $^{-1}$	-155.5	0.0	25.0	70.6			
b , km s $^{-1}$	$15.9^{+2.9}_{-1.8}$	$5.7^{+0.2}_{-0.2}$	$14.8^{+1.1}_{-4.5}$	$42.5^{+5.0}_{-8.4}$			
$\log N$ (SiII)	$13.02^{+0.06}_{-0.05}$	$15.08^{+0.03}_{-0.03}$	$13.60^{+0.06}_{-0.04}$	$13.06^{+0.08}_{-0.13}$	$15.10^{+0.02}_{-0.03}$	$-0.96^{+0.02}_{-0.04}$	$-0.41^{+0.05}_{-0.04}$
$\log N$ (FeII)	$12.55^{+0.02}_{-0.05}$	$13.70^{+0.02}_{-0.02}$	$12.23^{+0.17}_{-0.13}$	$12.26^{+0.16}_{-0.13}$	$13.75^{+0.02}_{-0.01}$	$-2.30^{+0.02}_{-0.02}$	$-1.75^{+0.03}_{-0.03}$
$\log N$ (SII)		$15.12^{+0.03}_{-0.04}$			$15.12^{+0.03}_{-0.04}$	$-0.55^{+0.03}_{-0.04}$	$0.00^{+0.05}_{-0.05}$
$\log N$ (ZnII)		$12.64^{+0.04}_{-0.02}$			$12.64^{+0.04}_{-0.02}$	$-0.47^{+0.04}_{-0.02}$	$0.08^{+0.06}_{-0.03}$
$\log N$ (MgI)		$13.30^{+0.03}_{-0.03}$			$13.30^{+0.03}_{-0.03}$	$-2.85^{+0.03}_{-0.03}$	$-2.30^{+0.05}_{-0.04}$
$\log N$ (AlII)		$13.21^{+0.10}_{-0.09}$	$12.18^{+0.05}_{-0.06}$		$13.32^{+0.07}_{-0.08}$	$-1.68^{+0.07}_{-0.08}$	$-1.13^{+0.08}_{-0.09}$
$\log N$ (AlIII)			$12.46^{+0.02}_{-0.04}$		$12.46^{+0.02}_{-0.04}$	$-2.54^{+0.02}_{-0.04}$	$-1.99^{+0.04}_{-0.05}$

**Figure A9.** Excitation diagram of H₂ at $z = 2.625$ towards J0858+1749.**Figure A10.** Fit to the CI absorption lines at $z = 2.625$ towards J0858+1749.

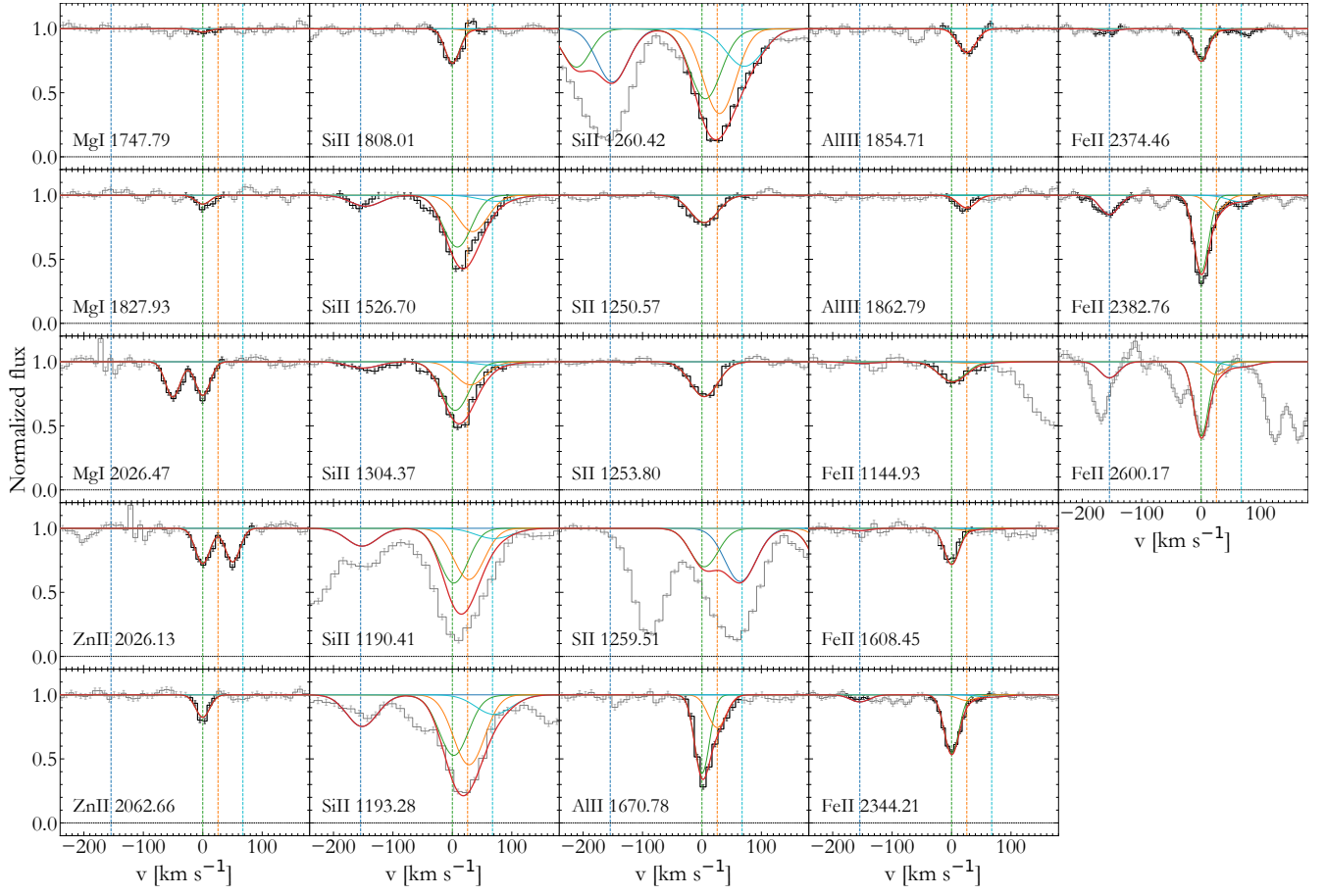


Figure A11. Fit to the metal absorption lines at $z = 2.625$ towards J0858+1749.

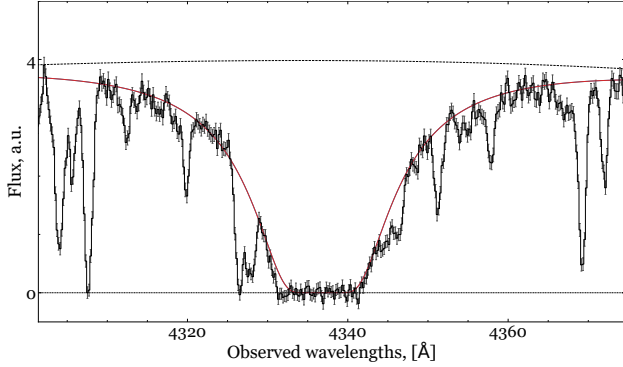


Figure A12. Fit to the H I Ly α absorption line at $z = 2.567$ towards J0906+0548.

A3 SDSS J090609.46+054818.72

We measured the H I column density of the DLA at $z = 2.567$ towards J0906+0548 by fitting the Ly α absorption line with a single component together with the continuum modelled using a sixth order Chebyshev polynomial. The derived column density, $\log N(\text{H I}) = 20.13 \pm 0.01$ at the best fit value $z = 2.56742$, indicates that this system formally belong to the class of sub-DLAs. The Ly α profile, together with the estimated quasar continuum are shown in Fig. A12.

We fit H₂ absorption lines in J0906+0548 using one component model. The result of the fit is given in Table A9 and the profiles of H₂ lines are shown in Fig. A13. The excitation diagrams of H₂ rotation levels for both components is shown in Fig. A14. We derived the T_{01} temperature to be 172^{+221}_{-55} K and 116^{+26}_{-4} K for the H₂ components at $z = 2.56698$ and 2.56918 , respectively.

We detected C I absorption lines from its three fine structure levels only at the location of the reddest and strongest H₂ component that dominates the profile. We therefore fitted C I lines using a one-component model. Unfortunately, C I lines from the 1560 Å multiplet are located at the noisy blue side of the VIS exposure for both X-shooter exposures and were not considered to constrain the fit. The result of the fit is given in Table A10 and the profiles of C I absorption lines are shown in Fig. A15.

The constrained values of the hydrogen number density and UV field in the H₂/C I-bearing medium are shown in Fig. A16 and the comparison between observed and model column densities at the best fit value (yellow star in Fig. A16) is provided in Table A11.

Eight components were used to model the metal line profile. The fifth and seventh components correspond to the position of H₂ components. Since the H I column density is relatively small we detected only a few low ionization metals and did not detect Zn II, Cr II, Ni II. We estimated the metallicity in this system using S II. The result of the fit is given in Table A12 and fit profiles are shown in Fig. A17.

Table A9. Fit results of H₂ towards J0906+0548.

comp	1	2	$\log N_{\text{tot}}$
z	$2.566980^{(+9)}_{(-4)}$	$2.5691809^{(+11)}_{(-73)}$	
Δv , km s ⁻¹	0.0	184.5	
b , km s ⁻¹	$7.5^{+0.3}_{-0.3}$	$6.8^{+0.1}_{-0.1}$	
$\log N(\text{H}_2 \text{ J0})$	$15.91^{+0.13}_{-0.15}$	$18.38^{+0.01}_{-0.07}$	$18.38^{+0.01}_{-0.07}$
$\log N(\text{H}_2 \text{ J1})$	$16.43^{+0.09}_{-0.07}$	$18.70^{+0.05}_{-0.01}$	$18.70^{+0.05}_{-0.01}$
$\log N(\text{H}_2 \text{ J2})$	$15.69^{+0.13}_{-0.10}$	$16.87^{+0.01}_{-0.01}$	$16.89^{+0.02}_{-0.01}$
$\log N(\text{H}_2 \text{ J3})$	$15.95^{+0.12}_{-0.09}$	$16.15^{+0.07}_{-0.07}$	$16.39^{+0.04}_{-0.08}$
$\log N(\text{H}_2 \text{ J4})$	$14.74^{+0.05}_{-0.04}$	$15.20^{+0.05}_{-0.04}$	$15.32^{+0.05}_{-0.03}$
$\log N(\text{H}_2 \text{ J5})$	$14.34^{+0.10}_{-0.04}$	$15.00^{+0.03}_{-0.03}$	$15.10^{+0.03}_{-0.03}$
$\log N_{\text{tot}}$	$16.70^{+0.11}_{-0.06}$	$18.87^{+0.02}_{-0.02}$	$18.88^{+0.02}_{-0.02}$

Table A10. Fit results of C I towards J0906+0548.

z	$2.569225^{(+6)}_{(-7)}$
b , km s ⁻¹	$3.8^{+0.6}_{-0.5}$
$\log N(\text{C I})$	$13.50^{+0.08}_{-0.06}$
$\log N(\text{C I}^*)$	$13.61^{+0.03}_{-0.03}$
$\log N(\text{C I}^{**})$	$12.89^{+0.07}_{-0.08}$
$\log N_{\text{tot}}$	$13.90^{+0.04}_{-0.03}$

Table A11. Comparison of observed column densities in the DLA towards J0906+0548 with the model ones, calculated at the best fit value of number density and UV field from Fig. A16.

species	$\log N$	
	observed	model
C I	$13.50^{+0.08}_{-0.06}$	13.55^a
C I*	$13.61^{+0.03}_{-0.03}$	13.54^a
C I**	$12.89^{+0.07}_{-0.08}$	13.00^a
H ₂ J0	$18.38^{+0.01}_{-0.07}$	18.45
H ₂ J1	$18.70^{+0.05}_{-0.01}$	18.68
H ₂ J2	$16.87^{+0.01}_{-0.01}$	16.92
H ₂ J3 ^b		15.94
H ₂ J4 ^b		14.29
H ₂ J5 ^b		13.87

(a) These values were obtained under the additional assumption that the total C I column density equates the observed one.

(b) We did not use these levels to compare with observed values, since the column densities measurements for these levels are subject to a large systematic uncertainty (see text).

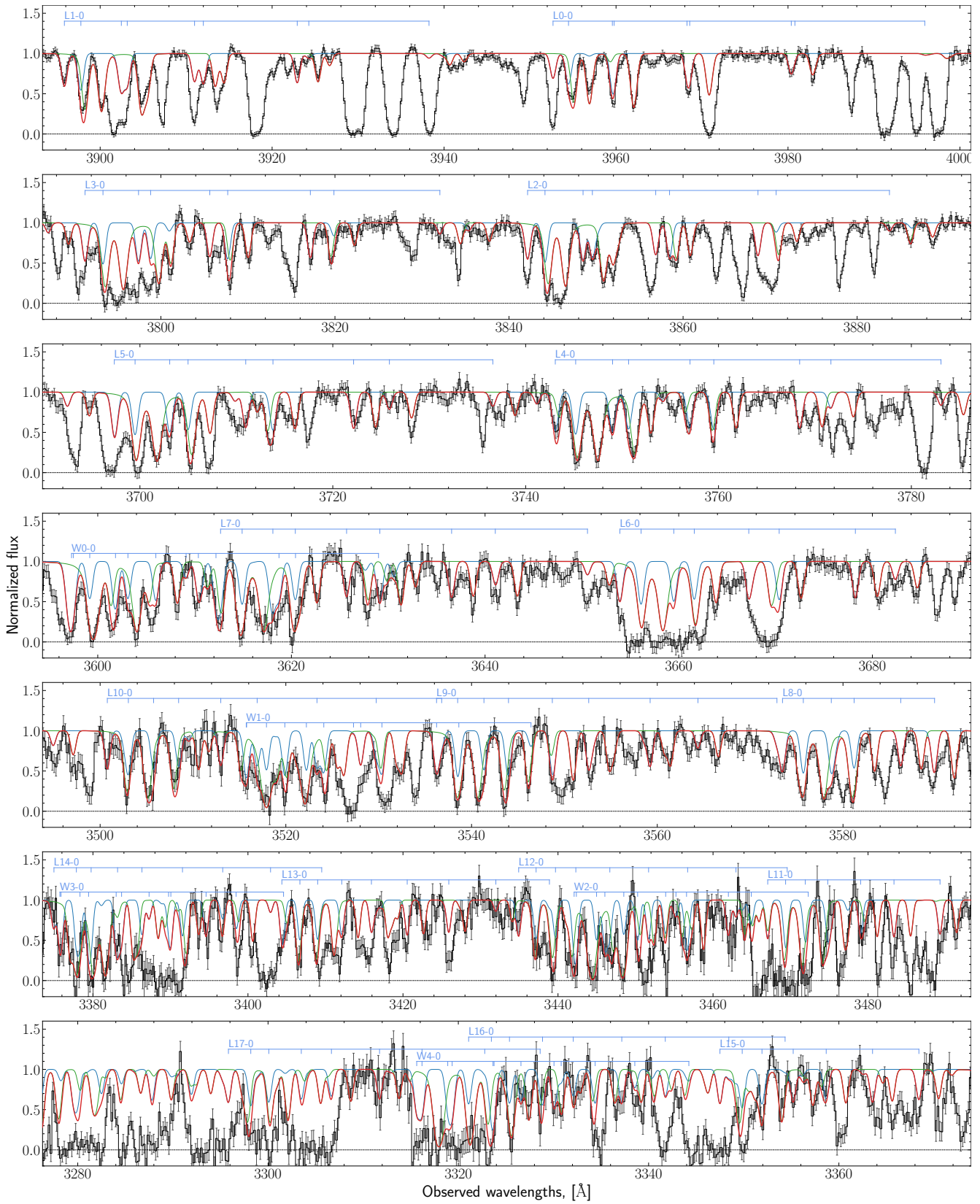
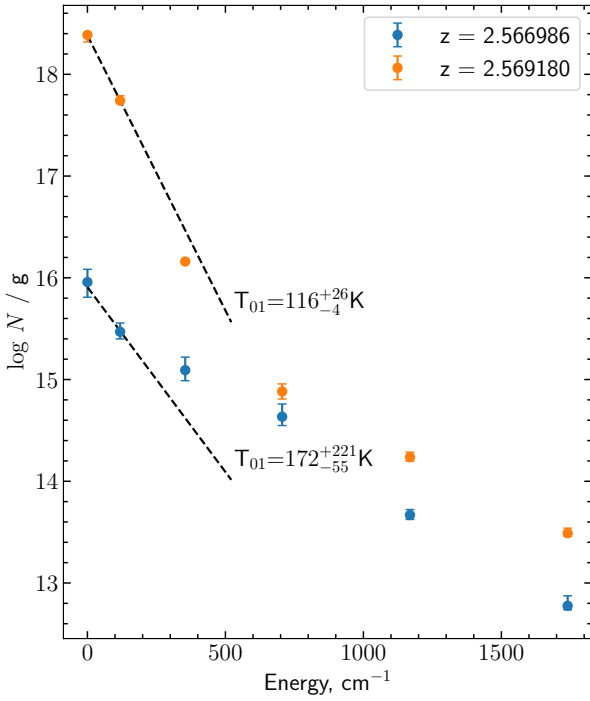
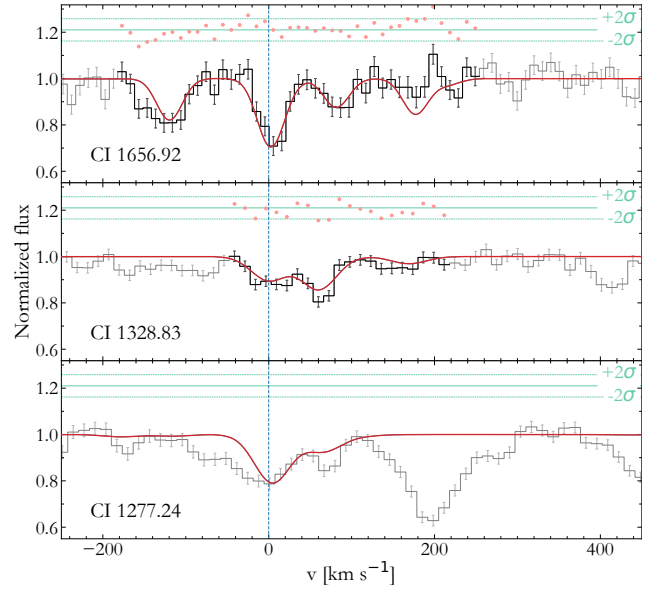


Figure A13. Fit to H₂ absorption lines at $z = 2.567$ towards J0906+0548.

Table A12. Fit results of metals towards J0906+0548.

comp	z	Δv , km s ⁻¹	b, km s ⁻¹	log N(SiII)	log N(FeII)	log N(SII)
1	2.563318(⁺⁵ ₋₂₄)	-500.3	10.6 ^{+5.7} _{-4.7}	13.20 ^{+0.05} _{-0.05}	12.81 ^{+0.04} _{-0.04}	
2	2.56625(⁺³ ₋₃)	-254.2	12.7 ^{+6.2} _{-6.8}	13.01 ^{+0.10} _{-0.06}	12.64 ^{+0.08} _{-0.08}	
3	2.566892(⁺¹⁶ ₋₁₆)	-199.2	7.6 ^{+2.5} _{-2.7}	14.21 ^{+0.16} _{-0.13}	13.79 ^{+0.09} _{-0.08}	14.40 ^{+0.30} _{-0.49}
4	2.56701(⁺⁸ ₋₃)	-187.3	25.1 ^{+5.9} _{-3.7}	14.22 ^{+0.06} _{-0.10}	13.60 ^{+0.07} _{-0.13}	
5	2.567609(⁺¹³ ₋₁₉)	-138.2	10.6 ^{+1.0} _{-1.1}	14.55 ^{+0.07} _{-0.05}	13.64 ^{+0.03} _{-0.03}	15.08 ^{+0.04} _{-0.09}
6	2.568677(⁺¹⁰ ₋₁₁)	-48.8	7.8 ^{+1.4} _{-3.1}	13.28 ^{+0.03} _{-0.03}	12.84 ^{+0.03} _{-0.04}	
7	2.569257(⁺¹⁴ ₋₈)	0.0	2.8 ^{+1.2} _{-0.2}	13.80 ^{+0.26} _{-0.19}	12.93 ^{+0.10} _{-0.08}	
8	2.570366(⁺³ ₋₅)	92.9	23.4 ^{+0.6} _{-0.4}	14.18 ^{+0.01} _{-0.01}	13.18 ^{+0.02} _{-0.02}	
log N _{tot}				14.99 ^{+0.04} _{-0.05}	14.24 ^{+0.03} _{-0.03}	15.14 ^{+0.05} _{-0.05}
[X/H]				-0.70 ^{+0.04} _{-0.05}	-1.44 ^{+0.03} _{-0.03}	-0.16 ^{+0.03} _{-0.08}
[X/SII]				-0.54 ^{+0.08} _{-0.07}	-1.28 ^{+0.08} _{-0.06}	0.00 ^{+0.09} _{-0.09}

**Figure A14.** Excitation diagram for the two H₂ components at $z = 2.567$ towards J0906+0548.**Figure A15.** Fit to the C I absorption lines at $z = 2.567$ towards J0906+0548.

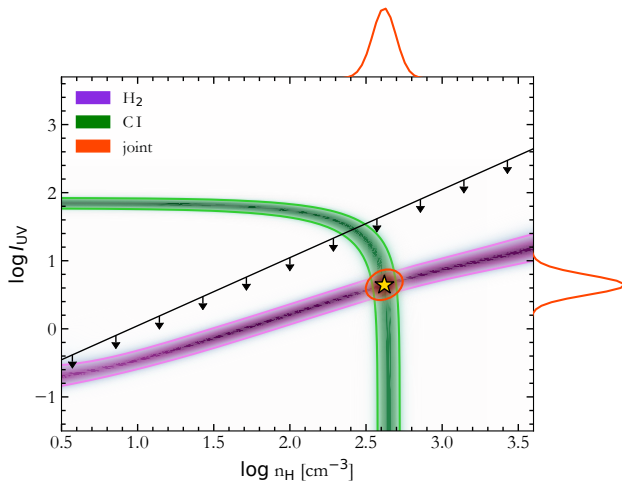


Figure A16. Constraints on the number density and UV field in the H₂-bearing medium at $z = 2.569181$ towards J0906+0548 from the excitation of CI fine-structure and H₂ rotational levels. The colors and lines are the same as in Fig. 2

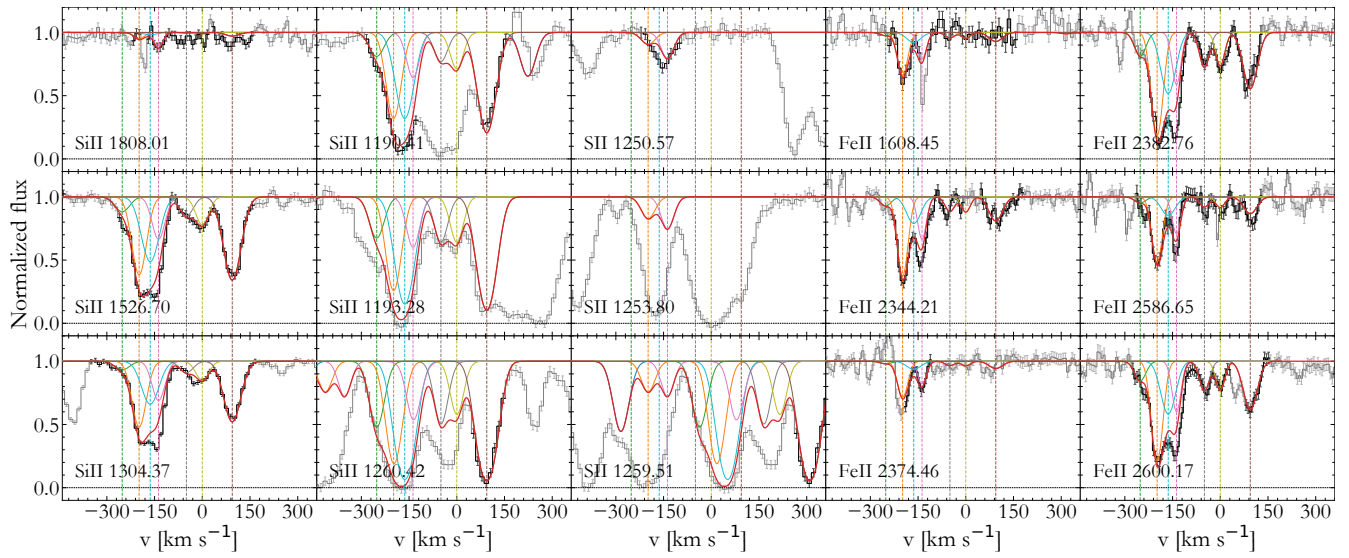


Figure A17. Fit to the metal absorption lines at $z = 2.567$ towards J0906+0548.

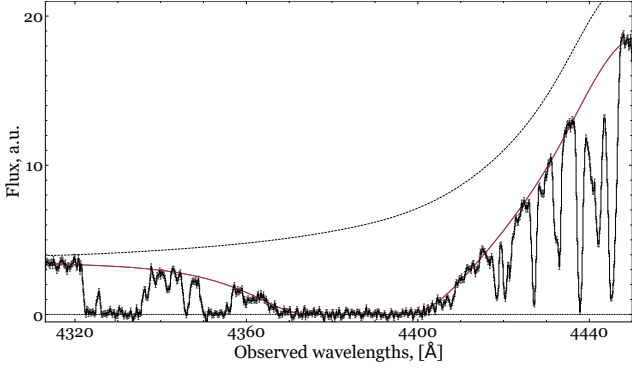


Figure A18. Fit to the damped H I Ly α absorption line at $z = 2.607$ towards J0946+1216.

A4 SDSS J094649.47+121628.56

We measured the H I column density of the DLA at $z = 2.607$ towards J0946+1216 by fitting the Ly α absorption line with a single component together with the continuum modelled using a seventh order Chebyshev polynomial. We derived $\log N(\text{H I}) = 21.15 \pm 0.02$ at the best fit value of $z = 2.60771$. The Ly α profile, together with the reconstructed quasar continuum are shown in Fig. A18.

The fit of H₂ absorption lines was done using a two components model. The result of the fit is given in Table A13 and H₂ line profiles are shown in Fig. A19. The large reported Doppler parameters for the red component probably indicate to unresolved subcomponents in H₂ lines. The excitation diagrams of H₂ rotation levels for both components are shown in Fig. A20, with derived T_{01} temperatures of 131^{+10}_{-14} K and > 90 K (1σ lower limit) for the component at $z = 2.60641$ and 2.60708 , respectively.

We detected C I absorption lines in two components arising from three fine structure levels, coinciding with the H₂ components. The result of the fit is given in Table A14 and the C I absorption profiles are shown in Fig. A21.

Since we measured only the lower limit on the temperature in the minor H₂/C I-bearing component at $z = 2.60708$, we constrained values of the hydrogen number density and UV field based on excitation of H₂ and C I levels only in the main H₂/C I-bearing component at $z = 2.60641$ (shown in Fig. A22). The comparison between observed and model column densities at the best fit value of the parameters (shown by yellow star in Fig. A22) is provided in Table A15.

Metal lines are fitted using a six components model. We estimated the metallicity in this system using S II. The results of the fit are given in Table A16 and fit profiles are shown in Fig. A23.

Table A13. Fit results of H₂ towards J0946+1216.

comp	1	2	$\log N_{\text{tot}}$
z	$2.606406^{(+30)}_{(-8)}$	$2.607083^{(+16)}_{(-5)}$	
Δv , km s ⁻¹	0.0	57.2	
b , km s ⁻¹	$9.8^{+0.8}_{-0.3}$	$17.6^{+1.6}_{-0.7}$	
$\log N(\text{H}_2 \text{ J0})$	$19.42^{+0.04}_{-0.02}$	$16.34^{+0.44}_{-0.21}$	$19.42^{+0.04}_{-0.02}$
$\log N(\text{H}_2 \text{ J1})$	$19.81^{+0.02}_{-0.02}$	$17.10^{+0.37}_{-0.08}$	$19.81^{+0.02}_{-0.02}$
$\log N(\text{H}_2 \text{ J2})$	$18.10^{+0.12}_{-0.17}$	$16.33^{+0.08}_{-0.13}$	$18.11^{+0.11}_{-0.17}$
$\log N(\text{H}_2 \text{ J3})$	$16.53^{+0.13}_{-0.15}$	$15.74^{+0.07}_{-0.05}$	$16.58^{+0.12}_{-0.11}$
$\log N(\text{H}_2 \text{ J4})$	$15.19^{+0.09}_{-0.04}$	$14.50^{+0.11}_{-0.13}$	$15.29^{+0.05}_{-0.05}$
$\log N(\text{H}_2 \text{ J5})$	$14.70^{+0.09}_{-0.10}$	$14.46^{+0.12}_{-0.08}$	$14.92^{+0.04}_{-0.04}$
$\log N_{\text{tot}}$	$19.96^{+0.01}_{-0.02}$	$17.26^{+0.31}_{-0.08}$	$19.97^{+0.01}_{-0.02}$

Table A14. Fit results of C I towards J0946+1216.

comp	1	2	$\log N_{\text{tot}}$
z	$2.606540^{(+5)}_{(-6)}$	$2.607271^{(+21)}_{(-15)}$	
Δv , km s ⁻¹	0.0	63.0	
b , km s ⁻¹	$4.6^{+0.3}_{-0.3}$	$12.6^{+3.1}_{-1.8}$	
$\log N(\text{C I})$	$14.10^{+0.05}_{-0.05}$	$13.22^{+0.05}_{-0.06}$	$14.15^{+0.04}_{-0.04}$
$\log N(\text{C I}^*)$	$13.89^{+0.03}_{-0.04}$	$13.35^{+0.03}_{-0.03}$	$14.10^{+0.02}_{-0.03}$
$\log N(\text{C I}^{**})$	$13.28^{+0.05}_{-0.04}$	$12.83^{+0.10}_{-0.18}$	$13.41^{+0.05}_{-0.05}$
$\log N_{\text{tot}}$	$14.33^{+0.05}_{-0.02}$	$13.64^{+0.03}_{-0.02}$	$14.42^{+0.04}_{-0.02}$

Table A15. Comparison of observed column densities in the component at $z = 2.60641$ towards J0946+1216 with the model ones, calculated at the best fit value of number density and UV field from Fig. A22.

species	$\log N$	
	observed	model
C I	$14.10^{+0.05}_{-0.05}$	14.09^a
C I*	$13.89^{+0.03}_{-0.04}$	13.92^a
C I**	$13.28^{+0.05}_{-0.04}$	13.25^a
H ₂ J0	$19.42^{+0.04}_{-0.02}$	19.53
H ₂ J1	$19.81^{+0.02}_{-0.02}$	19.72
H ₂ J2	$18.10^{+0.12}_{-0.17}$	17.87
H ₂ J3 ^b		16.29
H ₂ J4 ^b		15.19
H ₂ J5 ^b		14.70

(a) These values were obtained under the additional assumption that the total C I column density equates the observed one.

(b) We did not use these levels to compare with observed values, since the column densities measurements for these levels are subject to a large systematic uncertainty (see text).

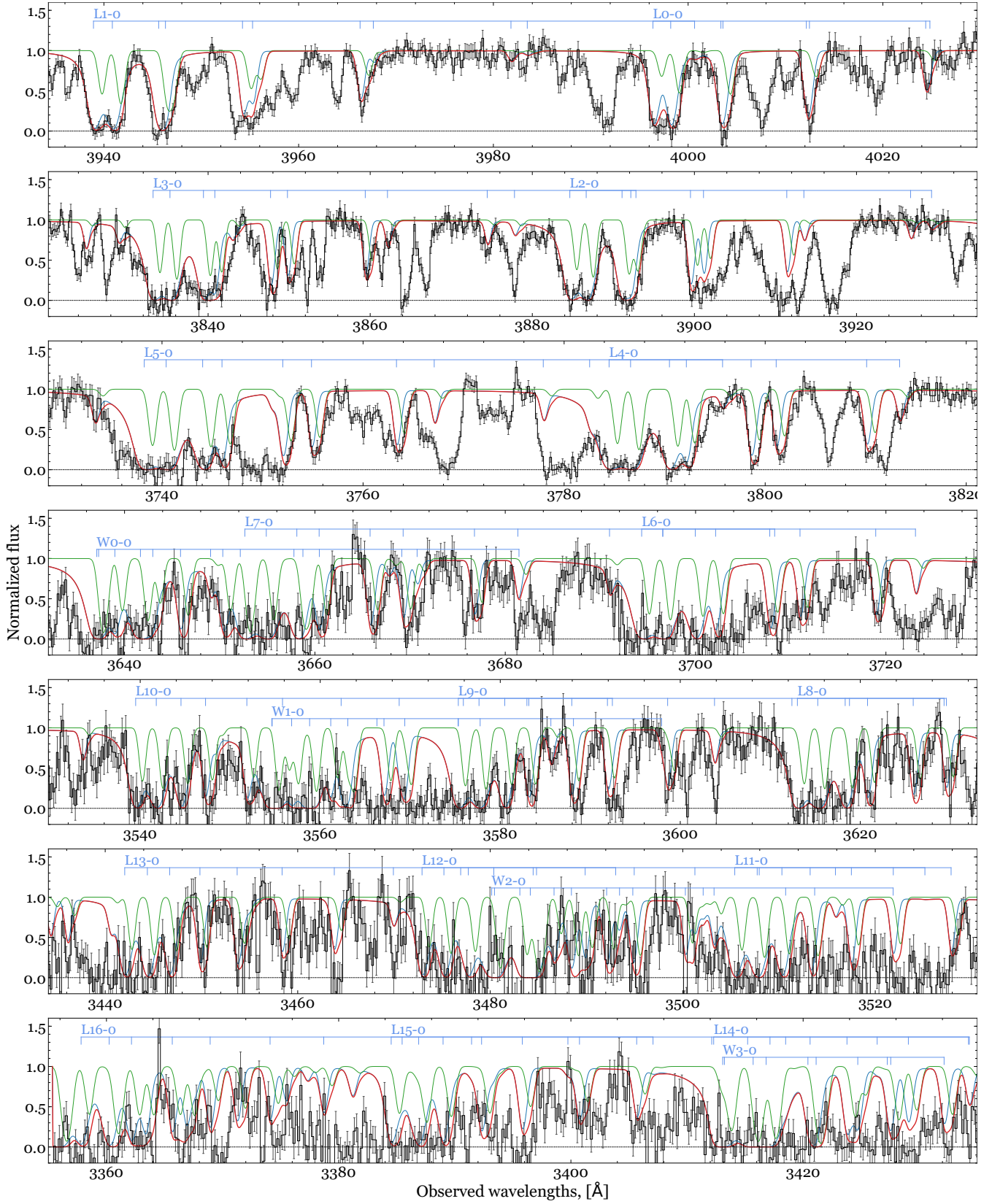


Figure A19. Fit to H₂ absorption lines at $z = 2.607$ towards J0946+1216.

Table A16. Fit results of metals towards J0946+1216.

comp	z	Δv , km s ⁻¹	b , km s ⁻¹	$\log N(\text{SiII})$	$\log N(\text{FeII})$	$\log N(\text{SII})$	$\log N(\text{NiII})$	$\log N(\text{CrII})$	$\log N(\text{ZnII})$
1	2.605717 ⁽⁺⁹⁾ ₍₋₃₎	-74.5	8.7 ^{+0.8} _{-0.6}	13.74 ^{+0.06} _{-0.06}	13.36 ^{+0.03} _{-0.03}				
2	2.606617 ⁽⁺⁹⁾ ₍₋₁₁₎	0.0	21.7 ^{+0.6} _{-0.7}	15.53 ^{+0.03} _{-0.03}	14.99 ^{+0.03} _{-0.02}	15.35 ^{+0.02} _{-0.02}	13.81 ^{+0.02} _{-0.03}	13.33 ^{+0.03} _{-0.02}	12.96 ^{+0.04} _{-0.02}
3	2.607342 ⁽⁺¹⁸⁾ ₍₋₁₅₎	58.2	17.8 ^{+3.3} _{-2.8}	15.47 ^{+0.03} _{-0.05}	14.76 ^{+0.03} _{-0.04}	15.37 ^{+0.02} _{-0.02}	13.58 ^{+0.06} _{-0.07}	13.14 ^{+0.05} _{-0.07}	12.97 ^{+0.03} _{-0.05}
4	2.60812 ⁽⁺⁴⁾ ₍₋₄₎	119.9	35.9 ^{+4.8} _{-3.8}	15.26 ^{+0.06} _{-0.07}	14.66 ^{+0.04} _{-0.04}	15.14 ^{+0.05} _{-0.04}	13.64 ^{+0.08} _{-0.14}	12.95 ^{+0.09} _{-0.11}	12.82 ^{+0.04} _{-0.09}
5	2.609050 ⁽⁺¹⁴⁾ ₍₋₂₀₎	212.0	11.5 ^{+1.4} _{-2.2}	14.75 ^{+0.10} _{-0.10}	14.10 ^{+0.04} _{-0.04}	14.01 ^{+0.14} _{-0.14}	13.21 ^{+0.14} _{-0.14}	12.69 ^{+0.10} _{-0.14}	12.31 ^{+0.03} _{-0.03}
6	2.609836 ⁽⁺⁹⁾ ₍₋₁₀₎	269.7	39.2 ^{+0.5} _{-0.6}	15.44 ^{+0.02} _{-0.02}	14.94 ^{+0.01} _{-0.01}	15.09 ^{+0.16} _{-0.01}	13.82 ^{+0.03} _{-0.04}	13.21 ^{+0.04} _{-0.05}	12.82 ^{+0.03} _{-0.04}
$\log N_{\text{tot}}$				16.06 ^{+0.01} _{-0.01}	15.48 ^{+0.01} _{-0.01}	15.86 ^{+0.01} _{-0.01}	14.36 ^{+0.02} _{-0.02}	13.81 ^{+0.02} _{-0.02}	13.52 ^{+0.02} _{-0.01}
[X/H]				-0.65 ^{+0.02} _{-0.02}	-1.22 ^{+0.02} _{-0.02}	-0.46 ^{+0.02} _{-0.02}	-1.06 ^{+0.03} _{-0.03}	-1.03 ^{+0.03} _{-0.03}	-0.24 ^{+0.03} _{-0.02}
[X/SII]				-0.19 ^{+0.02} _{-0.02}	-0.76 ^{+0.01} _{-0.02}	0.00 ^{+0.01} _{-0.02}	-0.60 ^{+0.02} _{-0.03}	-0.57 ^{+0.02} _{-0.03}	0.22 ^{+0.02} _{-0.02}

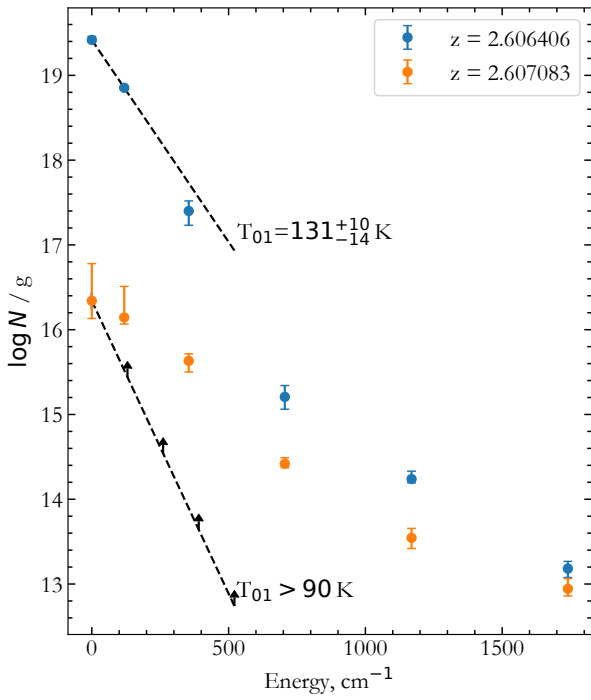


Figure A20. Excitation diagram for the two H₂ components at $z = 2.607$ towards J0946+1216.

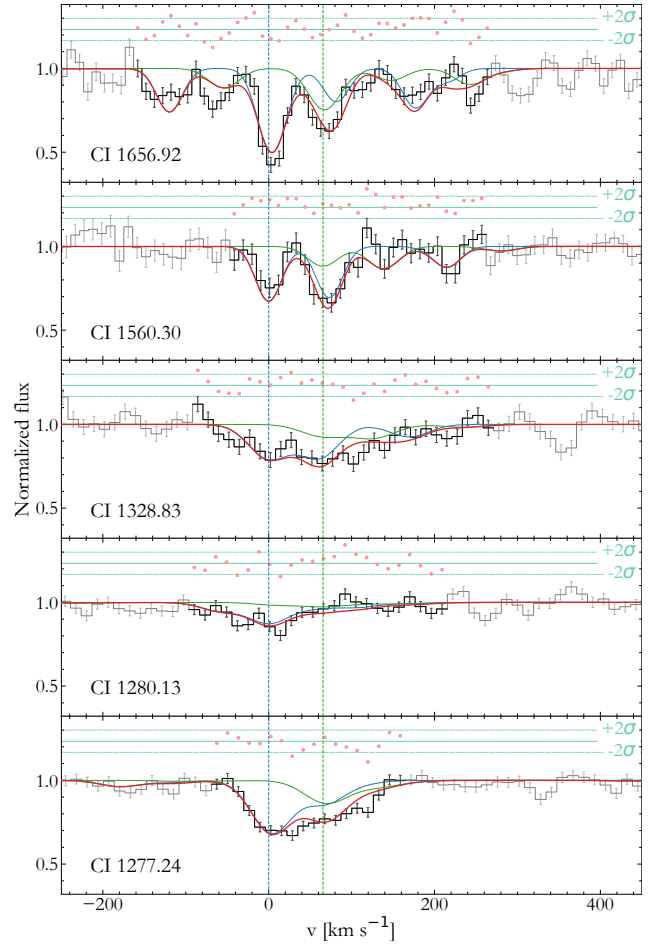


Figure A21. Fit to the C I absorption lines at $z = 2.607$ towards J0946+1216.

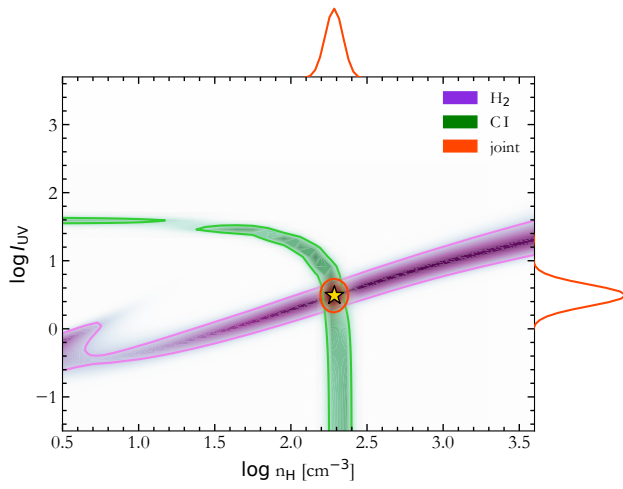


Figure A22. Constraints on number density and UV field in the H₂-bearing medium at $z = 2.60641$ towards J0946+1216 from the excitation of C I fine-structure and H₂ rotational levels. The colors and lines are the same as in Fig. 2.

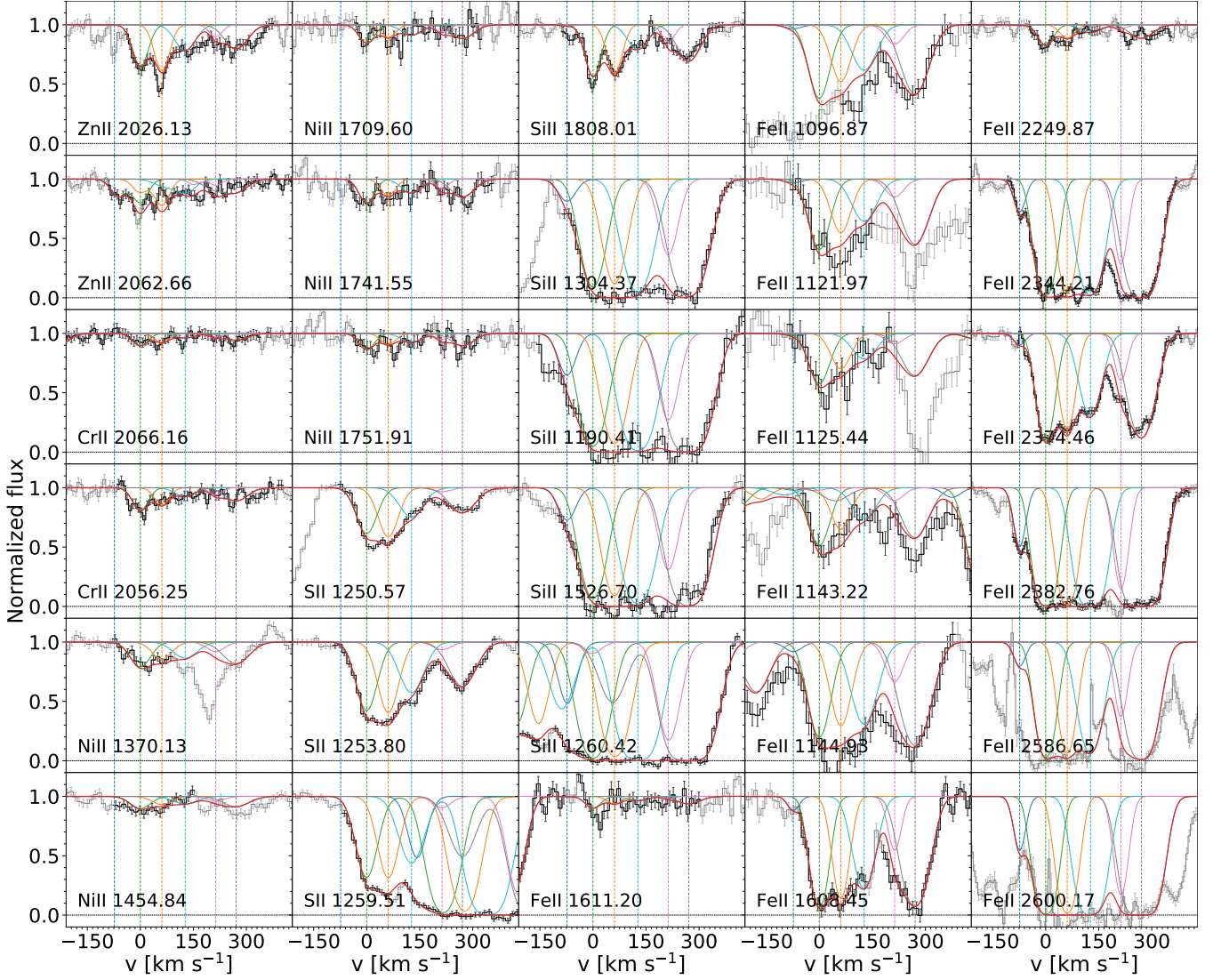


Figure A23. Fit to the metal absorption lines at $z = 2.607$ towards J0946+1216.

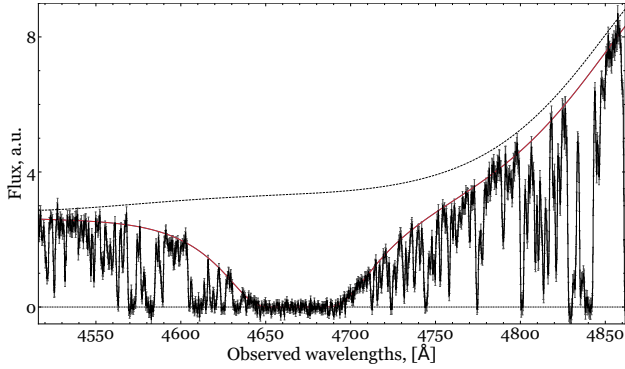


Figure A24. Fit to the damped H I Ly α absorption line at $z = 2.840$ towards J1146+0743.

A5 SDSS J114638.95+074311.28

We measured the H I column density of the DLA at $z = 2.840$ towards J1146+0743 by fitting the Ly α absorption line. We fitted together the continuum using seventh order Chebyshev polynomial in the region of Ly α line with a one-component absorption model. We derived $\log N(\text{H I}) = 21.54 \pm 0.01$ at the best fit value $z = 2.84059$. The Ly α profile, together with the reconstructed quasar continuum are shown in Fig. A24.

The fit of H₂ absorption lines was done using a two components model. The result of the fit is given in Table A17 and H₂ line profiles are shown in Fig. A25. The excitation diagrams of H₂ rotation levels for both components are shown in Fig. A26, with derived T_{01} temperatures of 91^{+3}_{-2} K and 57^{+25}_{-16} K at $z = 2.83946$ and 2.84163 , respectively.

We detected C I absorption lines in two components arising from three fine structure levels, coinciding with the H₂ components of DLA. The red component of C I 1656.92 Å line coincides with sky line, therefore we excluded corresponding pixels from the fit. The result of the fit is given in Table A18 and the C I absorption profiles are shown in Fig. A27.

The constrained values of the hydrogen number density and UV field in the H₂/C I-bearing medium, based on the excitation of H₂ and C I levels are shown in Fig. A28 and A29 for component at $z = 2.83946$ and 2.84163 , respectively. The comparison between observed and model column densities at the best fit value of the parameters (shown by yellow star in Fig. A5) is provided in Tables A19 and A20.

Metal lines are fitted using a five components model. The two strongest components seen in metal profiles coincide with the two components seen in H₂ absorption lines. The results of the fit are given in Table A21 and fit profiles are shown in Fig. A30.

Table A17. Fit results of H₂ towards J1146+0743.

comp	1	2	$\log N_{\text{tot}}$
z	$2.839459^{(+19)}_{(-8)}$	$2.841629^{(+10)}_{(-24)}$	
Δv , km s ⁻¹	0	166.7	
b , km s ⁻¹	$7.6^{+0.1}_{-0.4}$	$11.4^{+0.5}_{-0.7}$	
$\log N(\text{H}_2 \text{ J0})$	$18.38^{+0.01}_{-0.01}$	$17.75^{+0.02}_{-0.05}$	$18.47^{+0.01}_{-0.01}$
$\log N(\text{H}_2 \text{ J1})$	$18.52^{+0.01}_{-0.01}$	$17.40^{+0.28}_{-0.37}$	$18.54^{+0.04}_{-0.11}$
$\log N(\text{H}_2 \text{ J2})$	$16.57^{+0.09}_{-0.17}$	$16.06^{+0.11}_{-0.10}$	$16.67^{+0.11}_{-0.10}$
$\log N(\text{H}_2 \text{ J3})$	$15.97^{+0.09}_{-0.05}$	$16.05^{+0.09}_{-0.05}$	$16.34^{+0.04}_{-0.06}$
$\log N(\text{H}_2 \text{ J4})$	$14.70^{+0.05}_{-0.10}$	$15.14^{+0.07}_{-0.05}$	$15.28^{+0.05}_{-0.06}$
$\log N(\text{H}_2 \text{ J5})$	$13.68^{+0.34}_{-2.18}$	$14.62^{+0.07}_{-0.08}$	$14.66^{+0.06}_{-0.10}$
$\log N_{\text{tot}}$	$18.76^{+0.01}_{-0.01}$	$17.94^{+0.11}_{-0.13}$	$18.82^{+0.03}_{-0.02}$

Table A18. Fit results of C I towards J1146+0743.

comp	1	2	$\log N_{\text{tot}}$
z	$2.839015^{(+26)}_{(-18)}$	$2.841553^{(+3)}_{(-12)}$	
Δv , km s ⁻¹	0.0	196.4	
b , km s ⁻¹	$16.8^{+2.6}_{-4.0}$	$2.7^{+14.9}_{-1.9}$	
$\log N(\text{C I})$	$13.28^{+0.05}_{-0.04}$	$13.17^{+0.10}_{-0.11}$	$13.53^{+0.05}_{-0.05}$
$\log N(\text{C I}^*)$	$13.10^{+0.09}_{-0.10}$	$13.07^{+0.05}_{-0.08}$	$13.56^{+0.07}_{-0.04}$
$\log N(\text{C I}^{**})$	$12.93^{+0.12}_{-0.18}$	$12.85^{+0.12}_{-0.11}$	$13.23^{+0.04}_{-0.16}$
$\log N_{\text{tot}}$	$13.59^{+0.13}_{-0.04}$	$13.51^{+0.05}_{-0.06}$	$13.85^{+0.03}_{-0.03}$

Table A19. Comparison of observed column densities in the component at $z = 2.83946$ of DLA towards J1146+0743 with the model ones, calculated at the best fit value of number density and UV field from Fig. A28.

species	$\log N$	
	observed	model
C I	$13.28^{+0.05}_{-0.04}$	13.28^a
C I*	$13.10^{+0.09}_{-0.10}$	13.22^a
C I**	$12.93^{+0.12}_{-0.18}$	12.64^a
H ₂ J0	$18.38^{+0.01}_{-0.01}$	18.38
H ₂ J1	$18.52^{+0.01}_{-0.01}$	18.47
H ₂ J2	$16.57^{+0.09}_{-0.17}$	16.47
H ₂ J3 ^b		15.53
H ₂ J4 ^b		14.04
H ₂ J5 ^b		13.62

(a) These values were obtained under the additional assumption that the total C I column density equates the observed one.

(b) We did not use these levels to compare with observed values, since the column densities measurements for these levels are subject to large systematic uncertainty (see text).

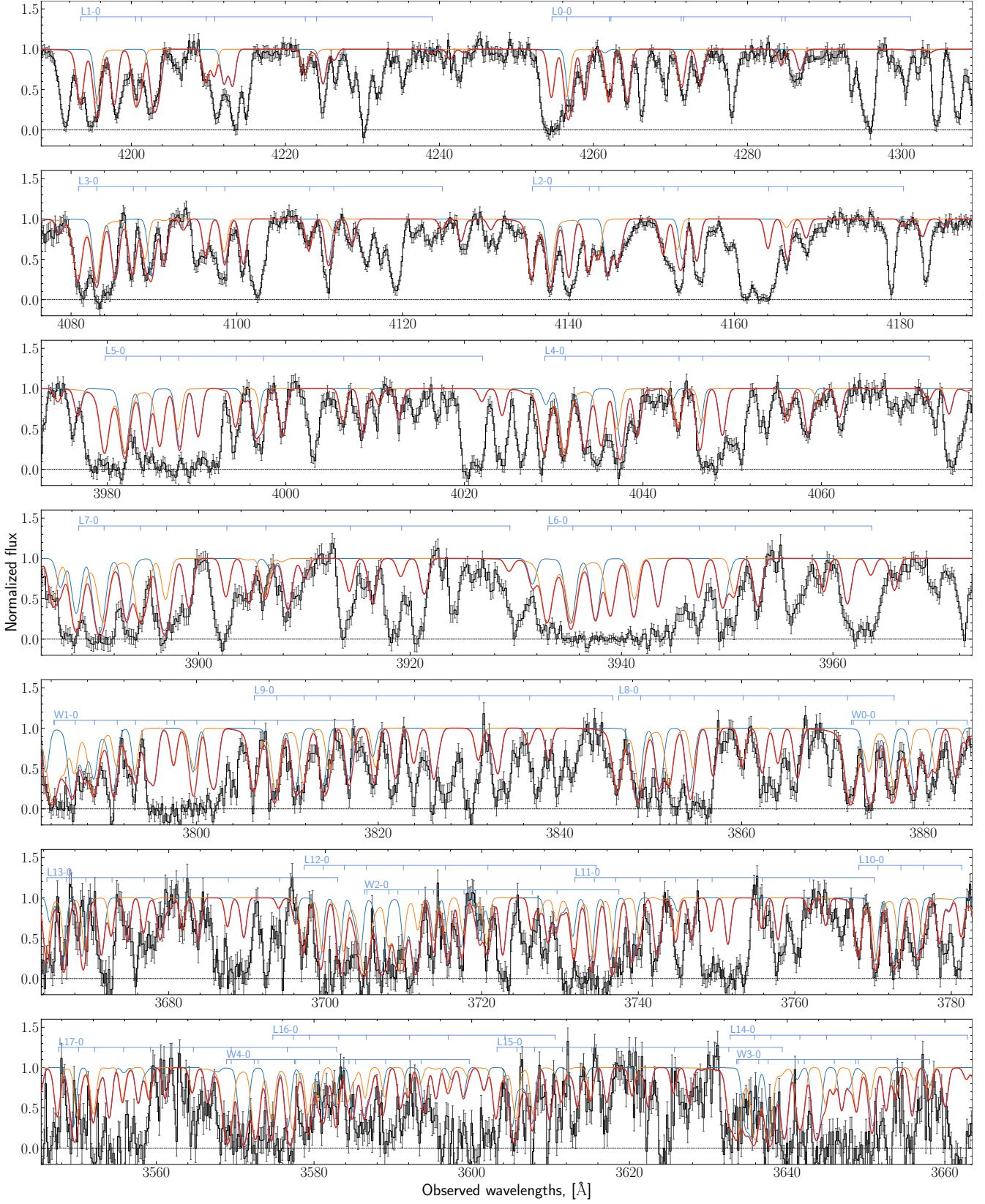


Figure A25. Fit to H₂ absorption lines at $z = 2.840$ towards J1146+0743.

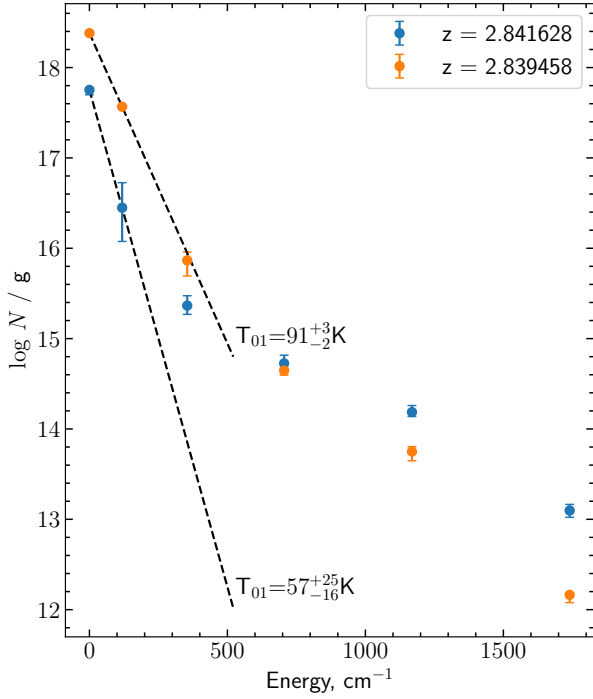


Figure A26. Excitation diagram for two H₂ components at $z = 2.840$ towards J1146+0743.

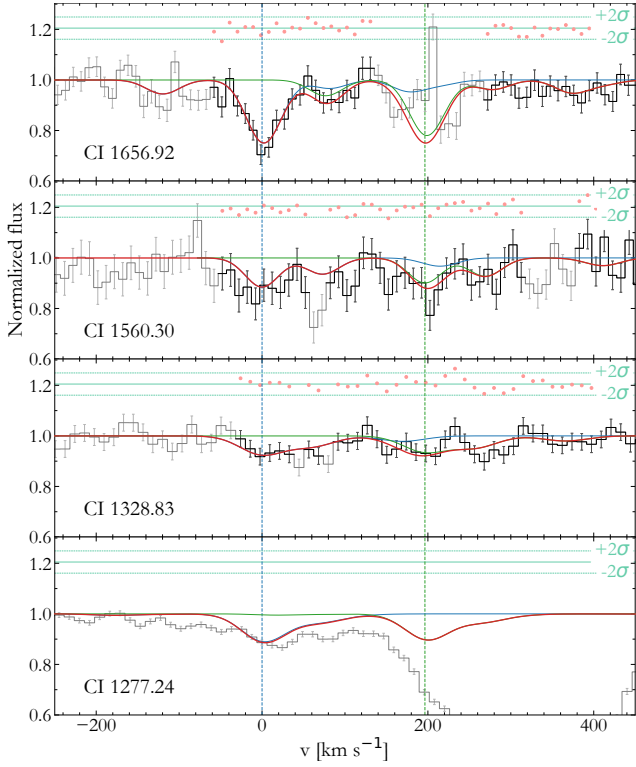


Figure A27. Fit to the C I absorption lines at $z = 2.840$ towards J1146+0743.

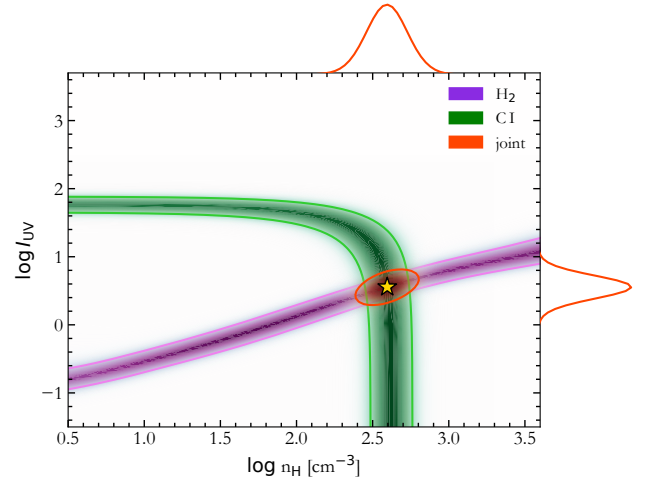


Figure A28. Constrains on the number density and UV field in H₂-bearing medium at $z = 2.83946$ towards J1146+0743 from the excitation of C I fine-structure and H₂ rotational levels. The colors and lines are the same as in Fig. 2.

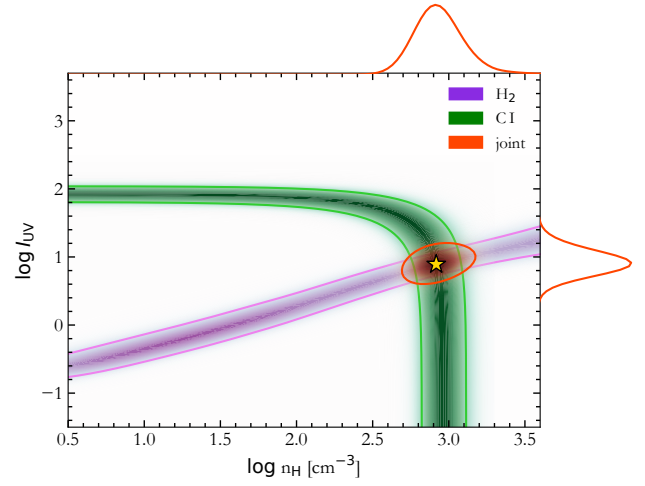


Figure A29. Constrains on the number density and UV field in H₂-bearing medium at $z = 2.84163$ towards J1146+0743 from the excitation of C I fine-structure and H₂ rotational levels. The colors and lines are the same as in Fig. 2.

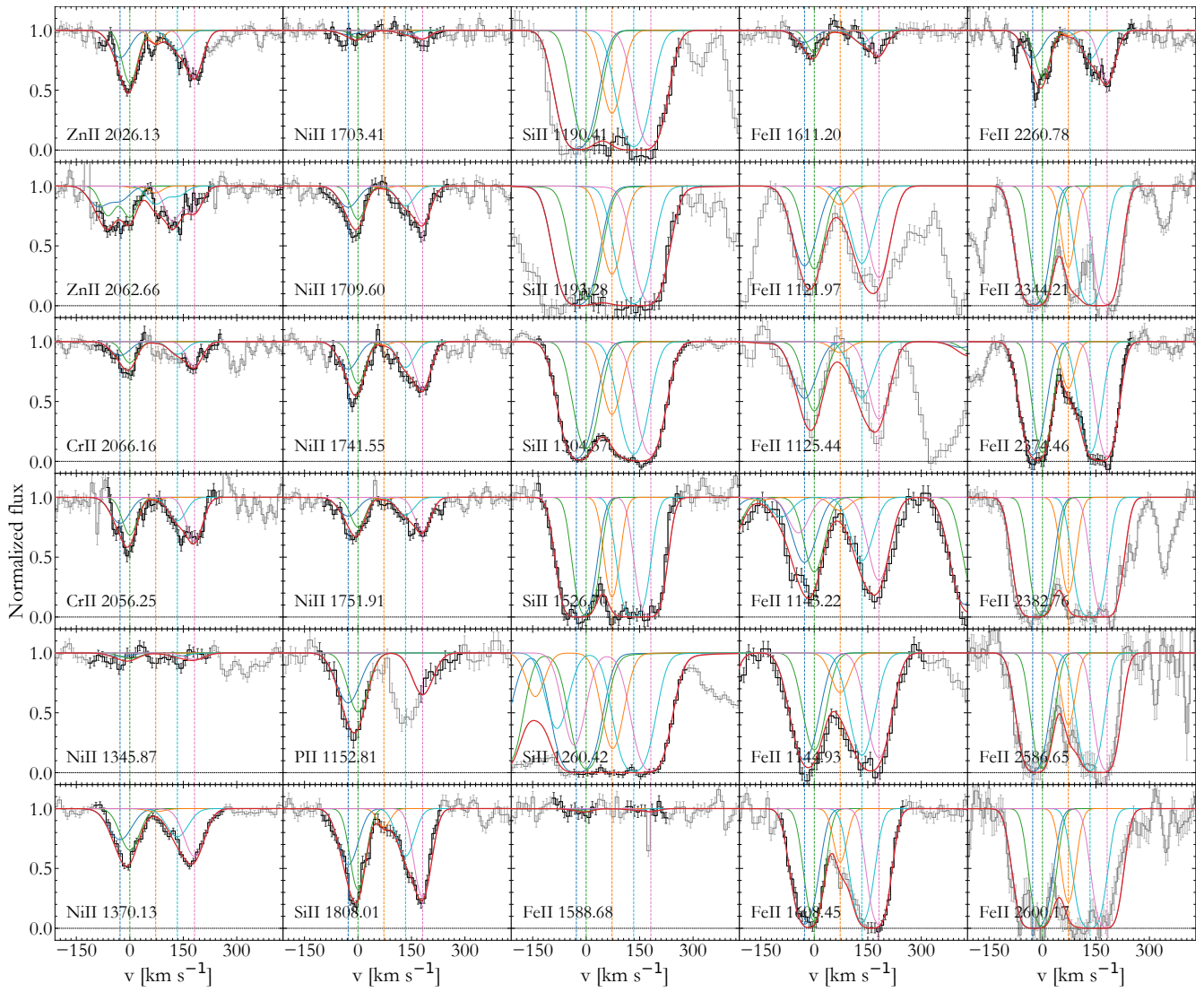


Figure A30. Fit to the metal absorption lines at $z = 2.840$ towards J1146+0743.

Table A20. Comparison of observed column densities in the component at $z=2.84163$ of DLA in J1146+0743 with the modelled ones, taken at the best fit values of number density and UV field from Fig. A29.

species	log N	
	observed	model
CI	$13.17^{+0.10}_{-0.11}$	13.15^a
CI*	$13.07^{+0.05}_{-0.08}$	13.18^a
CI**	$12.85^{+0.12}_{-0.11}$	12.67^a
H ₂ J0	$17.75^{+0.02}_{-0.05}$	17.28
H ₂ J1	$17.40^{+0.28}_{-0.37}$	17.51
H ₂ J2	$16.06^{+0.11}_{-0.10}$	15.84
H ₂ J3 ^b		14.86
H ₂ J4 ^b		13.68
H ₂ J5 ^b		13.23

(a) These values were obtained under the additional assumption that the total CI column density equates the observed one.

(b) We did not use these levels to compare with observed values, since the column densities measurements for these levels are subject to a large systematic uncertainty (see text).

Table A21. Fit results of metals towards J1146+0743.

comp	1	2	3	4	5	log N_{tot}	[X/H]	[X/ZnII]
z	2.838898($^{+38}_{-25}$)	2.839268($^{+16}_{-18}$)	2.840190($^{+24}_{-26}$)	2.84102($^{+4}_{-3}$)	2.841599($^{+16}_{-13}$)			
Δv , km s ⁻¹	-209.7	-182.2	-108.3	-45.8	0.0			
b , km s ⁻¹	29.0 $^{+1.0}_{-1.0}$	18.0 $^{+1.0}_{-1.0}$	11.8 $^{+1.7}_{-1.0}$	28.5 $^{+2.9}_{-4.4}$	21.0 $^{+0.6}_{-0.5}$			
log N (SiII)	15.65 $^{+0.04}_{-0.10}$	15.84 $^{+0.07}_{-0.06}$	14.91 $^{+0.08}_{-0.07}$	15.56 $^{+0.05}_{-0.07}$	15.89 $^{+0.04}_{-0.03}$	16.36 $^{+0.02}_{-0.01}$	-0.69 $^{+0.02}_{-0.02}$	-0.13 $^{+0.02}_{-0.01}$
log N (FeII)	15.06 $^{+0.06}_{-0.08}$	15.27 $^{+0.04}_{-0.05}$	14.14 $^{+0.07}_{-0.06}$	15.09 $^{+0.06}_{-0.05}$	15.31 $^{+0.04}_{-0.03}$	15.81 $^{+0.01}_{-0.01}$	-1.23 $^{+0.01}_{-0.01}$	-0.68 $^{+0.01}_{-0.02}$
log N (ZnII)	12.81 $^{+0.07}_{-0.09}$	13.07 $^{+0.05}_{-0.04}$	12.32 $^{+0.06}_{-0.07}$	12.63 $^{+0.05}_{-0.06}$	13.02 $^{+0.03}_{-0.03}$	13.54 $^{+0.01}_{-0.01}$	-0.56 $^{+0.01}_{-0.02}$	0.00 $^{+0.02}_{-0.02}$
log N (CrII)	13.49 $^{+0.06}_{-0.08}$	13.56 $^{+0.06}_{-0.06}$	12.33 $^{+0.24}_{-0.07}$	13.41 $^{+0.05}_{-0.07}$	13.64 $^{+0.04}_{-0.03}$	14.13 $^{+0.01}_{-0.01}$	-1.05 $^{+0.02}_{-0.01}$	-0.49 $^{+0.02}_{-0.02}$
log N (NiII)	13.94 $^{+0.07}_{-0.06}$	14.09 $^{+0.04}_{-0.05}$	12.87 $^{+0.16}_{-0.61}$	13.92 $^{+0.05}_{-0.06}$	14.12 $^{+0.03}_{-0.04}$	14.63 $^{+0.01}_{-0.01}$	-1.13 $^{+0.01}_{-0.01}$	-0.57 $^{+0.01}_{-0.01}$
log N (PII)	13.79 $^{+0.07}_{-0.12}$	13.93 $^{+0.10}_{-0.12}$			13.53 $^{+0.10}_{-0.08}$	14.24 $^{+0.04}_{-0.05}$	-0.71 $^{+0.04}_{-0.05}$	-0.15 $^{+0.04}_{-0.05}$

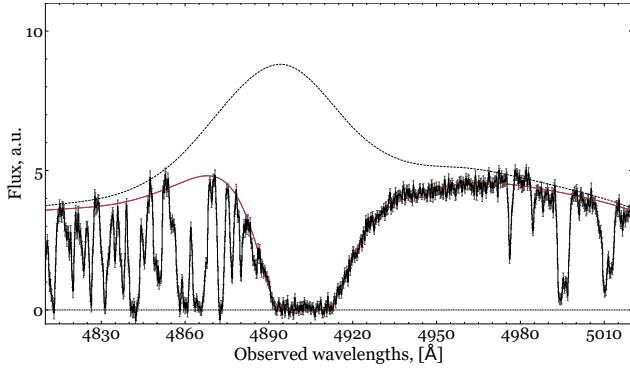


Figure A31. Fit to the damped H I Ly α absorption line at $z = 3.033$ towards J1236+0010.

Table A22. Fit results of H₂ towards J1236+0010.

z	$3.03292^{(+27)}_{(-18)}$
b , km s ⁻¹	$2.3^{+0.2}_{-0.2}$
$\log N(\text{H}_2 \text{ J0})$	$19.21^{+0.03}_{-0.02}$
$\log N(\text{H}_2 \text{ J1})$	$19.56^{+0.02}_{-0.00}$
$\log N(\text{H}_2 \text{ J2})$	$18.46^{+0.03}_{-0.04}$
$\log N(\text{H}_2 \text{ J3})$	$18.10^{+0.02}_{-0.02}$
$\log N(\text{H}_2 \text{ J4})$	$16.10^{+0.49}_{-0.16}$
$\log N(\text{H}_2 \text{ J5})$	$15.11^{+0.41}_{-0.28}$
$\log N_{\text{tot}}$	$19.76^{+0.01}_{-0.01}$

A6 SDSS J123602.11+001024.60

We measured the H I column density of the DLA at $z = 3.033$ towards J1236+0010 by fitting the Ly α absorption line with a single component together with the continuum modelled using a seventh order Chebyshev polynomial. We derived $\log N(\text{H I}) = 20.74 \pm 0.01$ at the best fit value of $z = 3.03284$. The Ly α profile, together with the reconstructed quasar continuum are shown in Fig. A31. Interestingly, that reconstructed continuum indicates that DLA is redshifted regarding Ly α emission line of quasar by ~ 500 km s⁻¹ (see Fig. A31).

We fitted the H₂ absorption lines towards J1236+0010 using a one component model. The result of the fit is given in Table A22 and H₂ line profiles are shown in Fig. A32. The excitation diagram of H₂ rotation levels is shown in Fig. A33 and we derived $T_{01} = 122^{+9}_{-7}$ K.

We detected C I absorption lines in three fine structure levels in a single component corresponding to H₂. The result from fitting these lines is given in Table A23 and the corresponding profiles are shown in Fig. A34.

The constrained values of the hydrogen number density and UV field in the H₂/C I-bearing medium are shown in Fig. A35 and the comparison between observed and model column densities at the best fit value (yellow star in Fig. A35) is provided in Table A24.

Metal lines are fitted using a nine components model. The second component of metals from the red side coincides with position of H₂/C I-bearing component of the DLA. The results of the fit are given in Table A25 and the fit profiles are shown in Fig. A36.

Table A23. Fit results of C I towards J1236+0010.

z	$3.032969^{(+17)}_{(-8)}$
b , km s ⁻¹	$2.0^{+0.4}_{-0.2}$
$\log N(\text{C I})$	$14.28^{+0.36}_{-0.37}$
$\log N(\text{C I}^*)$	$13.70^{+0.11}_{-0.08}$
$\log N(\text{C I}^{**})$	$13.18^{+0.11}_{-0.16}$
$\log N_{\text{tot}}$	$14.35^{+0.33}_{-0.25}$

Table A24. Comparison of the observed column densities in the DLA towards J1236+0010 with the model ones, calculated at the best fit value of the number density and UV field from Fig. A35.

species	log N	
	observed	model
C I	$14.28^{+0.36}_{-0.37}$	14.24^a
C I*	$13.70^{+0.11}_{-0.08}$	13.88^a
C I**	$13.18^{+0.11}_{-0.16}$	12.89^a
H ₂ J0	$19.21^{+0.03}_{-0.02}$	19.14
H ₂ J1	$19.56^{+0.02}_{-0.01}$	19.61
H ₂ J2	$18.46^{+0.03}_{-0.02}$	18.26
H ₂ J3 ^b		17.42
H ₂ J4 ^b		15.29
H ₂ J5 ^b		14.59

(a) These values were obtained under the additional assumption that the total C I column density equates the observed one.

(b) We did not use these levels to compare with observed values, since the column densities measurements for these levels are subject to a large systematic uncertainty (see text).

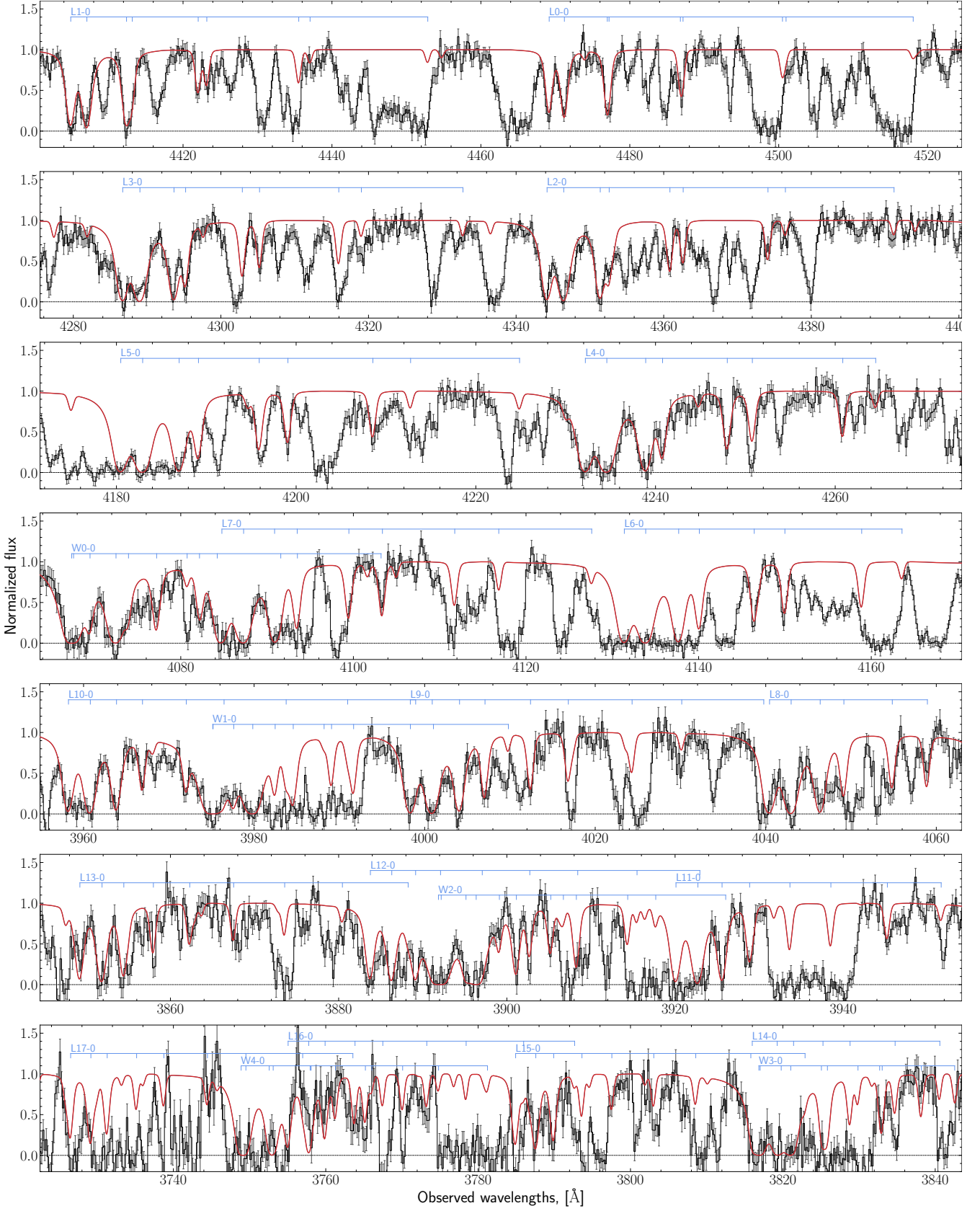
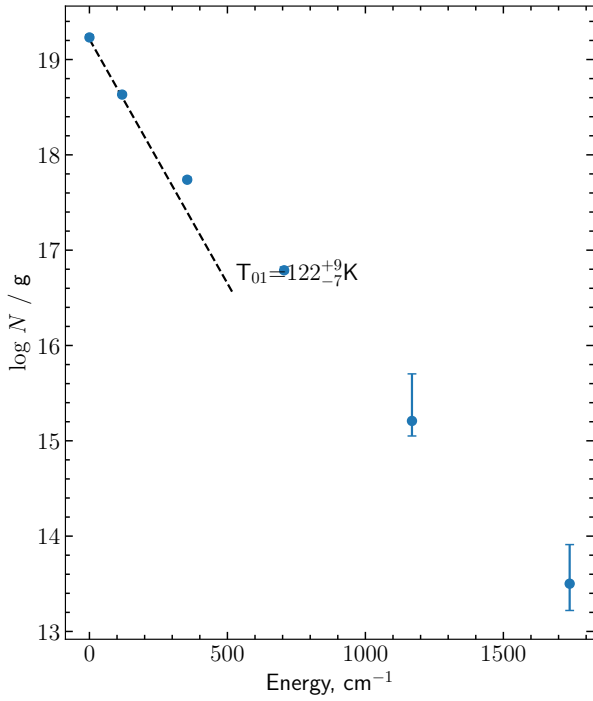
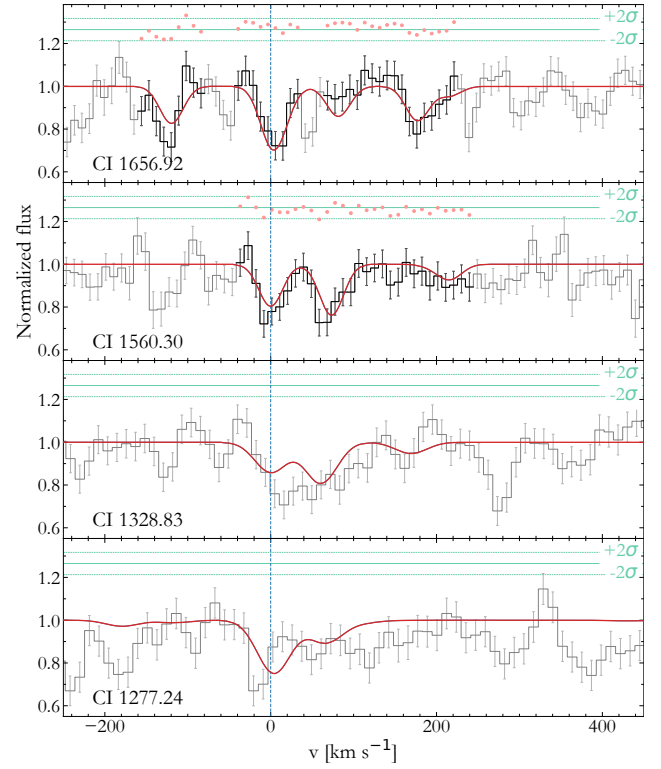


Figure A32. Fit to the H₂ absorption lines at $z = 3.033$ towards J1236+0010.

Table A25. Fit results of metals towards J1236+0010.

comp	z	Δv , km s ⁻¹	b, km s ⁻¹	$\log N(\text{SiII})$	$\log N(\text{OI})$	$\log N(\text{SII})$	$\log N(\text{FeII})$
1	3.026187 ⁽⁺²⁹⁾ ₍₋₃₄₎	-512.9	14.7 ^{+2.0} _(-2.2)	13.80 ^{+0.07} _(-0.04)	14.18 ^{+0.05} _(-0.09)		
2	3.02696 ⁽⁺⁴⁾ ₍₋₃₎	-457.0	13.0 ^{+2.0} _(-1.7)	13.71 ^{+0.07} _(-0.06)	14.11 ^{+0.10} _(-0.08)		
3	3.02797 ⁽⁺³⁾ ₍₋₆₎	-380.4	16.7 ^{+3.0} _(-3.3)	14.43 ^{+0.12} _(-0.11)	15.47 ^{+0.30} _(-0.23)	14.65 ^{+0.07} _(-0.07)	13.63 ^{+0.10} _(-0.13)
4	3.028675 ⁽⁺²⁸⁾ ₍₋₅₂₎	-334.7	31.6 ^{+1.4} _(-2.9)	14.58 ^{+0.05} _(-0.07)	15.17 ^{+0.05} _(-0.10)	14.52 ^{+0.12} _(-0.14)	13.94 ^{+0.07} _(-0.06)
5	3.030418 ⁽⁺¹³⁾ ₍₋₁₄₎	-202.7	8.4 ^{+2.9} _(-0.9)	13.80 ^{+0.12} _(-0.04)	16.21 ^{+0.15} _(-1.48)		13.09 ^{+0.10} _(-0.08)
6	3.03142 ⁽⁺¹²⁾ ₍₋₈₎	-123.5	49.1 ^{+0.9} _(-16.1)	13.30 ^{+0.07} _(-0.10)			12.50 ^{+0.22} _(-0.32)
7	3.03234 ⁽⁺⁴⁾ ₍₋₃₎	-60.7	24.4 ^{+2.5} _(-2.5)	13.66 ^{+0.08} _(-0.06)	15.28 ^{+0.07} _(-0.08)		13.42 ^{+0.04} _(-0.05)
8	3.033152 ⁽⁺¹³⁾ ₍₋₇₎	0.0	13.7 ^{+0.8} _(-0.7)	15.58 ^{+0.08} _(-0.04)	16.65 ^{+0.52} _(-0.33)	15.21 ^{+0.06} _(-0.03)	14.46 ^{+0.04} _(-0.04)
9	3.033699 ⁽⁺³³⁾ ₍₋₂₈₎	39.5	21.1 ^{+1.6} _(-2.3)	13.74 ^{+0.08} _(-0.06)	14.97 ^{+0.12} _(-0.08)		
$\log N_{\text{tot}}$				15.69 ^{+0.06} _(-0.05)	16.77 ^{+0.44} _(-0.23)	15.39 ^{+0.03} _(-0.04)	14.66 ^{+0.03} _(-0.03)
[X/H]				-0.60 ^{+0.06} _(-0.05)	-0.70 ^{+0.44} _(-0.23)	-0.51 ^{+0.03} _(-0.04)	-1.62 ^{+0.04} _(-0.03)
[X/SII]				-0.09 ^{+0.07} _(-0.06)	-0.19 ^{+0.44} _(-0.23)	0.00 ^{+0.05} _(-0.05)	-1.11 ^{+0.05} _(-0.04)

**Figure A33.** Excitation diagram of H₂ at $z = 3.033$ towards J1236+0010.**Figure A34.** Fit to the CI absorption lines at $z = 3.033$ towards J1236+0010.

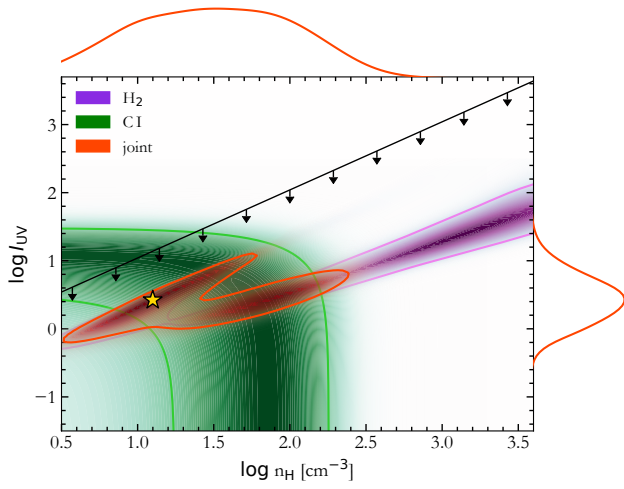


Figure A35. Constraints on the number density and UV field in H₂-bearing medium at $z = 3.033$ towards J1236+0010 from the excitation of CI fine-structure and H₂ rotational levels. The colors and lines are the same as in Fig. 2.

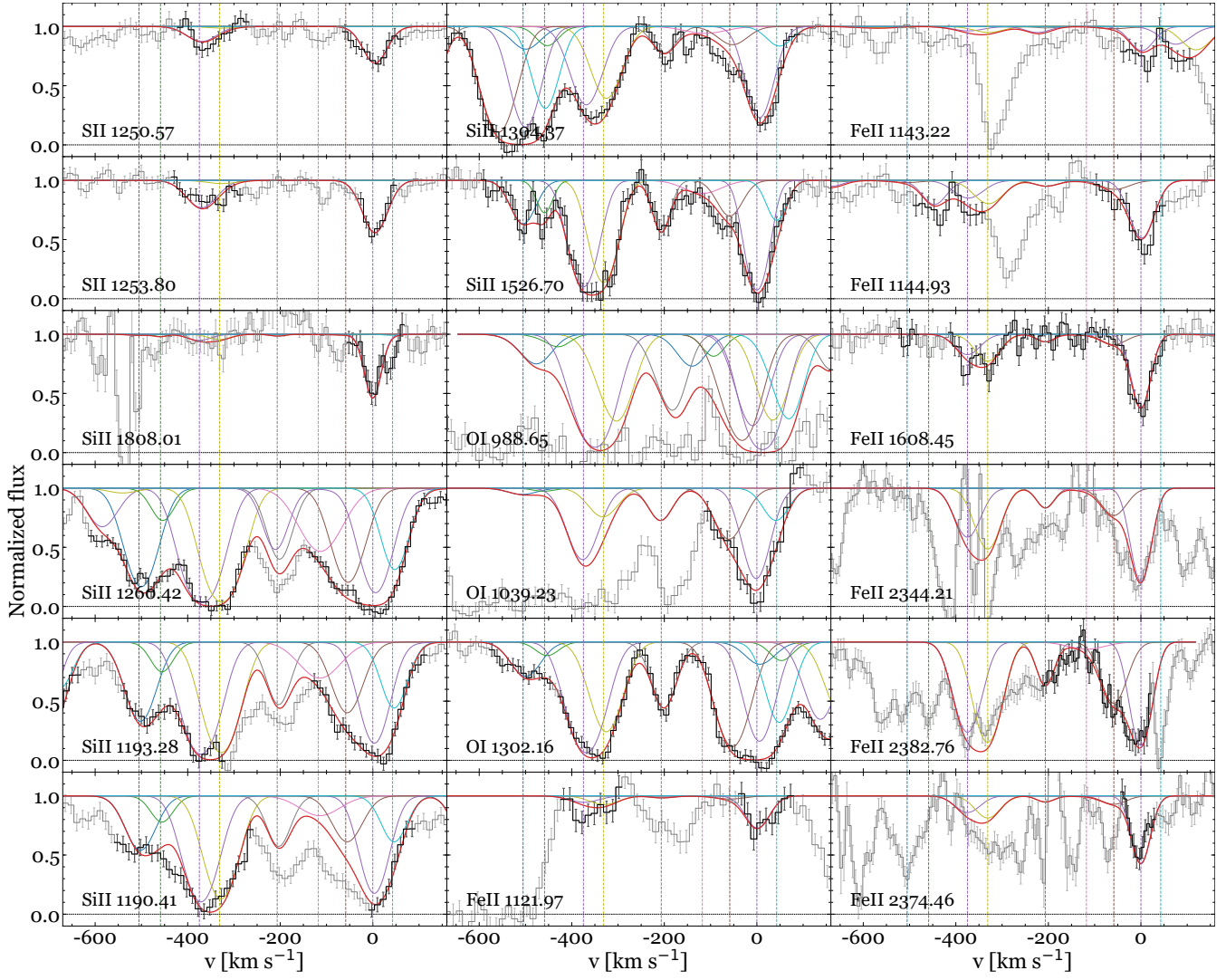


Figure A36. Fit to the metal absorption lines at $z = 3.033$ towards J1236+0010.

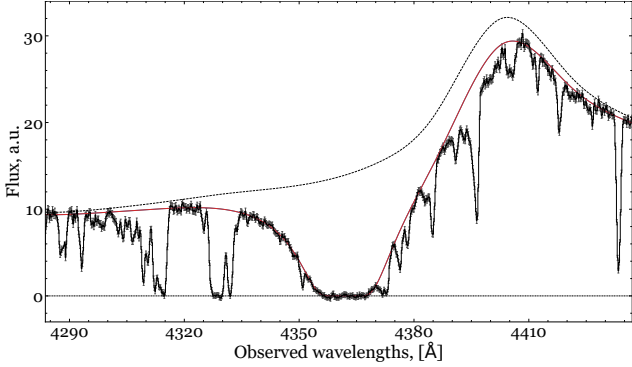


Figure A37. Fit to the damped H I Ly α absorption line at $z = 2.588$ towards J2347–0051.

A7 SDSS J234730.76–005131.68

We measured the H I column density of the DLA at $z = 2.588$ towards J2347–0051 by fitting the Ly α absorption line with a single component together with the continuum modelled using a seventh order Chebyshev polynomial. We derived $\log N(\text{H I}) = 20.47 \pm 0.01$ at the best fit value of $z = 2.58813$. The Ly α profile, together with the reconstructed quasar continuum are shown in Fig. A37. There is additional DLA at $z = 1.9742$ in this spectrum with strong metal absorption lines.

We fitted the H₂ absorption lines towards J2347–0051 using a one component model. The result of the fit is given in Table A26 and H₂ line profiles are shown in Fig. A38. The excitation diagram of H₂ rotation levels is shown in Fig. A39 and we derived $T_{01} = 76^{+2}_{-1}$ K.

We detected C I absorption lines in three fine structure levels in a single component corresponding to H₂. The result from fitting these lines is given in Table A27 and the corresponding profiles are shown in Fig. A40. C I $\lambda 1565\text{\AA}$ line is located at the wing of C IV emission line of quasar. Therefore we included partial coverage of at this line into consideration. We estimated the the covering factor at this line to be $0.93^{+0.07}_{-0.11}$ which is consistent with the total coverage of emission region of quasar by C I-bearing absorption system. However X-shooter resolution do not allow us to resolve the velocity components of the system and therefore this case should be studied using high resolution spectrum.

The constrained values of the hydrogen number density and UV field in the H₂/C I-bearing medium are shown in Fig. A41 and the comparison between observed and model column densities at the best fit value (yellow star in Fig. A41) is provided in Table A28.

Metal lines are fitted using a four components model. The third component of metals corresponds to H₂/C I-bearing component of the DLA. The results of the fit are given in Table A29 and the fit profiles are shown in Fig. A42.

This paper has been typeset from a T_EX/L^AT_EX file prepared by the author.

Table A26. Fit results of H₂ towards J2347–0051.

z	$2.587969^{(+10)}_{(-9)}$
b , km s ⁻¹	$6.1^{+0.2}_{-0.1}$
$\log N(\text{H}_2 \text{ J0})$	$19.14^{+0.01}_{-0.01}$
$\log N(\text{H}_2 \text{ J1})$	$19.12^{+0.01}_{-0.01}$
$\log N(\text{H}_2 \text{ J2})$	$16.23^{+0.07}_{-0.10}$
$\log N(\text{H}_2 \text{ J3})$	$15.92^{+0.07}_{-0.06}$
$\log N(\text{H}_2 \text{ J4})$	$14.77^{+0.04}_{-0.05}$
$\log N(\text{H}_2 \text{ J5})$	$14.10^{+0.09}_{-0.11}$
$\log N_{\text{tot}}$	$19.44^{+0.01}_{-0.01}$

Table A27. Fit results of C I towards J2347–0051.

z	$2.587986^{(+11)}_{(-13)}$
b , km s ⁻¹	$1.1^{+0.3}_{-0.2}$
$\log N(\text{C I})$	$14.04^{+0.40}_{-0.54}$
$\log N(\text{C I}^*)$	$13.31^{+0.12}_{-0.10}$
$\log N(\text{C I}^{**})$	$12.99^{+0.12}_{-0.14}$
$\log N_{\text{tot}}$	$14.16^{+0.23}_{-0.44}$

Table A28. Comparison of the observed column densities in the DLA towards J2347–0051 with the model ones, calculated at the best fit value of number density and UV field from Fig. A41.

species	log N	
	observed	model
C I	$14.28^{+0.36}_{-0.37}$	14.24 ^a
C I*	$13.70^{+0.11}_{-0.08}$	13.87 ^a
C I**	$13.18^{+0.11}_{-0.10}$	12.96 ^a
H ₂ J0	$19.14^{+0.10}_{-0.01}$	19.24
H ₂ J1	$19.12^{+0.01}_{-0.01}$	18.97
H ₂ J2	$16.23^{+0.07}_{-0.10}$	16.09
H ₂ J3 ^b		14.93
H ₂ J4 ^b		13.59
H ₂ J5 ^b		13.14

(a) These values were obtained under the additional assumption that the total C I column density equates the observed one.

(b) We did not use these levels to compare with observed values, since the column densities measurements for these levels are subject to a large systematic uncertainty (see text).

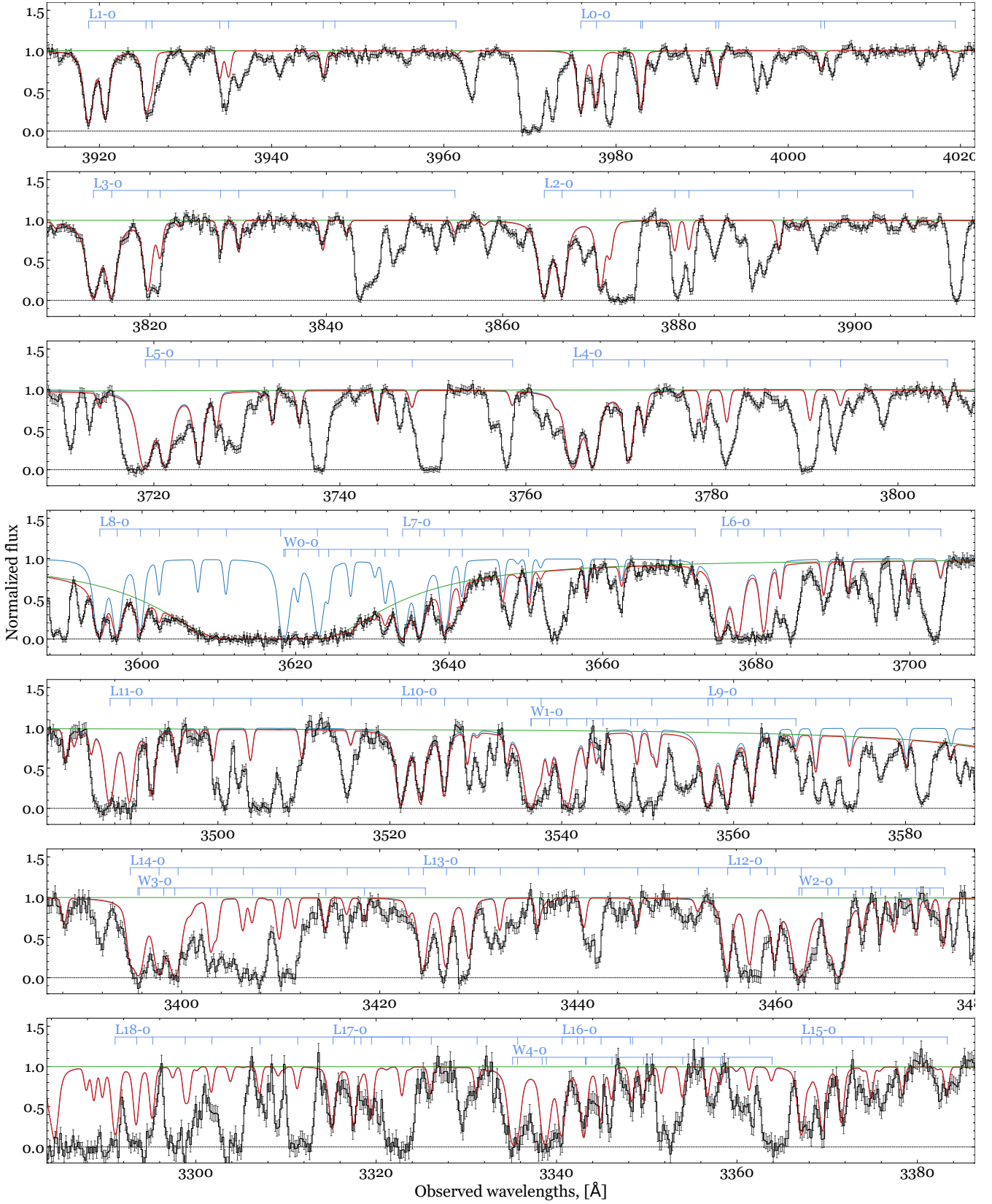


Figure A38. Fit to the H_2 absorption lines at $z = 2.588$ towards J2347–0051.

Table A29. Fit results of metals towards J2347–0051.

comp	1	2	3	4	log <i>N</i> _{tot}	[X/H]	[X/SII]
<i>z</i>	2.587008 ⁽⁺⁹⁾ ₍₋₅₎	2.587633 ⁽⁺¹²⁾ ₍₋₁₁₎	2.5879841 ⁽⁺²⁶⁾ ₍₋₄₎	2.5883292 ⁽⁺⁴⁾ ₍₋₇₀₎			
Δ <i>v</i> , km s ⁻¹	-81.2	-29.3	0.0	28.4			
<i>b</i> , km s ⁻¹	24.98 ^{+0.88} _{-0.47}	6.17 ^{+0.52} _{-0.83}	8.00 ^{+0.75} _{-0.65}	19.38 ^{+0.74} _{-1.04}			
log <i>N</i> (SiII)	14.64 ^{+0.03} _{-0.01}	13.96 ^{+0.11} _{-0.04}	14.89 ^{+0.07} _{-0.07}	14.05 ^{+0.03} _{-0.04}	15.14 ^{+0.05}	-0.91 ^{+0.05}	-0.09 ^{+0.06}
log <i>N</i> (FeII)	14.15 ^{+0.01} _{-0.01}	13.59 ^{+0.04} _{-0.04}	14.06 ^{+0.07} _{-0.05}	13.50 ^{+0.02} _{-0.02}	14.51 ^{+0.03}	-1.53 ^{+0.02}	-0.71 ^{+0.05}
log <i>N</i> (NiII)	13.05 ^{+0.13} _{-0.26}	12.67 ^{+0.28} _{-0.84}	13.38 ^{+0.06} _{-0.09}	< 12.8	13.55 ^{+0.07}	-1.21 ^{+0.07}	-0.40 ^{+0.08}
log <i>N</i> (SII)	14.41 ^{+0.05} _{-0.03}	13.85 ^{+0.25} _{-0.39}	14.63 ^{+0.07} _{-0.11}	< 14.2	14.84 ^{+0.05}	-0.82 ^{+0.05}	0.0
log <i>N</i> (CrII)	12.63 ^{+0.23} _{-0.48}	12.49 ^{+0.16} _{-0.99}	12.57 ^{+0.14} _{-0.18}	< 12.4	12.94 ^{+0.16}	-1.24 ^{+0.16}	-0.42 ^{+0.16}
log <i>N</i> (ZnII)	< 11.4	11.97 ^{+0.16} _{-0.27}	12.31 ^{+0.08} _{-0.11}	< 11.4	12.50 ^{+0.08}	-0.60 ^{+0.08}	0.22 ^{+0.06}
log <i>N</i> (NI)	13.43 ^{+0.13} _{-0.21}	< 12.3	13.91 ^{+0.11} _{-0.07}	< 13	14.05 ^{+0.07}	-2.32 ^{+0.07}	-1.50 ^{+0.08}

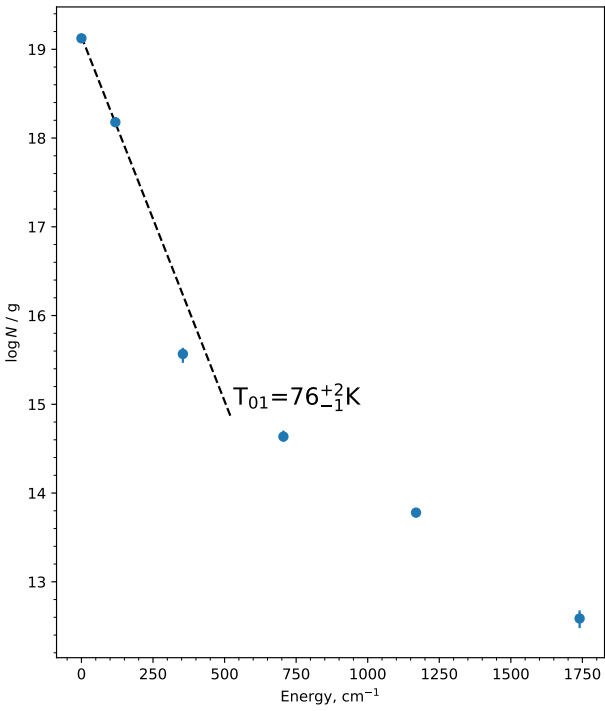


Figure A39. Excitation diagram of H₂ at *z* = 2.588 towards J2347–0051.

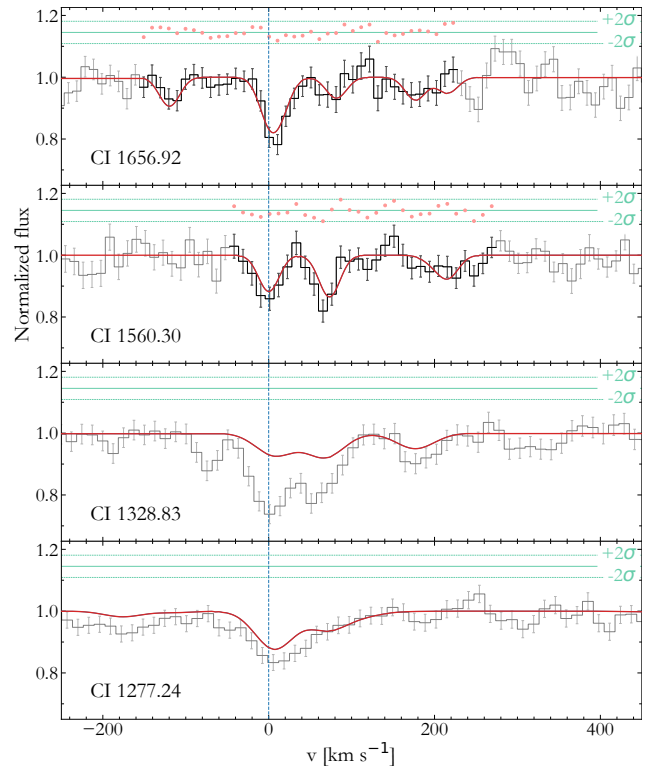


Figure A40. Fit to the C I absorption lines at *z* = 2.588 in J2347–0051. C I lines near C I λ1328 transition are blended with C IV doublet at *z* ≈ 2.0744.

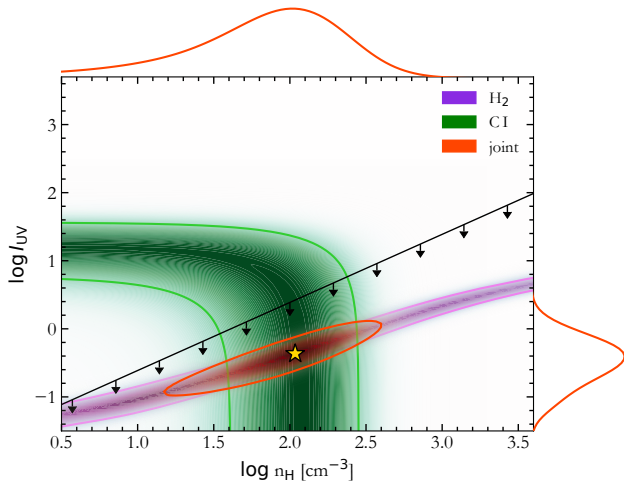


Figure A41. Constraints on the number density and UV field in H₂-bearing medium at $z = 2.588$ towards J2347–0051 from the excitation of CI fine-structure and H₂ rotational levels. The colors and lines are the same as in Fig. 2.

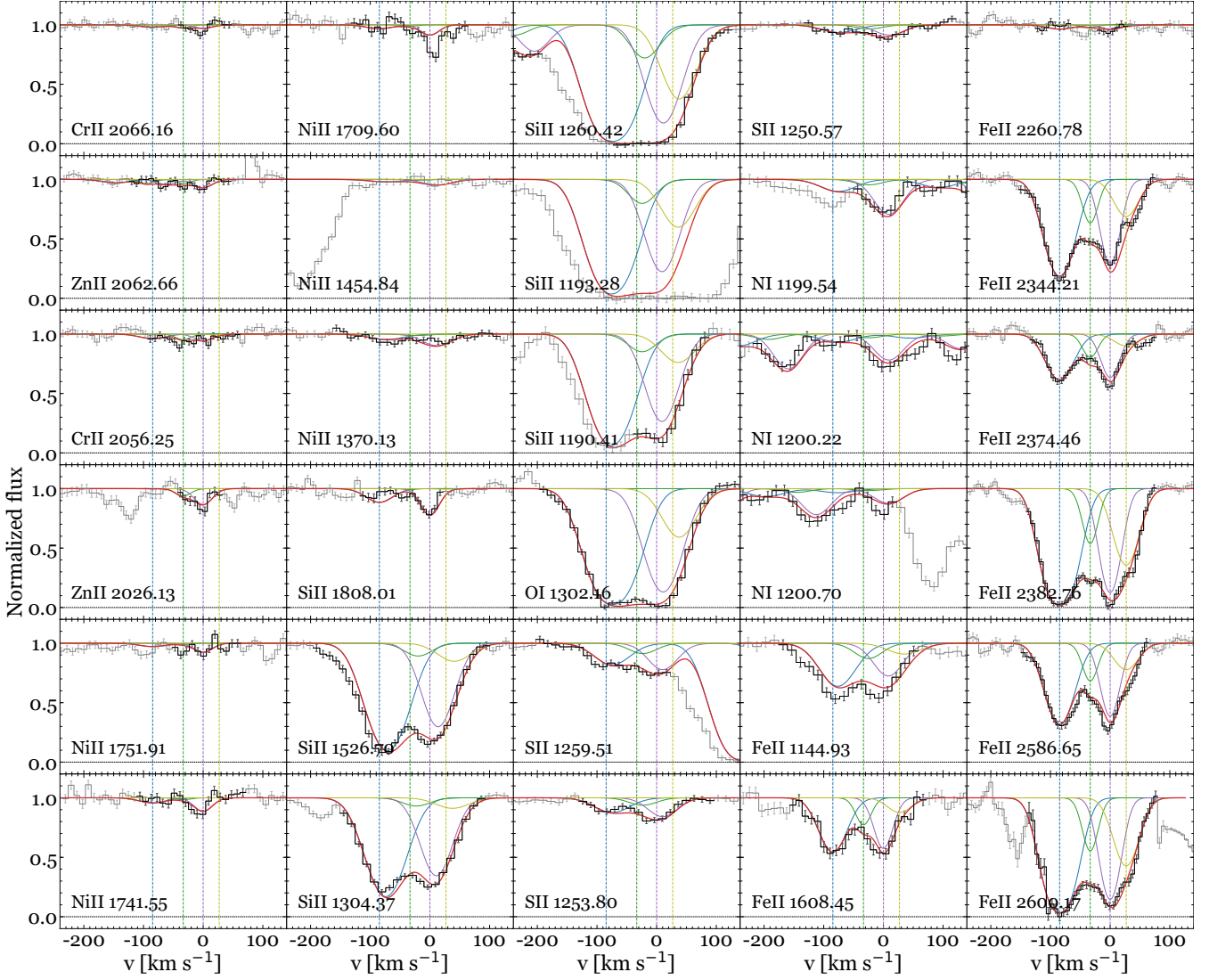


Figure A42. Fit to the metal absorption lines at $z = 2.588$ towards J2347-0051.